Morphological and Chemical Changes in *in vitro* Bone Mineral and the Effect of Strontium on *in vitro* Mineralisation

Kharissa Ayu Perdana Nitiputri

Department of Materials

Imperial College London

This thesis is submitted in fulfilment of the requirements Doctor of Philosophy (PhD) degree of Imperial College London

Author's Declaration

I, Kharissa Nitiputri, performed the work done in this thesis in the Materials Department of Imperial collagen London, unless otherwise stated. I wrote this thesis, and the results obtained by others are appropriately referenced. Some of results present in this thesis have been published and presented in:

1. Nitiputri K, Boonrungsiman S, Porter A, Stevens M.M. An *In Vitro* Study into Early Collagen Mineralization on the Potential Role of Intracellular Calcified Vesicles in Mineralization. Poster Presentation in the Gordon Research Seminar and Conference in Biomineralization. 2012.

2. Nitiputri K, Kalepitis C, Hedegaard M, Hadjilucas L, Bharath A, Porter A, Stevens M.M. Strontium Concentration Affects Long-term *In Vitro* Optimum Collagen Arrangement & Mineralization. Oral Presentation in the 12th International Symposium on Biomineralization. 2013.

3. Nitiputri K, Kalepitis C, Hedegaard M, Hadjilucas L, Bharath A, Porter A, Stevens M.M. Strontium Concentration Affects Long-term *In Vitro* Optimum Collagen Arrangement & Mineralization. Poster Presentation in the Materials Department Postgraduate Research Day at Imperial College London. 2013

Copyright Declaration

Table of Contents

Abstract

The steps involved in early bone mineralisation have been extensively studied. Studies have suggested various means by which bone mineralisation occurs: (1) a cell-independent (protein-assisted) process where non-collagenous proteins mediate soluble ions to form mineral on the collagen fibril; (2) a cell-controlled mechanism where mineral seeds formed within intracellular vesicles released from the plasma membrane would subsequently rupture and disperse their contents on the extracellular matrix; and (3) an acellular route in which amorphous calcium phosphate mineral precursors are produced and deposited in collagen fibrils where they transform into more crystalline apatite platelets.

Despite extensive studies, there are still unanswered questions about how bone becomes bone. The first series of experiments in this thesis are aimed at studying the mineral characteristics of early *in vitro* osteoblast mineralisation at the extracellular matrix. These experiments seek to determine the sequence of possible mineralisation events that take place during mineral nucleation and growth on collagen. Transmission electron microscopy was used to provide high spatial resolution, which was compounded with chemical analysis of energy dispersive x-ray and electron energy-loss spectroscopies. We identified carbonate-rich calcium phosphate dense granules in the extracellular matrix that may act as seeds for growth into larger, submicron-sized, globular aggregates of apatite mineral with a different stoichiometry. These globules appear to mineralise the collagen fibrils forming crystalline textured crystals with higher calcium-to-phosphate ratio and lower carbonate content as the mineral phase of bone. We provide new evidence that the use of a carbonate rich, amorphous calcium phosphate spherical bioseed could be a process by which a soluble calcium phosphate phase is stabilised and delivered to the collagen for subsequent maturation and collagen mineralisation.

We also examined the effect of strontium ion supplementation to bone mineralisation as a translational study. Previous studies showed the positive effects of *in vivo* strontium supplementation as an anti-osteoporotic drug. Strontium is able to: (1) stimulate bone formation; (2) increase osteoid surface, osteoblast surface, and

bone forming surfaces; (3) decrease bone resorbing cells; (4) increase bone strength and mass; and (5) reduce the risk of fractures. In the *in vitro* system, studies have focused on how strontium ions increase bone mineral's *a*- and *c*-axis lattice parameters. The effect of strontium ions on the matrix component of bone is the aim for the second part of this thesis.

Using Raman spectroscopy, TEM imaging, and biochemical quantification, we studied the effect of strontium ion supplementation on *in vitro* MC3T3 osteoblasts, with close focus on the osteoblast matrix. We observed that cultures treated with high strontium supplementation had impaired mineralisation, where nodules were formed but failed to mineralise. Periodic collagen banding was seen on TEM micrograph from all treatments. Collagen organisation was quantified using image analysis of TEM micrograph, and strontium supplementation seemed to affect fibril organisation. A slight addition of 0.1 mM strontium seemed to result in the less random organisation of collagen fibril, while 3 mM supplementation seemed to increase the random organisation. Only cultures treated with the highest amount of strontium supplementation showed an abundance of matrix vesicles around the collagen fibrils. Raman spectroscopy showed an increase in lipid detection on strontium supplemented groups, which may be due to the increased presence of matrix vesicles. Taken together, high strontium supplementation may decrease the rate of degradation of matrix vesicles and lead to altered mineralisation whereby nodules form but fail to mineralise. The relative amounts of collagen were also explored by Raman spectroscopy and hydroxyproline analysis; however, our findings were not statistically significant. Further experiments are needed to more completely elucidate the molecular mechanisms at play in strontium's effect on bone mineralisation.

Acknowledgement

To the Giants, whose shoulders I have been standing firmly on,
To the Mentors, who have walked alongside the ups and downs,
To the Parents, who have sacrificed immeasurably,
To the Peers, who shares the sorrows and triumphs,
To the Husband, who has made my days complete,
Thank you.

To the Triune God, who has given me unmerited favour and does not give me what I deserve,
I am grateful.

'The fear of the LORD is the beginning of wisdom, and knowledge of the Holy One is understanding.''

Proverbs 9 : 10 New International Version 1984

This PhD thesis was supervised by Professor Molly M. Stevens and Dr. Alexandra Porter.

During the course of the experiments, Dr. Hélène Autefage mentored cell culture experiments. Electron microscopy work was helped by Dr. Quentin Ramasse (SuperSTEM, Daresbury, UK) and Dr. Catriona McGilvery.

List of Figures

List of Abbreviations

ACP	Amorphous Calcium Phosphate
ADF	Annular Dark Field
ALP	Alkaline Phosphatase
BF	Bright Field
BGP	β-Glycerophosphate
BSP	Bone Sialoprotein
Ca/P	Calcium to Phosphate Ratio
CaSR	Calcium Sensing Receptor
CCD	Charge-Coupled Device
CFE	Cold Field Emission
CHA	Carbonated Hydroxyapatite
DF	Dark Field
DNA	Deoxyribonucleic Acid
DOS	Density of Unfilled States
ECM	Extracellular Matrix
EDTA	Ethylenediaminetetraacetic Acid
EDX	Electron Dispersive X-ray Spectroscopy
EEL	Electron Energy-Loss
EELS	Electron Energy-Loss Spectroscopy
ELNES	Energy-Loss Near-Edge Structure
eV	electron Volt
FBS	Foetal Bovine Serum
FEG	Field Emission Gun
FIB	Focused Ion Beam
FTIR	Fourier Transform Infrarred Spectroscopy
HAADF	High Angular Annular Dark Field
HRTEM	High Resolution Transmission Electron Microscopy
ICP-OES	Inductively Coupled Plasma Optical Emission Spectroscopy
MLLS	Multiple Linear Least Squares
mM	milli Molar
mrad	milli Radian
MSC	Mesenchymal Stem Cells
MV	Matrix Vesicle
NA	Numerical Aperture
NCP	Non-Collagenous Proteins
NF-κB	Nuclear Factor-κB
OCP	Octacalcium Phosphate
OPG	Osteoprotegerin
PBS	Phosphate-Buffered Solution
PC	Principal Component
PCA	Principal Component Analysis
PCR	Polymerase Chain Reaction
PIPES	piperazine-N,N’-bis(2-ethanesulfonic acid)

PPAR-γ	Peroxisome proliferator-activated receptor gamma
RANK	Receptor Activator of Nuclear Factor-κB
RANKL	Receptor Activator of Nuclear Factor-κB Ligand
SAED	Selected Area Electron Diffraction
SEM	Scanning Electron Microscope
STEM	Scanning Transmission Electron Microscope
TEG	Thermionic Emission Gun
TEM	Transmission Electron Microscope
TRAP	Tartrate-Resistant Acid Phosphatase
UK	United Kingdom
USA	United States of America
UV	Ultraviolet
XRD	X-Ray Diffraction
YAG	Yttrium Aluminum Garnet

List of Tables

1. Introduction

In today's ageing society, the global proportion of individuals aged 60 years and over has increased from around 9% in 1990 to 12% (841 million people) in 2013, and is predicted to reach 21% (2 billion people) by 2050. With increased life expectancy, health risks associated with old age will become increasingly costly to the government and individuals. Osteoporosis is a major bone metabolic disease associated with old age and has become a global public health problem that affects 200 million people worldwide in 2009 [1]. In the USA alone, 1.5 billion dollars was spent on treating osteoporosis-related fractures in 2005, and is estimated to accumulate to $474 billion over the next two decades [2]. Osteoporosis is not only a financial burden, but also lowers the quality of life through pain and disability.

With this increasing financial cost caused by bone diseases, the demand to understand the fundamentals of the bone maturation process, along with the effectiveness of certain treatments for bone diseases, has intensified. The two studies conducted in this thesis seek to understand: (1) the stages of *in vitro* bone mineral maturation, which may enable the engineering of more appropriate bone substitutes in the future; and (2) the effect of strontium ion supplementation on bone mineralisation *in vitro*, especially on the matrix component. Understanding how strontium affects bone mineralisation could lead to the development of better bone substitutes with increased biological activities.

1.1. Fundamental Understanding of Stages of Bone Mineralisation

The discovery of X-rays in the late 1800s opened up the field of bone research. X-ray technology made it possible to detect the nanoscale building blocks of bone *in situ*. In the 1930s, electron microscopes contributed to this field of research in various ways. Electron microscopy enabled characterisation of the hierarchical nature of bone, especially of long bones and also helped determine bone mineral crystallinity (through electron diffraction) and elemental analysis (through energy dispersive spectroscopy [EDX] and electron energy loss spectroscopy [EELS]). Despite decades of research on bone, many questions still remain, including: what are the maturation steps of early bone matrix mineralisation; where does the calcium come from; how the calcium is transported; how are the cells are involved in matrix mineralisation; and how, and in which format, is the mineral first deposited to the matrix?

The ideal approach to studying early bone mineralisation would be to conduct simultaneous high-resolution imaging and elemental analysis and diffraction studies *in vivo*. Unfortunately, such a technology does not exist due to the complexity, heterogeneity, and transient nature of the *in vivo* system. An alternative approach is to use an *in vitro* model to study bone mineralisation. High resolution electron microscopy studies have shown the occurrence of extracellular matrix vesicles (MVs), suggesting that mineralisation is mediated through a cell-mediated process. Several studies also have shown the existence of intracellular vesicles that contain calcium and phosphate, which are potentially the precursor of MVs. By contrast, other studies have provided evidence that mineralisation of the bone matrix occurs via an acellular route.

Questions remain about the step-by-step process by which bone mineral matures. The aim of the first study in this thesis is to focus on the extracellular matrix in bone and characterise the morphology and physio-chemistry of extracellular *in vitro* bone-like mineral as it matures. Specifically, the focus is in:

- identifying the localisation of bone-like mineral, in relation to the collagen fibrils by assessing (with TEM) heavy-metal stained sections of mineralising *in vitro* primary mouse osteoblasts cultures prepared with a protocol that preserves the mineral properties;
- characterising different mineral morphologies present within the culture by assessing (with TEM) non-stained sections of mineralising *in vitro* primary mouse osteoblast cultures;
- comparing the different mineral morphologies with those reported in literature to determine the relative stages of the mineral; and
- characterising the chemistry of the minerals through EDX and EELS compounded by high resolution imaging to provide a better understanding of the evolution of the chemistry of the *in vitro* bone-like mineral as a function of time.

1.2. Understanding the Effect of Strontium Ion Supplementation to *In Vitro* Bone Cell Culture

With the high monetary and quality of life costs associated with osteoporosis, it is of interest to study how one of the latest and most popular anti-osteoporotic drugs, Protelos®, effects bone mineralisation. This Servier's anti-osteoporotic drug uses strontium ions (in the form of strontium ranelate salt) as its active ingredient. Many positive effects of strontium treatment on bone mineralisation have been reported including increased bone strength and mass with the increase in bone volume and trabecular number and thickness. These positive effects have led to the reduction in the risk of fractures and to the significant improvement of quality of life. In the effort to elucidate the full mechanism of action, a number of studies have focused on exploring the effect of strontium supplementation on the mineral component of bone. However, numerous questions remain as to how strontium ions work in bone mineralisation, especially with regards to understanding their effect on the matrix component of bone.

To study the effect of strontium supplementation in bone mineralisation, especially on the matrix component of bone, Raman spectroscopy and TEM observation were used [3-7]. With Raman spectroscopy's ability to quickly screen various parameters, the effect of strontium on bone mineralisation and how strontium affects bone cells and matrix could be understood further. Combined with TEM's high resolving power, this second study provided a holistic view on how strontium affects the *in vitro* matrix.

Utilising Raman spectroscopy, TEM analysis, and biochemical analysis, the focus of the second study was on:

- verifying the potential of an osteoblast cell line (MC3T3-E1) as a model of primary osteoblast cells to study bone mineralisation and optimising the mineralisation condition for MC3T3-E1 to avoid concerns for spontaneous precipitation in the media by having a high concentration of a phosphate source (in the form of ß-Glycerophosphate);
- optimising the appropriate amount of strontium chloride supplementation to achieve *in vitro* matrix mineralisation. Control groups used no ion supplementation and strontium ranelate salt;

- analysing hydrated MC3T3-E1 monolayer by Raman spectroscopy to understand how strontium affects the matrix in its chemical level;
- analysing collagen fibrils submicron morphology through TEM micrograph;.
- quantifying the organisation of collagen fibrils by TEM image analysis to deduce if strontium supplementation may add a physiochemical parameter to affect collagen fibrils organisation; and
- quantifying hydroxyproline and DNA on MC3T3-E1 monolayer to observe how the amount of collagen is affected by different concentrations and forms of strontium supplementation.

2. Literature Review

This literature review chapter is sectioned largely into three parts: The first summarises common knowledge on bone structure and components. Studies in how bone is formed (i.e. bone mineralisation) will be reviewed in the second section. Lastly, strontium's effects on bone and its potential mechanism will be summarised on the last section. Following that, a brief mention on the *in vitro* cell culture models used in this thesis will be presented.

2.1. Bone

'Bone is a rigid form of connective tissue in which the extracellular matrix is impregnated with inorganic salts, mainly calcium phosphate and carbonate, providing hardness' [8]. Bone is most commonly known for giving body shape and support (mechanical function). There are, however, other functions of bone, including storing calcium and phosphate, providing sites for fat storage, and providing sites for red blood cell production [9]. In this part of the literature review, bone from its macroscopic features will be presented, followed by subsequent zooming in to its nano-scale components.

2.1.1. Macro- to Micro- Scale

Based on the observation of bone structure (macro-scale), mature bone is divided into two: compact and spongy. A brief description of these observations will explain bone's micro-scale organisation (Figure 2.1):

2.1.1.1. Compact (or Cortical) Bones

As described by its name, compact bone is densely packed (five to ten percent porosity [10]) with bone's natural scaffold (collagen fibers), and can be found in load bearing areas. Further microscopic examination reveals hierarchic structure that is called Haversian structure. In the centre of a Haversian structure is the Haversian canal. This canal is connected to other Haversian canals by Volkmann's canals, where blood vessels and nerves that support the cells within the bone. Concentrically situated around a Haversian canal are lamellar-structures (concentric lamellae; each 3-7 µm thick [11]), which are mineralised collagen fibres. Recently, it was observed that human lamella consist of collagen fibres that mostly aligned parallel to each other, with some looser packing disordered areas [12]. The spaces in between the concentric lamellae, called lacunae, host a type of bone cells called osteocytes. Three to eight lamellae make an osteon. [13, 14]

2.1.1.2. Spongy (or Cancellous or Trabecular) Bones

The spongy bones can be found at the end of long bones and inside the flat and cuboidal cortical bones. These bones are spongy with 50-95% porosity [10], do not contain osteons, and has trabecular arrangement of thin-column irregular lattice of bone (spicules). Red bone marrow fills the spaces between the trabecular. The outer surface of the cancellous bone spicules are covered by a single layer of flat "bone-lining cells" supported by a thin layer of reticular connective tissue. Bone forming cells (osteoblasts) and bone resorbing cells (osteoclasts), are also found within this cell layer [15]. Mature osteoblasts (osteocytes; see section on Bone Cells) of cancellous bone are present in the surface of the bone; they receive nutrient and oxygen from and directly exchange waste with the blood circulating through the medullary cavities [16].

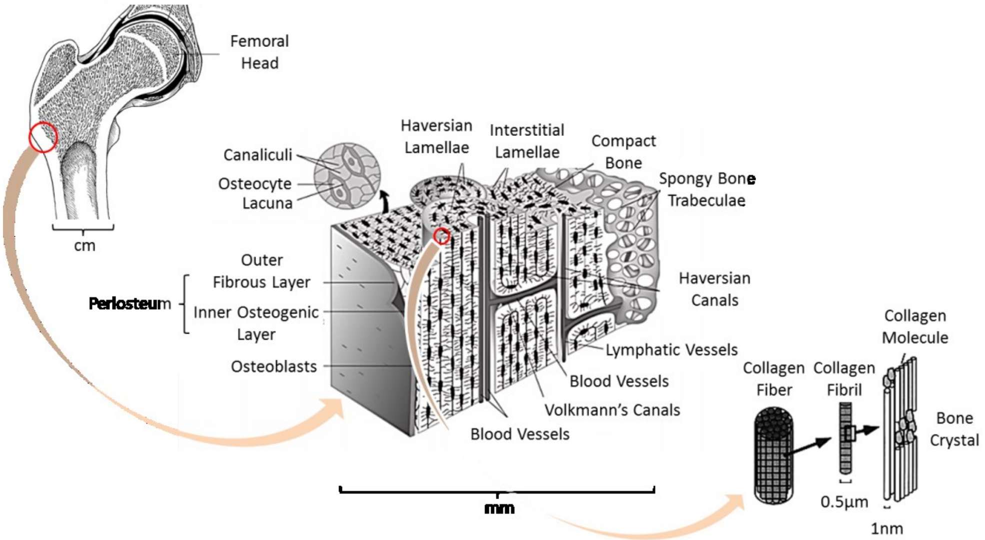

Figure 2.1 Hierarchy of bone structure. Bone is a macroscopic organ (length scale: centimetre) with components of various sizes forming a hierarchy in the nano- to centi-meter length scales. The macroscopic bone may be composed of both compact and spongy bone architecture. The compact bone is structured with Haversian structure that contains a busy network of cells and vessels (blood and lymphatic vessels). The spongy bone is made of trabeculae with high porosity. The matrix that is surrounding the cells and the vessels are made of mineralised collagen fibres. Figure is adapted from [17-19]

2.1.2. Micro- to Nano- Scale

2.1.2.1. Micro-Scale Arrangement

Looking at bone's micro- to nano-scale, bone is described in its material constituents and how these components are arranged. As a composite material that provides support to a body, bone's natural scaffold (collagen fibril) is interspersed with its ‘cement’ component of mineral. Based on the orientation of the collagen fibril, there are woven and lamellar bones.

2.1.2.1.1. Woven Bone

Woven bone is usually an immature bone; structurally, it consists of highly unsystematically arranged osteocytes [20]. The calcified matrix present in the woven bone is always permeated by collagen bundles that are not parallel to one another (unlike the tendency of that in lamellar bone); however, some degree of preferential orientation in the direction parallel to the long axis of the bone usually exist [21]. Having four to eight times higher osteocyte population than that of mature bone, woven bone is rapidly formed during bone healing [22].

2.1.2.1.2. Lamellar Bone

A mature bone, lamellar bone, consists of lamellar structures and makes up the compact bone. It is a remodelled woven bone, which begins to be formed one month after birth in human [23], and forms the flat bone as well as surfaces of long bones [24]. The highly structured lamella of the lamellar bone is stressed oriented, hence it has the highest strength along the parallel direction along the longitudinal collagen fibril [23].

2.1.2.1.3. Comparison between mineralisation of woven and lamellar bones

Woven bone is laid down quicker than lamellar bone is (i.e. >4 mm versus <1 μm per day). In woven bone, collagen is oriented almost randomly, unlike in lamellar bone. The spaces surrounding the osteocytes are extensive, unlike those in lamellar bone. The mineralisation process in woven bone involves roughly spherical centres that impregnate both collagen and grown substance simultaneously. These centres spread but also leave mineral-free spaces, making woven bone porous at the micron level. The mineral crystal of woven bone is also randomly oriented. Different from woven bone, many models have been proposed on how the mineral is arranged within the collagen fibrils of lamellar bone (Figure 2.2), and that lamellar bone has lower degree of mineralisation than woven bone has. [25]

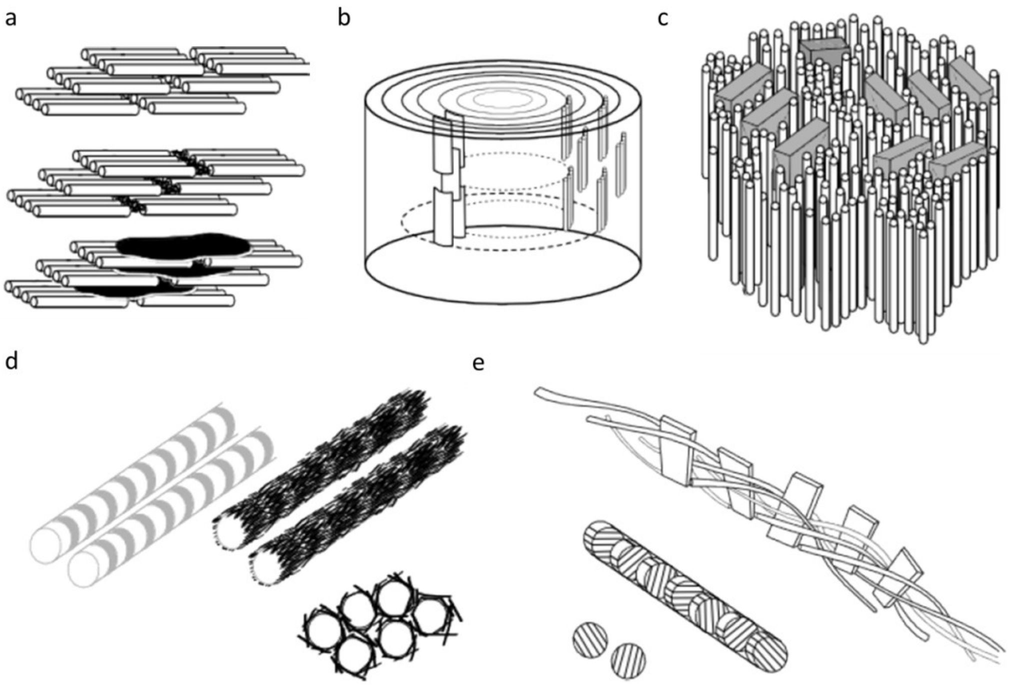

Figure 2.2 Various models showing collagen and mineral arrangement in lamellar bone. Collagen fibrils (a; top) acts as a template for mineral nucleation, where mineral can start to nucleate between the gap zone (a; middle) and later grow to mineralise the rest of the fibrils (a; bottom) [26]. Collagen fibril and mineral crystals (absent here) are arranged in concentric layers (b) [26]. Mineral crystals (represented in blocks) randomly distributed among the collagen molecules (represented in tubes) (c) [27]. Extrafibrillar mineral crystal forms crust around collagen fibrils (d) [28]. Collagen molecules intertwine around various crystal alignments, and the crystals align separately in each gap (e) [29].

Zooming in into the components that make woven and lamellar bones, there are organic and inorganic parts:

2.1.2.2. Organic Components

2.1.2.2.1. Collagenous Protein

Type-I Collagen is the most abundant extracellular protein of bones [30]. In general, three collagen polypeptides (two α_1 and one α_2 chains [31]) assemble into a procollagen molecule [32] that has left-handed triple helix motif. Each polypeptide is composed of Glycine-X-Y repeats [33], where in ten percent of the cases, X and Y are proline and hydroxyproline, respectively [34]. Each chain is composed of 337-343 Glycine-X-Y repeats [31], which translates to a total length of the molecule equal to 300 nm [35]. The diameter of the coiled triple helix chains is 1.5 nm [35].

Since the procollagen peptides are assembled from different amino acids, many types of collagen can form, and have been discovered; so far, there are 28 types found [36]. The most widely occurring collagen, type-I collagen, is present in bone, and is secreted by osteoblasts (See next section) [37]. Its procollagen peptide is matured by having its ends cleaved and arranged into quarter-staggered parallel fibrils (Figure 2.3) [30]. The defined and specific banding pattern of collagen fibrils with periodicity (D) of 64-67 nm that is seen by TEM is the result of this staggered arrangement (Figure 2.4); the size of the gap between the fibrils (gap zone) is 40 nm [31].

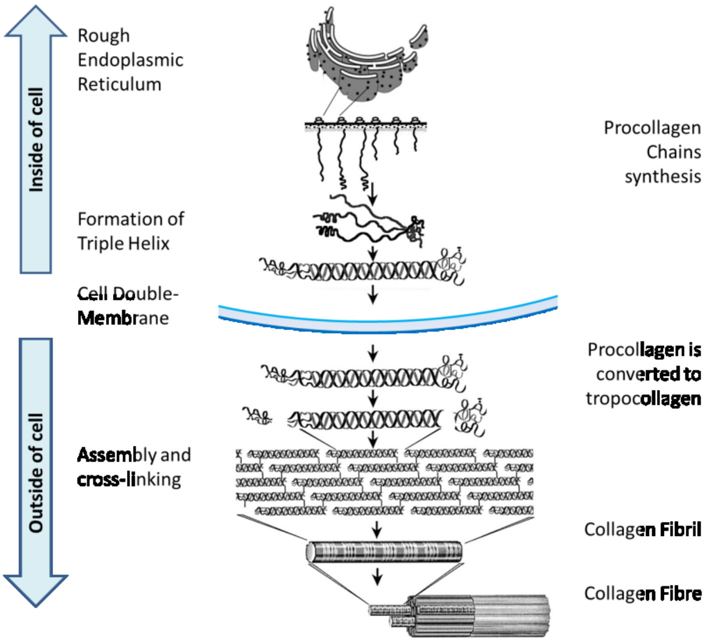

Figure 2.3 Collagen synthesis begins inside the osteoblast cells, which produce the procollagen and its subsequent assembly into a triple helix. Once the triple helixes are transported to the extracellular environment, the strands matures up by having the ends cleaved, and getting cross-linked in a quarter staggered formation to form the fibril. Figure adapted from [38].

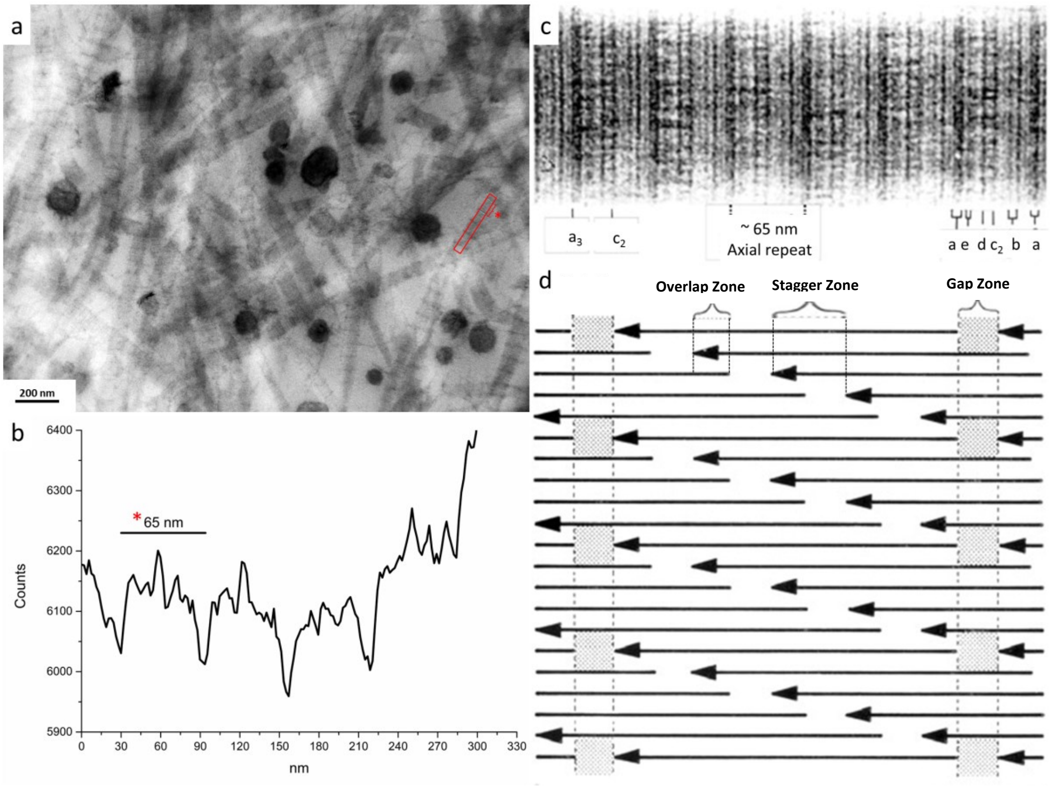

Figure 2.4 A TEM micrograph of MC3T3 at day 14 grown in mineralising medium supplemented by 3 mM $SrCl_2$, showing collagen fibrils and extracellular vesicles (electron dense (black) globules) (a). Line profile of figure a shows the intensity of pixels within the area selected in red. The red asterisk (*) shows the size of one fibril banding pattern (b). Higher resolution of negatively stained collagen showing the various banding pattern; the ~65 nm axial repeat is the length of the gap zone (40 nm; located between a_3 and c_2 bands) with the length of the overlap zone (c). A schematic of collagen quarter-staggered arrangement showing its various zones (d). Figures c and d are adapted from [39].

2.1.2.2.2. Non-Collagenous Protein

Besides the collagenous proteins present in bone, non-collagenous proteins (NCP) make up ten percent of the organic component of bone. There are several classes of NCP: proteoglycans, hyaluronan, glycoproteins, serum proteins, and ɣ-carboxy glutamic acid-containing proteins [40]. Some of the functions of NCPs are to give bones their elasticity [8], to provide interactive surface for protein binding [41], to modulate cell-matrix interaction [42], and to be involved in bone mineralisation events (as shown by the examples below). Several of the well-known NCPs are briefly explained below:

1. Osteocalcin

   A bone Gla-protein (a strong chelator of calcium ion [43]), osteocalcin is native to bone matrix (its vitamin K-dependent biosynthesis occurs in bone). Osteocalcin is the most abundant NCP of bone [44], and seems to be a highly specific osteoblastic marker produced during bone formation [45].

2. Osteopontin

   Osteopontin is a glycosylated phosphoprotein [46], and was observed to be produced several days before the onset of mineralisation by hyperthropic chicken chondrocytes [47]. Osteopontin is an inhibitor of *in vitro* hydroxyapatite crystal formation when phosphorylated [48]. Since osteopontin was observed to be localised at the mineralising front of developing bone, it suggests that osteopontin influence the rate of mineralisation instead of the nucleation of hydroxylapatite crystal growth [49, 50] (See section 'Inorganic Constituent (Bone Mineral)').

3. Bone sialoprotein (BSP)

   BSP is a bone-specific glycoprotein, and it was proposed to be involved in the nucleation of hydroxyapatite crystals at bone's mineralising front [51]. It promotes attachment and spreading of various cells, and has been implicated as a nucleator of apatite crystal in mineralising tissues [52].

4. Osteonectin

   It is found in bone's trabecular and in the newly formed osteoid and occurs at higher levels in the matrix than in the cells of bone. It was reported that osteonectin binds mineral to matrix and can induce mineral deposition onto Type-I collagen [53].

5. Fetuin

   Accounting for 25% of NCP, fetuin-A is highly abundant [54], and has been shown to inhibit calcification [55]. It is shown in an acellular *in vitro* system that fetuin-A forms complexes with calcium phosphate, stabilising the mineral particles and preventing aggregation [56].

2.1.2.3. Inorganic Constituent (Bone Mineral)

Landis summarised that:

'A mineral is any class of substances occurring in nature, typically comprising inorganic species of definite chemical composition and usually of definite crystal structure. A crystal is classically a solid (in some cases a liquid) having a regular geometric shape with characteristic internal structure, enclosed by symmetrically arranged plane surfaces and intersected at definite and specific angles' [26].

Regardless of species or age, bone mineral consists of calcium-deficient apatite containing CO_3^{2-}, HPO_4^{2-}, OH^- and other trace elements in the crystal lattice such as fluorine, chlorine, and strontium [57]. Through X-ray studies, mature bone mineral has been identified to be similar to hydroxyapatite [58, 59]. Pure hydroxyapatite has the basic formula of $Ca_5(PO_4)_3X$, where X is calcium-channel ion most commonly a hydroxyl group (OH^-), a fluorine (F^-), or a chlorine (Cl^-). Its crystal unit cell, composed of $Ca_{10}(PO_4)_6X$, has lattice dimensions of $a = b = 9.398$ to 9.438 Å and $c = 6.868$ Å, with $\alpha = \beta = 90°$ and $\gamma = 120°$ [60, 61] (Figure 2.5).

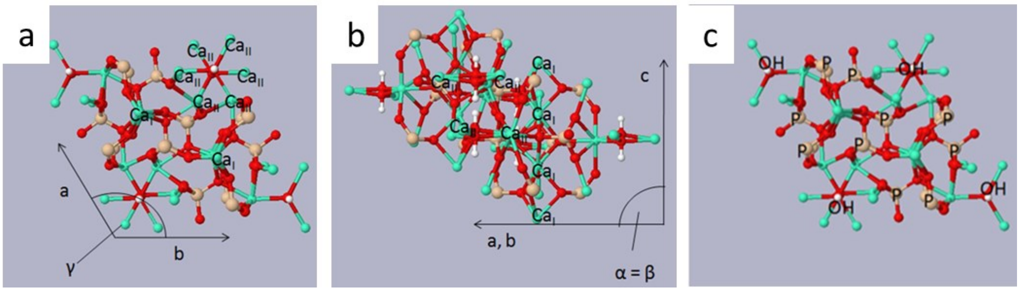

Figure 2.5 Pure hydroxyapatite atomic structure [62], consisting of two unit cells, viewing from the top (a and c), and side (b). Oxygen is coloured red, calcium with green, phosphorus with orange, and hydrogen with white. a, b, c labelled in the figures are the unit cell dimensions, and α, β, γ are the unit cell angles. Ionic substitution may occur in some sites of the crystal: calcium ions can be replaced by cations (e.g. Na^+, K^+, Mg^{2+}, Fe^{2+}, Zn^{2+}, Pb^{2+} or Sr^{2+}). Second, hydroxyl groups (OH^-) can be vacant or be replaced by F^-, Cl^- and CO_3^{2-} (also known as A-type substitution). Lastly, phosphate groups (PO_4^{3-}) can be replaced by CO_3^{2-}, SO_4^{3-} or HPO_4^{2-} (also known as B-type substitution) [39, 63, 64]. Figures were acquired from The United Kingdom Chemical Database Service [65].

Resembling hydroxyapatite, bone mineral can be represented by $Ca_{8.3}(PO_4)_{4.3}(CO_3)_x(HPO_4)_y(OH)_{0.3,}$ where y decreases and x increases with over time, and the sum of x and y always equals to 1.7 [57]. Bone mineral also contains Mg^{2+} (0.5%), Na^+ (0.7%), and trace amount of Cl^-, F^-, K^+, Sr^{2+}, and other metal ions [66] (Table 1). There are slight modifications of these trace components over time, and this aspect will be summarised in the later section (See section 'Changes during Mineral Maturation').

The shape of bone mineral crystal has been of controversy because of its unusually small size. Some older studies observed the plate-shaped bone crystal with the size of 45 x 30 x 2-4 nm [26, 67], while it was then suggested that there exist a 2-3 nm needle-like crystal population [68]. Bone mineral has a large specific surface of 100-200 m^2/g and high surface reactivity [66]. Demonstrated by X-ray diffraction, bone mineral contained a non-crystalline calcium phosphate phase [69]. It has been suggested that this amorphous calcium phosphate is the first phase formed in early mineralisation stages [70, 71]. Octacalcium phosphate ($Ca_8H_2(PO_4)_2.5H_2O$) was also suggested to be the precursor of apatite in bone [71-73]. Table 2 shows the different calcium-phosphorus based mineral identified in nature, and those that are present in biology.

Table 1 Some components of bone mineral obtained from whole bone not through ashing, Table is adapted from [74].

Component	Weight %
Ca	32.6-39.5
P	13.1-18.0
CO_2	3.2-13
Na	0.26-0.82
Mg	0.32-0.78
K	In the order of ~0.07
Sr	In the order of ~0.05
Cl	In the order of ~0.10
F	In the order of ~0.10
Ca/P molar ratio	1.61-1.87

Table 2 Known calcium orthophosphate. Biological systems, including bone, may be composed of species indicated by the check mark (√). Pure hydroxyapatite is never present in biological system. Calcium-deficient hydroxyapatite is the mineral found in mature bone. It has been proposed that initial bone mineral may be composed of octacalcium phosphate or amorphous calcium phosphate. Pure ß-tricalcium phosphate never occurs in biological calcification, except for its Mg-substituted form (i.e. whitlockite). Table adapted from [59].

Compound	Formula	Ca/P Molar Ratio	Solubility at 25°C (g/L)	Existence in biological system
Monocalcium phosphate monohydrate	$Ca(H_2PO_4)_2{\cdot}H_2O$	0.50	~18	
Monocalcium phosphate anhydrous	$Ca(H_2PO_4)_2$	0.50	~17	
Dicalcium phosphate dehydrate (i.e. brushite)	$CaHPO_4{\cdot}H_2O$	1.00	~0.088	
Dicalcium phosphate anhydrous (i.e. monetite)	$CaHPO_4$	1.00	~0.048	
Octacalcium phosphate	$Ca_8(HPO_4)_2(PO_4)_4{\cdot}5H_2O$	1.33	~0.0081	√
α-Tricalcium phosphate	$\alpha\text{-}Ca_3(PO_4)_2$	1.50	~0.0025	
ß-Tricalcium phosphate	$\beta\text{-}Ca_3(PO_4)_2$	1.50	~0.0005	√
Amorphous calcium phosphates	$Ca_xH_y(PO_4)_z{\cdot}nH_2O$ (n=3-4.5 or 15-20% H_2O)	1.20 - 2.20	Cannot be measured precisely	√
Calcium-deficient hydroxyapatite	$Ca_{10-x}(HPO_4)_x(PO_4)_{6-x}(OH)_{2-x}$ ($0<x<1$)	1.50 - 1.67	~0.0094	√
Hydroxyapatite	$Ca_{10}(PO_4)_6(OH)_2$	1.67	~0.0003	
Fluoroapatite	$Ca_{10}(PO_4)_6F_2$	1.67	~0.0002	
Oxyapatite	$Ca_{10}(PO_4)_6O$	1.67	~0.0870	
Tetracalcium phosphate (i.e. hilgenstockite)	$Ca_4(PO_4)_2O$	2.00	~0.0007	

2.1.2.4. Bone Cells

In the micro-scale, it would be incomplete to not include the presence and role of biological entities in bones. These entities are several kinds of cells that are crucial in the development and maintenance of bone as a whole:

2.1.2.4.1. Osteoprogenitor cells

Also called preosteoblasts, these cells are originated from multipotential mesenchymal stem cells that can differentiate also into chondroblasts, fibroblasts, adipocytes, and myoblasts [75]. Osteoblast precursors are likely located in the marrow space of the bone [76].

2.1.2.4.2. Bone lining cells

These cells cover the bone surface, and can be precursors for osteoblast cells when activated by chemical or mechanical stimuli [77]. Bone lining cells are flat (often less than 0.1 µm thick), and contain few cytoplasmic organelles because they are inactive cells [78].

2.1.2.4.3. Osteoblasts

Differentiated osteoprogenitors, osteoblasts are 10-20 µm in size. Mature osteoblast phenotype is characterised by the ability of the cells to synthesise membrane-associated alkaline phosphatase, bone matrix molecules (e.g. Type-I collagen, proteoglycans, hormone and growth factor receptors), and non-collagenous proteins (e.g. osteocalcin, bone sialopritein, and osteopontin) (see section on 'Organic Components') [77].

2.1.2.4.3.1. Osteoblast Maturation

Based on the function of morphology, three types of osteoblasts are identified at the bone surface: preosteoblasts, active osteoblasts, and inactive (or resting) osteoblasts. Preosteoblasts are located at a distance from bone surface and can still divide; they do not deposit bone matrix, but they produced collagen type I precursor molecules (to be later modified and assembled into collagen fibrils). Preosteoblasts differentiate into active bone matrix-secreting osteoblasts, which are typically cuboidal in shape (in mammals). [79]

Active osteoblasts do not divide. Unlike preosteoblats, active osteoblast are marked by upregulation of bone markers (such as bone sialoprotein, osteocalcin, decorin, several bone morphogenetic proteins, and collagen type I). Active osteoblasts secrete bone matrix, and 15% of the active osteoblasts become embedded in the cells secretory product called the osteoid, where mineralisation occurs in the adult skeleton. Osteoblasts that are embedded in osteoid are often referred to as young osteocytes. [79, 80]

When the osteoid mineralised, the young osteocytes decrease their protein synthesis and secretion. The bone markers previously expressed in active osteoblasts (such as osteocalcin, bone sialoprotein, collagen type I, and alkaline phosphatase) are down regulated or switched off as the osteocytes mature. [79]

With the three stages of osteoblast maturation, the formation of bone occurs in three phases: the production of osteoid matrix and its subsequent maturation, followed by mineralisation of the matrix. Initially, there the rate of matrix synthesis is higher than matrix mineralisation. It is then followed by the increase in the rate of matrix mineralisation to match the rate of matrix synthesis. Finally, the matrix synthesis subsides and matrix mineralisation continues until the osteoid becomes fully mineralised. [80]

2.1.2.4.4. Osteocytes

Being the most abundant of all bone cell types, osteocytes are terminally differentiated osteoblasts that are trapped within their own secreted osteoid. Mature osteocytes are stellate shaped or dendritic cells, and have relatively few organelles. Located in lacunae, each osteocyte is connected to the neighbouring osteocytes, or to the cells lining the bone surface by canals called canaliculi [81]. Young osteocytes have the more structural resemblance to osteoblasts than older osteocytes do [80]. Young osteocytes also decreased their cell volume and capacity for synthesising proteins as they mature [80]. It has been proposed that osteocytes are key to local bone remodelling by being the stress/load-mechanosensor of the bone: the combination of the porous lacunae-canaliculi system creates fluid shear stress that are detected by the three-dimensional network of osteocytes. Osteocytes may also contribute to homeostasis of calcium in blood [81].

2.1.2.4.5. Osteoclasts

Osteoclasts are responsible for bone resorption. They originate from the fusion of mononuclear precursors, which originate in the various hemopoietic tissues. They are large (20-100 μm) multinucleate cells which contain high density of mitochondria and lysosomal vesicles. When active, osteoclasts rest directly on the bone surface, and bone resorption takes place in the ruffled border of the plasma membrane. Osteoclasts solubilise bone mineral by creating local acidic environment. Osteoclasts produce proteolytic enzymes (e.g. cathepsin K) to degrade bone's organic matrix after bone mineral solubilisation [78].

Normal osteoclastogenesis involves a signalling pathway between osteoblasts and osteoclasts precursors [82]. Osteoblasts produce a protein called RANKL (or Receptor Activator of Nuclear Factor-κB Ligand) that will bind to a transmembrane protein called RANK (or Receptor Activator of Nuclear Factor-κB) on the surface of osteoclast precursors. This event will lead to an activation of NF-κB and its translocation to osteoclasts nucleus to later trigger the transcription of osteoclastogenic genes and the differentiation of osteoclast precursors to osteoclasts. To prevent excessive bone resorption by osteoclasts, a protein called osteoprotegerin (OPG) binds to RANKL and prevents RANKL from binding to its receptor (i.e. RANK) [82].

2.2. Bone Mineralisation

As summarised in the sections before, the function, components, and mechanical properties of bone has been well characterised. However, the mineralisation of bone matrix (i.e. 'how bone becomes bone') is a complex process and is still not fully understood. It is dependent on ion concentration and distribution, collagen arrangement, nucleation site characteristics and localisation. The sections below will describe the bone mineralisation mechanisms that have been proposed: bone matrix mineralisation (mineralisation on collagen template) and cell-regulated mineralisation. Following how the mineral is 'directed' to the matrix, a review on changes in mineral maturation will be presented.

2.2.1. Bone Matrix Mineralisation

In 1990, Lee and Glimcher utilised high-voltage electron microscopy and stereomicroscopy, electron probe micro-analysis and diffraction, and computer reconstruction to examine the relationship between bone mineral and collagen fibrils of pickerel and herring bone. They observed that in the early stage of mineralisation, apatite crystals were found to locate only within the collagen fibrils (i.e. no apatite crystals were observed in the collagen-free extracellular space) [83]. A decade later, Nudelman *et al.* combined cryogenic transmission electron microscopy and tomography on reconstructed collagen fibril *in vitro* (in the absence of cells) [84]. The study confirmed that the mineral nucleation occurs in gap junction domain of the collagen fibril [83] as the result of the strong interaction between positively-charged collagen fibril domain and the negatively-charged surface of apatite complex [26, 85, 86] (Figure 2.6). Specifically, the amino acid residues present in the gap zones of collagen are highly likely to bind to calcium and phosphate ions, and as such acting as nucleation sites and the subsequent growth of apatite crystals [87]. In Nudelman's time course study, mineralisation of calcium phosphate particles were first found outside the fibril (near the gap zone), associating with the fibril's overlap region. Subsequently, the apatite crystals started to develop and grow within the amorphous calcium phosphate (ACP) bed, embedded within a less dense matrix [84].

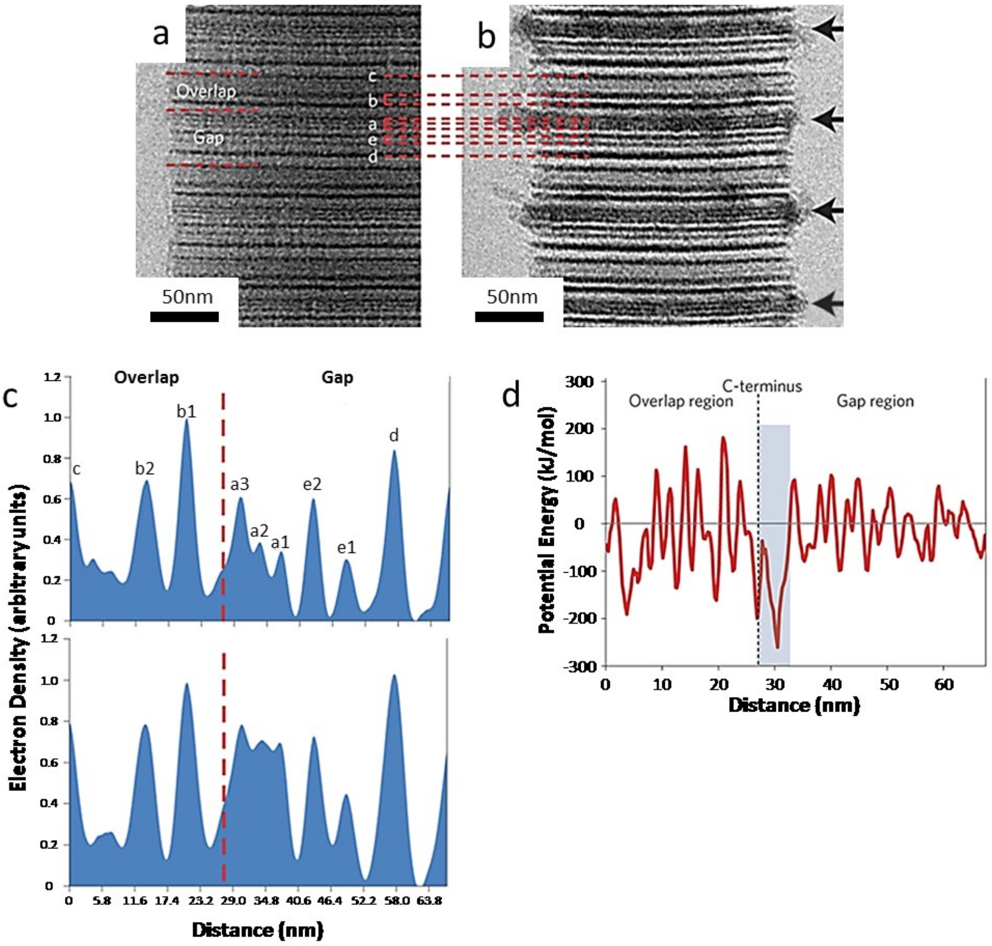

Figure 2.6 Stained, non-mineralised collagen showing overlap and gap regions (a). Collagen in mineralising solution for 24-hour, showing amorphous calcium phosphate preference in the a-regions (arrows) (b). Intensity profiles of non-mineralised (top) and mineralised (bottom) collagen, showing increased intensity at the a-regions after 24-hour of mineralisation (c). Electrostatic potential energy calculated by atomistic modelling shows that the shaded area has the lowest potential energy and the most favourable for interaction with negative charges, which coincide with the a-regions (d). Image is adapted from [84].

Other previous studies have shown the great deal of NCPs involvement in mineralisation. In general, the polyanionic feature of NCPs is thought to be contributing to matrix mineralisation; for example, their presence can inhibit hydroxyapatite nucleation when in soluble form and promote nucleation when attached to a substrate [88]. Another example, the negatively charged surface of osteocalcin was shown to coordinate five calcium ions in a spatial orientation that is complementary to calcium ions in a hydroxyapatite crystal lattice [44]. In another study, in the presence of osteonectin, bone Gla protein and dentine phosphoprotein, a greater accumulation of inorganic phosphate was needed for calcium phosphate to precipitate, suggesting that a higher degree of supersaturation is required for calcium phosphate to precipitate [89]. In short, these studies show that collagen fibrils, along with non-collagenous proteins, are able to initiate precipitation and direct the growth of the minerals.

2.2.2. Cell-Regulated Mineralisation

2.2.2.1. Extracellular Vesicles or Matrix Vesicles

As the name suggests, the studies under the umbrella of 'cell-mediated mineralisation' put forward the involvement of cells for mineralisation to occur. Many observations have made extracellular 'matrix vesicle' (MV) a widely-accepted theory for how bone mineral is packaged initially. MVs were first observed in cartilage's growth plate in 1960s. They were seen as the initial sites of mineral formation before matrix mineralisation [90-92]. As more studies were conducted, matrix vesicles were found in not only cartilage growth plates, but also around osteoblasts, ondontoblasts, and tenocytes [91, 93-97]. Comparing the relative amount of matrix vesicles found in cartilage and those found in bone, significantly more matrix vesicles was obtained per gram tissue of cartilage than those of bone [98]. It was suggested that only relatively small proportion of bone is undergoing active mineralisation compared to that of cartilage, and hence bone does not contain as many intact matrix vesicles as cartilage does [98].

In 1976, Anderson and Rabinovitch proposed four hypotheses regarding biogenesis of matrix vesicles in cartilage growth plate [99] (Figure 2.7):

a) MVs are the result of budding or detachment from elongated cellular processes.
b) MVs are formed as extrusion of vesicular structures that have been fully preformed within the cell.

c) MVs being the product of cell death (cellular degeneration and disintegration).
d) MVs' components are intracellularly formed before being secreted to the extracellular area to self-assemble.

Some evidences obtained based on ultrastructural and protein-based studies support the hypothesis that MVs originated from polarised budding from the cell's plasma membrane [91, 93, 100-102].

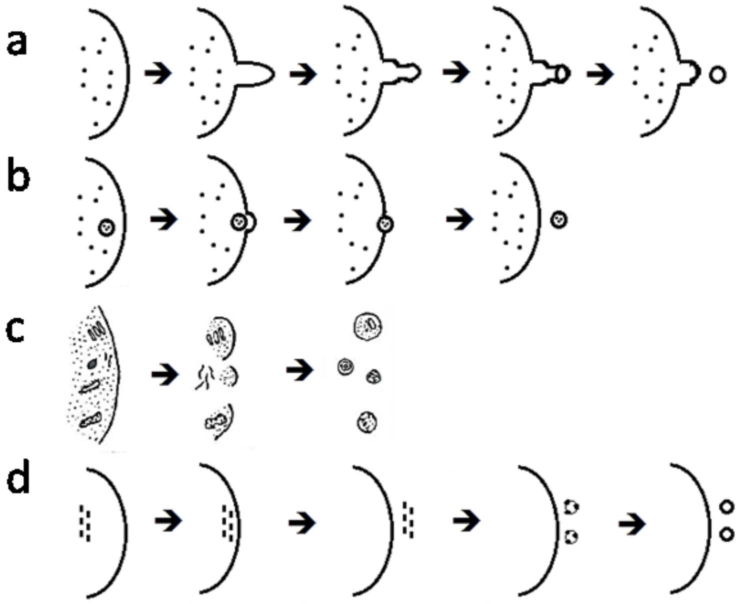

Figure 2.7 Hypotheses on biogenesis of matrix vesicles in cartilage growth plate. MVs can be the result of budding or detachment from elongated cellular processes (a); MVs can be formed as extrusion of vesicular structures that has been fully preformed within the cell (b); MVs being the product of cell death (cellular degeneration and disintegration) (c); MVs' component are intracellularly formed before being secreted to the extracellular area to self-assemble (d). Figures are adapted from [99].

Extensive research over the years have shed some lights into the characteristics of MVs. It was observed that the concentration of calcium in matrix vesicles is 25-50 times higher than that of their adjacent cells, and that MVs' calcium to phosphate molar ratio were much higher than those of cells or later mineral deposits [103]. Having abundance of inorganic phosphate and calcium ions, MVs provide a microenvironment and nucleation site for calcium and phosphate crystallisation [104]. Matrix vesicle membranes are particularly enriched in membrane tissue-nonspecific alkaline phosphatase (tnALP) [105] and annexins [106, 107]. Alkaline phosphatase (ALP) hydrolyses phosphate from phosphate esters, providing the mineralising system with phosphorus. tnALP determines the normal steady-state levels of pyrophosphate [108], and mutations in the tnALP gene result in poorly mineralised bone, spontaneous fractures, and elevated extracellular concentrations of inorganic pyrophosphate [109]. Annexin II, V, and VI have been identified in MVs and extensively studied [106, 110-114]. Studies suggested that Annexins form channels in the MV membrane and mediate Ca^{2+} influx into the vesicles [111, 115]. A more recent finding showed, however, that using knock-out mice, annexin V is not essential for skeletal development [116] and that deficiency of annexin V and VI does not inhibit the induction of mineralisation [117].

With regards to MVs calcium-phosphorus contents, X-ray diffraction of Isolated MVs showed amorphous mineral [103, 118]. McLean *et al.* indicated that the calcium and pyrophosphate ions are not coupled together initially in the MVs. A fourier transform infrared spectroscopy (FTIR) study on isolated MVs induced to mineralise in synthetic cartilage lymph confirmed that the initial calcium-phosphate in MVs is not crystalline, and that the first crystalline phase is octacalcium phosphate (OCP), which was, over time, transformed into a more hydroxyapatite-like mineral [119].

2.2.2.2. Intracellular Vesicles

More recently, initial bone mineralisation studies mentioned the involvement of intracellular vesicles that sequester calcium ions. For instance, in two consecutive years, Mahamid *et al.* and Boonrungsiman *et al.* used *in vivo* mouse and *in vitro* mouse osteoblasts models, respectively, showing the presence of intracellular vesicles with 70-80 nm calcium-containing granules [120, 121].

Mahamid *et al.* showed, using cryoSEM, that the bone-lining cells of developing mouse calvaria and long bones concentrate membrane-bound mineral granules within their intracellular vesicles [121]. These granules were analysed to consist of the highly metastable potential precursor of carbonated hydroxyapatite, the disordered calcium phosphate [121]. Similar intracellular calcified vesicles was observed by Rohden and Mayer in *in vitro* bone marrow stroma cells [122] and Carter *et al.* in frozen-prepared tissue [123]. Much is yet revealed about these observed intracellular vesicles in their translocation and their role in bone mineralisation. Mahamid *et al.* argued that these intracellular packages advantageously facilitate the transport of mineral precursor without much water lost. Further, this form of transport also allows the mineral precursor to arrive in the collagen matrix in the form that can penetrate through the gaps of the collagen fibrils [121]. In their extensive TEM studies, Boonrungsiman *et al.* further showed that these intracellular vesicles received their calcium content as they interact with mitochondria, which are known to be organelles that maintain the presence of ionic and granular calcium [120, 124]. Essentially, the studies mentioned above further hypothesised the cellular-origin of matrix vesicles, and where the mineral precursor comes from.

2.2.3. Changes during Mineral Maturation

The phase of mineral deposited on collagen and its subsequent transformation have been studied and revised with better equipment being used over the years. The advent of Röntgen’s X-ray increased our understanding in bone mineral; and a review article in 1950, summarised the knowledge of bone’s inorganic component to be exhibiting x-ray diffraction pattern of carbonated apatite [125]. This mineral crystal is shown to be increasing in size overtime from less than 50 Å particles to as much as 1500x500x100 Å on senile human; similar trends are also observed in other animals [57, 126, 127]. This growth of the crystal is found to be more rapid in the *a*-axis, even though its *c*-axis is initially larger [127]. On the crystallinity of bone mineral, an *in vivo* (rat model) study done by Posner *et al.* [128] confirmed that bone mineral is poorly crystalline shortly after birth, and the crystallinity improves overtime; this observation is later confirmed by others [129-131].

In terms of morphology, maturation of mineral brings changes to the mineral shape. *In vivo* cryo-SEM studies of the growing fin of zebra fish showed that the mineral started out as globular entities (200-500 nm diameter) that consist of nanospherical subparticles (10-15 nm diameter) [129, 132]. Overtime, the mineral is observed to assume the shape of platelets, before joining to the bulk of the mineralised matrix. Similar observations were reported in an *in vivo* rat system [121].

An attempt was done to understand the full picture of the morphological maturation of calcium phosphate. In the study of an acellular and inorganic system [133], various morphologies were observed overtime as calcium and phosphorus sources were mixed in ‘test tubes’. Two routes of mineral maturation were observed (Figure 2.8):

1) Calcium phosphate strands consisted of nanometer-sized units were formed in less than two minutes, followed by their assembly to one another to make branched aggregates (called ‘pre-nucleation species’). After 10-20 minutes, spherical nodule (around 100 nm diameter; called ‘post-nucleation species’)

consisting of nanometer-sized components formed, and then transformed ribbon-looking aggregates at 80-110 minutes.

2) Formation of ribbons directly from calcium phosphate strands at 60-110 minutes, before transforming into needles and elongated plates after 110 minutes.

The observations mentioned above [133] were done by mixing calcium and phosphate sources in a test tube without having any biological component, such as cells and extracellular matrix; hence, it is a very simplified environment. The previous paragraph (see 'Bone Matrix Mineralisation') presents some simplified acellular studies that used organic components (e.g. collagen and NCP) to better mimic bone environment.

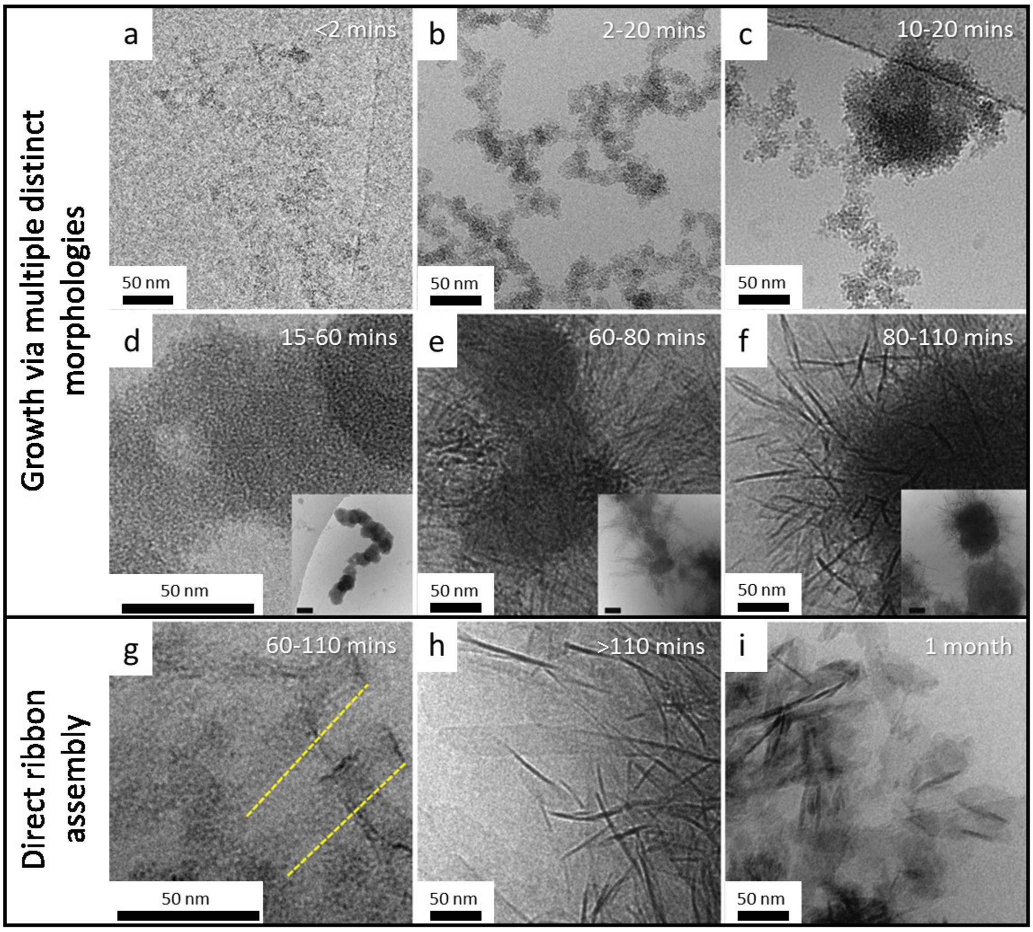

Figure 2.8 Growth of calcium phosphate by addition of phosphate solution into a gently stirred solution of calcium ions. Two paths of mineral maturation observed: growth via multiple morphologies (a-f) and direct ribbon-structure assembly (g-i). Growth via multiple morphologies starts with polymeric assembly (a) before forming branched aggregate (b). The branched aggregate then formed a post-nucleation species (c, d) before transforming to ribbon-like morphology (e,f). As the name suggests, direct ribbon assembly route involves the assembly of ribbon-like structure from calcium phosphate, bypassing the granule-formation step (g, h, i). Scale bar of the inserts are 100 nm. Figure adapted from [133].

Increasing maturity of mineral also is seen to be accompanied with the changing of mineral components. An observation shows a decrease of magnesium per gram bone during 4-22 weeks maturation rat bone *in vivo* [127]. The most common *in vivo* observation, however, is the calcium to phosphorus ratio's (Ca/P's) increasing with maturity [57, 121, 128, 129]. This trend is explained by the increased substitution of phosphate group (PO_4) by carbonate (CO_3^{2-}), while calcium per unit formula remains constant, making it B-type carbonated apatite [57, 127].

In vitro investigations have also been conducted [134, 135], and some differences are observed from that of *in vivo*. While poorly crystalline apatite is observed in both *in vivo* and *in vitro* system, the size of *in vitro* crystal deposited in earlier time point is larger than those in later time point [134]. Total carbonate content of *in vitro* bone mineral also decreased overtime, unlike in *in vivo*'s case [129, 134, 135]. In a study of mineral produced by chick osteoblast, octacalcium phosphate is not detected as of significant presence in the mineral. These contrasts are argued to be the result of differences in the local extracellular environment between *in vitro* and *in vivo* during mineral deposition and crystal growth [134, 135]. More recently, a study is proposing that the cells's carbonic anhydrase is acting as the bioseed-forming enzyme that synthesise calcium carbonate seeds before the calcium phosphate is then layered [136].

2.3. Strontium and Bone Mineralisation

Discovered near the Scottish village, Strontian, in the late eighteenth century [137], Strontium has been popularised in the twentieth century as the active ingredient of an anti-osteoporotic drug called Protelos® (by Servier) (Figure 2.9). In this part of the literature review, some evidences on the effect of strontium supplementation in bone mineralisation will be explained.

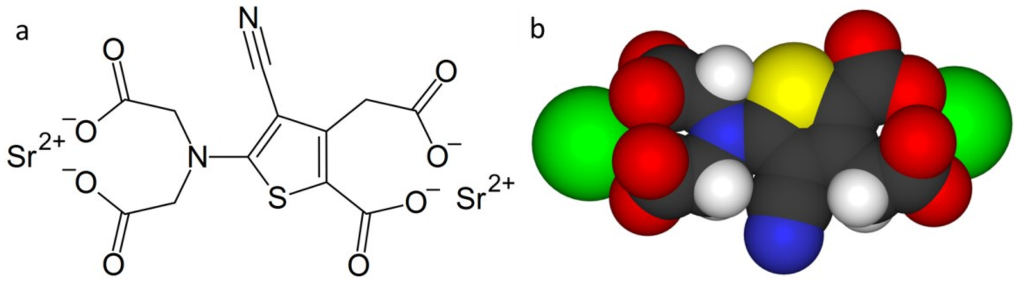

Figure 2.9 Chemical structure of strontium ranelate (a,b), the active ingredient of the anti-osteoporotic drug Protelos. In (b), strontium is pictured in green, oxygen in red, nitrogen in blue, sulphur in yellow, hydrogen in white, and carbon in grey. Images are taken from enacademic.com).

2.3.1. Early use of Strontium as Medicine

In the 1950’s, McCaslin and Janes described their success in treating osteoporosis patients using 1.7 g/day strontium lactate [138]. They showed that 84% of the patients have reduced bone pain, and showed improvements in the appearance of lumbar vertebrae on X-ray. This success was, however, not followed up by the medical and research communities until the early 1990’s, upon Servier’s development of strontium ranelate. Some of the reasons contributing to the gap in pursuing strontium as potential drugs for osteoporosis were:

1. Strontium’s reputation as a contributing factor to ‘strontium rickets’ when given to animals in high doses (i.e. an order of magnitude higher per kilogram of body weight than modern doses). This observation was later deduced to be caused by the decreases in bone calcium, rather than the high levels of strontium [139].
2. The production of radioactive and cancer-inducing strontium-90 from nuclear fission reactions that [140], albeit different from the harmless stable-strontium, is leading erroneous public view on the potential use of the naturally occurring stable-strontium in medicine.

2.3.2. Strontium as Treatment for Osteoporosis and Strontium’s Effect to Bone Components

Osteoporosis, a disease commonly known for occurring amongst postmenopausal women, is also found to affect men [141]. This disease is marked by low bone density and bone microarchitectural deterioration that cause bone to be prone to fracture [142]. This disease is caused by the gradual loss of balance between bone formation by osteoblasts and bone resorption by osteoclasts [143]; hence, the various treatment for osteoporosis can be broadly classified as anabolic treatment (those that increase bone mass) and as anti-catabolic treatment (those that decrease bone resorption).

As mentioned, strontium as a treatment of osteoporosis began to be popularised in the 1990s by Servier's Protelos®, and as such, many of the studies attempting to understand the effect of strontium come from studies of this strontium-ranelate salt conducted by this company. In summary, it was seen that strontium chloride supplementation in rats increased osteoid surface, osteoblast surface, and bone forming surfaces [144]. Bone resorbing cells are also seen to be transiently reduced with the strontium supplementation in mice [145]. Conclusive evidences from human studies also show that strontium ranelate treatment increased bone strength and mass with the increase in bone volume and trabecular number and thickness [146], which lead to the reduction in the risk of fractures and lead to the significant improvement of quality of life after five years of treatment [147, 148]. Strontium is found to be incorporated into the newly form bone [149-151], and it does not cause severe changes in the mineral substance [150, 152]. Table A 1 and a recent review [153] feature more evidences of strontium's effect on bone.

With evidences showing positive effect of strontium in *in vivo* bone, much effort has been done in finding out how strontium achieves those desirable effects. To try to tease out strontium's mechanism of action, many *in vitro* studies as simpler bone mineralisation models have been conducted. The following sections will present some findings on the effects of strontium on the components that make up bone: bone cells (cellular effect), bone mineral, and bone matrix (mineral and matrix effect).

2.3.2.1. Cellular Effect of Strontium Supplementation

Some studies have shown that strontium supplementation is affecting directly on osteoblasts and their progenitor cells (anabolic effect), as well as osteoclasts (anti-catabolic effect) [154-158]. With primary mouse calvarial osteoblast cells, Bonnelye *et al.* [156] studied the effect of primary mouse cells cultured with strontium chloride and sodium ranelate added to the culture medium (at a molar ratio of 100:1). Cells treated continuously with concentrations of 0.1, 0.3, and 1 mM Sr^{2+}, showed concentration-dependent and statistically higher mRNA levels of alkaline phosphatase, bone sialoprotein, and osteocalcin, as well as more bone nodule number at the observed time points of day 5 and 22. When the cells were only treated for the first five days of the 22-day culture, strontium-treated cells also resulted in significantly higher mRNA levels alkaline phosphatase, bone sialoprotein and osteocalcin, as well as higher bone nodule number, than those of the control group. This result suggests that strontium is not only increasing osteoblasts mineralisation, but also enhancing osteoblastic differentiation at the early stage.

Yang *et al.* observed that when primary human MSC (progenitor of osteoblasts) are exposed to 2 mM strontium chloride-containing mineralising media, more ALP, type-I collagen, and osteopontin were expressed after ten days (both gene expression and protein), as well as more bone nodules were produced at the end of the four-week observation, compared to those of cells treated strontium-free osteogenic media [159]. Peng *et al*. have also seen similar observation that 1-3 mM strontium chloride supplementation in osteogenic media for seven days increased osteoblast transcription factor RUNX2 mRNA, and increased bone sialoprotein and osteocalcin mRNAs after 14 and 21 days, respectively in murine mesenchymal stem cell cells (cell line) and primary murine bone marrow MSC, marking the increased commitment of MSC to osteogenic differentiation [160]. Furthermore, Fournier *et al.* also observed the significant increase in ALP and RUNX2 mRNA levels of mouse multipotent mesenchymal cells (from cell line) when treated with 3 mM strontium chloride-containing adipogenic media for five days [161]. They also observed after five days with 3 mM strontium supplementation, the mRNA expression of adipogenic genes (PPAR-γ2, CEBPα, CEBPß, and FABP4) decreased. This results show that strontium supplementation is able to inhibit effectively adipogenic genes and increased osteogenic genes, even as the cells were cultured in an adipogenic environment.

A more recent study by Bakker *et al.*, improved our understanding of the effect of strontium supplementation to the signalling between osteocyte and osteoblasts and osteoclasts precursors [162]. In the study, osteocytes (cell line) were cultured for 24 hours with up to 3 mM strontium ranelate (made by combining 100:1 molar ratio of strontium chloride and sodium ranelate), and with or without mechanical stimulation for one hour (by pulsating fluid flow). This condition media was then used to culture primary mouse pre-osteoclasts (bone marrow cells) or pre-osteoblasts cells (cell line). On the pre-osteoblasts, only those treated with the condition medium free of strontium (both with and without mechanical stimulation) had the changes in the expression of osteogenic mRNAs (Ki67, Runx2, and osteocalcin); it was argued whether strontium supplementation altered the response of osteocytes to the mechanical stimulation. When pre-osteoclasts are cultured with the condition medium, most pronounced inhibition to osteoclast number was achieved when the condition medium was obtained from the mechanically stimulated osteocytes treated with 3 mM strontium ranelate. This shows that the supplementation of strontium affects the signalling molecule released by mechanically-stimulated osteocytes and enables the suppression of osteoclast formation.

Besides osteoblasts and their precursors (i.e. MSCs) and their matured form (i.e osteocytes), the effect of strontium supplementation has been previously studied to other bone cells such as osteoclasts and their precursors. In depth discussion on how strontium affects them is beyond the scope of this thesis; to summarise, strontium supplementation was found to be inhibiting osteoclast formation (measured by quantification of TRAP activity after eight days) and resorption (after two days by visualisation and quantification) by murine primary *in vitro* osteoclasts with concentration as low as 0.1 mM [156, 163]. The lower resorption was seen to be contributed by the decrease in ruffled border formation by osteoclasts [163].

The mechanism of action of strontium in osteoblasts and osteoclasts are yet fully understood. One of the ways that has been thought to be involved in strontium's affecting the cells is its similarity to calcium ions. Because of that, strontium ions are thought to be an agonist to calcium sensing receptors (CaSR) in osteoblasts and osteoclasts, although with lower affinity than calcium [157, 164-166]. It was found that strontium ions promote osteoblasts proliferation [167], differentiation, and mineralisation [168] by stimulating CaSR. When a CaSR inhibitor was introduced, the effect of strontium-induced mineralisation and proliferation was abolished [168], further confirming the activation of CaSR by strontium ions. Through CaSR in osteoclasts, strontium was found to induce osteoclast apoptosis [169].

The difficulty in distinguishing the effect of calcium to that of strontium in the cell culture system has made complete understanding of strontium's mechanism of action challenging. The complexity of bone cells also adds to the intricacy of isolating the exact mechanism(s) that strontium ion may be involve in. As an example, apart from strontium's mechanism of action through CaSR, Fromigue *et al*. also found that CaSR is not the only receptor involved in stimulating osteoblasts [170]. Their study showed that, independent of CaSR expression (i.e. through ERK1/2, Akt signalling, and PGE2 production), strontium increased osteoblasts proliferation and protected osteoblasts against apoptosis [170]. In fact, there are many studies presenting other evidences on the mechanisms of action strontium has effect on other cells such as osteoclasts, osteocytes, bone marrow, and mesenchymal cells, however as strontium's pathways are beyond the scope of this thesis, readers are advice to refer to [153, 171-173].

2.3.2.2. Mineral and Matrix Effect of Strontium Supplementation

Boivin, *et al*. [174] summarised that a crystal environment can be modelled by four compartments:

1. Outside of crystal: bulk solution
2. Outside of crystal: hydration shell (polarisable ions bound to crystal)
3. Crystal surface
4. Crystal interior

Interaction between the ions in the bulk solution and the crystal can occur by different means. First, adsorption phenomena can occur on the surface of the crystal, mainly to stabilise the mineral's the surface energy. Second, substitution of atoms or moieties of crystal can occur with the ions that are present in the bulk solution (heterionic substitution). The latter mean is affected by the size of the new atoms or moieties, and hence may change the crystal shape and size at the bulk and unit cell levels. [174]

Exposing *in vivo* bone or *in vitro* mineral (e.g. in cell culture experiments) to strontium ions may change the property of the mineral with the pathway(s) mentioned above. As bone's inorganic mineral gives bone its mechanical strength, it is important to gain insight on how strontium interacts with bone mineral, and the effects thereof. Here, some of the existing studies are presented:

In vivo studies have shown that strontium is taken up at the bone tissue level [149, 175-178]. These studies saw the dose-dependent strontium incorporation into newly formed bone *in vivo* [152, 177, 179]. The findings posed further questions on where exactly the strontium is located: in the collagen or in the mineral. Moreover, should the strontium be located in the mineral, whether strontium is incorporated into the mineral crystal (hence, changing the lattice parameters, crystal sizes, and crystallinity of the mineral) or just merely being adsorped.

Studies have revealed that strontium is both adsorped on the surface and incorporated to the crystal lattice [150, 152, 177, 180]. It is found that heteroionic substitution is around 0.5 to 1 calcium ions substituted in 10 calcium ions [150, 152, 177]. More recently [181, 182], it was found that the substitution of calcium ion by strontium ion did not change the overall cation to phosphorus ratio (i.e. calcium to phosphorus, or [calcium + strontium] to phosphorus ratio) and mineral crystallinity (compared to that of non-strontium substituted apatite mineral); however, type-B carbonate mineral substitution was seen to be increased with strontium substitution, which may be resulting in the observed increased of mineral's lattice parameters *a* and *c*. Phosphate environment of the mineral was also seen to be changed with strontium substitution, which may be the result of the changed lattice parameters.

As mentioned, strontium can also be interacting with bone matrix (i.e. mainly collagen type I) (Figure 2.10). X-ray absorption spectroscopy was used to determine the relative amount of strontium incorporation in various component of bone matrix [183]. The study found that approximately 35-45% of the strontium present is incorporated into the bone mineral by heteroionic substitution, at least 30% is located in the surface of the mineral, and the remaining is located in the matrix. Minimal number of *in vivo* studies showed that collagen cross-linking, which often contributes to better bone physical quality, was not altered by strontium ions macroscopically [151, 184]; however, it is argued in another study that the strontium interacting with the collagen may still be involved in the cross-linking of collagen, as well as collagen and mineral ionic coupling [183].

The effects of strontium in the mineral and matrix of bone were isolated by Cattani-Lorente, *et al.*, who incubated dried bone in strontium solutions (with calcium and barium solutions as controls) [185]. The study showed that incubation in strontium ions increased in bone's elastic modulus, hardness, and working energy (energy dissipated during the deformation) in significant manner. Since this system is acellular, it is revealed that strontium may modify bone's intrinsic property independently of its cellular activity. However, since these effects were also seen with the calcium and barium treatments (as controls), it is plausible to infer that the positive results shown here are the result of adding 2+ cations to the system, which change the ionic strength and ionic interaction in the solution.

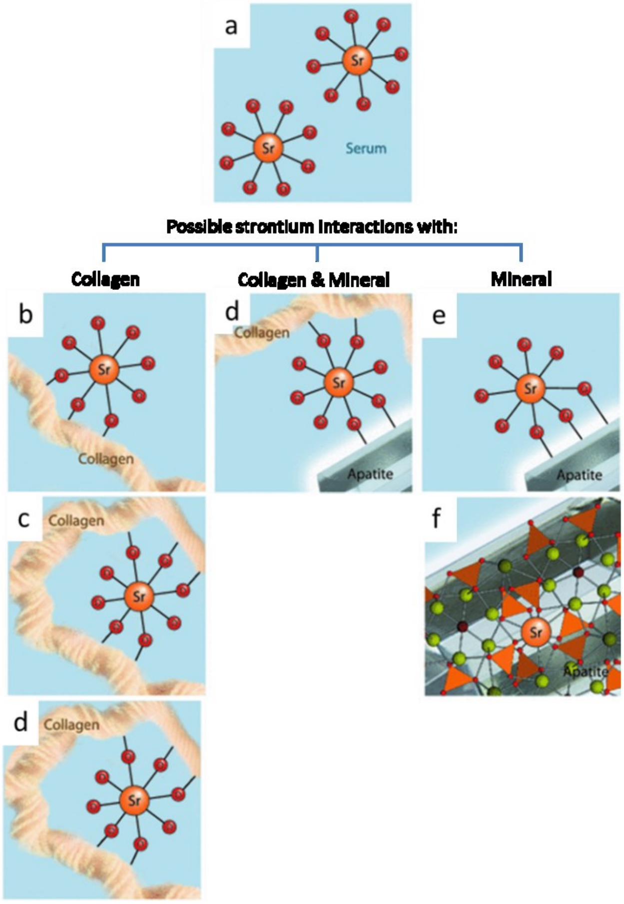

Figure 2.10 Possible interaction cites of strontium: Strontium ions in the serum (a) can be interacting solely with the collagen of the bone matrix by being adsorped to collagen's surface (b), or providing intra- (c) or inter-fibrillar cross linking (d). Strontium can also provide ionic coupling of collagen and mineral surface (d), be adsorped to the mineral surface (e) or be incorporated into the mineral crystal (f). Figure adapted from [183].

2.3.3. Motivation for Further Study on Effect of Strontium Ion in Bone Mineralisation

With the summary presented in the preceding sections, the effect and mechanism of action of strontium is yet to be fully revealed. One of the reasons that may be contributing to this is that most of the studies were not completely controlled: the strontium-supplemented groups are often only compared to strontium-free control groups [144-148, 154, 186-196], and lack the comparison to the groups supplemented with other divalent ions (such as calcium [155, 197] or barium [185]) or other ions (e.g. sodium) to maintain ionic strength [155, 185].

It has also been challenging to compare the results between studies as differences in cell types (or type of organisms, in *in vivo* cases), culture media and serum. Further, the concentration of strontium supplementation are obvious: *in vivo* strontium serum level of osteoporotic patients treated with 2 g/day strontium ranelate were measured to be in the order of 0.1 mM [165]; however, *in vitro* systems used in many studies were supplemented with 1 mM or greater than 10mM strontium supplementation [154, 155, 162, 169, 188, 198]. It has been argued in some studies that in the vicinity of bone remodelling, high strontium concentration may be found when osteoclasts are dissolving the bone [169]. However, it can be also suggested that since only up to ten percent of calcium ions of bone calcium is replaced by strontium ions [152, 177, 178], the concentration of strontium around the cells may be 0.8-4 mM [169], which is lower than some of the concentrations used in several studies. The results gained from exposing cells to very high amount of strontium warrants a cautious interpretation as the strontium concentration maybe more than 100 folds of *in vivo* concentration.

As mentioned in the earlier section, the research on strontium action as an anti-osteoporosis drug is mainly done or sponsored by Servier. It could be speculated that conflict of interest may bias the experimental set up or parameters or data treatment in the published studies. It is evident that in the earlier strontium studies, much positive effects of strontium in both *in vivo* and *in vitro* studies were shown (refer to Table A 1). Recently, however, some studies are published with results challenging the earlier results:

Chavassieux et al. conducted studies on osteoporotic postmenopausal women treated with 2 g/day strontium ranelate in a multicentre, international, double-blind, and controlled way: 387 patient’s transiliac bone biopsies were performed at baseline and at 6 or 12 months, and bone histomorphometric parameters were analysed [199]. They showed that the bone formed during the treatments did not show mineralisation defect. With close inspection on the data, however, it shows that statistically significant increase of the parameters of bone formation[1] and bone resorption[2] were not achieved at the end of the study. With this result, anabolic and catabolic actions could not be demonstrated on bone remodelling in patients treated with strontium ranelate, hence not providing an explanation for its beneficial effect

---

[1] i.e. osteoblast surfaces, and osteoid surfaces, volume, and thickness

[2] i.e. eroded surfaces, osteoclast number and surface, mean and maximum erosion depth, and eroded volume

on bone strength that was shown from earlier studies (refer to Table A 1). It is argued that this study offers its longitudinal design with high number of paired-biopsy samples; however, this two dimensional histomorphometry approach on non-weight-bearing bones (i.e. negligible mechanical pressure) may be contributing to the different results showed in previous studies. Further, the one-year study may also be too brief to yield positive results, especially as it was shown previously that bone markers, microarchitecture, and resistance are shown to be much higher after two years of treatment by Rizzoli *et al.* [200].

A recent study by Wornham *et al*. showed that strontium chloride and strontium ranelate supplementation dose-dependently (0.01, 0.1, and up to 1 mM) reduced mineralisation in the bone-forming neonatal rat osteoblasts cultures in the statistically significant manner [201]. Statistically significant reduction in the ALP activity was seen for the cultures treated by strontium chloride (in all concentration); such a reduction, albeit insignificant, was also seen in the strontium ranelate treated cultures. Other studies supported these findings as high strontium supplementation induced osteomalacia [202], and that higher blood-strontium concentration in renal-failure animals and patients corresponds to osteomalacia [203, 204]. The findings by Wornham *et al.*, contradicted earlier studies that found normal mineralisation was observed in MC3T3 osteoblast cell line culture with 1 mM strontium ranelate supplementation [154]. It is briefly discussed that these differences between the results may be explained by the differences in cells and culture methods.

Most recently, Autefage *et al*. studied the effect of culturing primary human MSC for up to ten days in media conditioned by the ions released from 45S5 bioglass composition (as control) or from bioglass with 10 or 100 mol% strontium substitution (i.e. 0, 0.1, and 1 mM strontium ions in the condition media, respectively) [205]. Whole-genome microarray and Raman spectroscopy, among other methods, were used to study the global cell-material interactions. These analyses showed the increase expression of genes that up-regulate the sterol and steroid biosynthesis and metabolic processes and protein prenylation activity. These genes were shown to later be translated to the increase in membrane cholesterol and lipid raft contents. Apart from these findings, the authors reported that no statistical differences between the control and treatments were found in the regulation of osteoblast-related genes.

With discrepancies found in the literature regarding the effect of strontium supplementation to bone mineralisation in the recent years, further research is of paramount importance. It has been suggested that strontium inhibition to mineralisation may be because of a direct inhibition of the crystal growth or an increased solubility of calcium hydroxyapatite [206, 207]. Hence, it is significant to know for more precisely the effect of strontium supplementation, especially for the benefit of the current patients who are undergoing strontium for bone-related treatment, as well as for future development of therapeutics and bone materials.

2.4. *In Vitro* Model for Bone Mineralisation

Bone mineralisation is a complex, multistep process that has been investigated for more than four decades. *In vitro* investigation of bone mineralisation provides a simpler system to study the already-complex bone mineralisation performed in *in vivo* model. One cell source that has been used frequently in studying bone mineralisation is calvarial osteoblasts. Collagenase isolation protocol of bone cells from rat calvarial was first reported by Peck *et al.* in 1964 [208], and since then studies have been conducted to isolate cell population with improved osteoblastic qualities [209, 210]. Primary osteoblasts have been widely observed *in vitro* to form mineralised nodules resembling true bone [211, 212]: continuous layer of cuboidal cells was seen on the nodule surface; these cells appear to be connected to each other by adherens junctions that resemble gap junctions present in *in vivo* osteocytes [212]. Collagen was seen throughout the nodule to be highly organised, densely packed, orthogonally arranged, and having banding, with initial mineralisation areas marked with needle-like mineral crystals [212].

Large availability, population homogeneity, and phenotype stability are some advantages of using cell lines over primary cells. MC3T3-E1, first established in 1981 from newborn mouse calvaria [213], is an osteogenic cell line with the capacity to differentiate into osteoblasts and deposit minerals *in vitro* [214]. The calcified bone-like tissue was found to resemble that observed in *in vivo* intramembranous calcification, where the minerals are initially localised before calcification is progressed on to the organic matrix. Assessments of this cell line also showed that the cells' time-dependent developmental sequence and expression of osteoblastic characteristics is comparable to that of *in vivo* bone formation [215, 216]. Just as ascorbic acid and β-glycerophosphate (BGP) are essential in *in vitro* culture of primary osteoblasts (for collagen development and to act as phosphate source, respectively [211, 212]), these additives are also required to induce MC3T3-E1 osteoblastic phenotype: Ascorbate is required in collagen deposition and maturation in the extracellular matrix by MC3T3-E1 [215, 217, 218]; BGP further stimulate collagen accumulation and alkaline phosphatase activity in post-mitotic culture, and is required in mineralisation of mature cultures [215, 219].

In this thesis, *in vitro* cell culture approach will be used in the two main studies: 1) to understand the physical and chemical changes of early mineral deposited by osteoblasts, and 2) to understand the effect of strontium supplementation in bone matrix in controlled experiment setup. Primary murine osteoblasts were used for the first study to continue the investigation of previous studies [3, 120]. For the second study, a murine osteoblastic cell line (MC3T3-E1) was used because of its large availability and phenotype stability.

2.5. Hypothesis

The following section will provide hypotheses of the two results chapter presented in this thesis.

2.5.1. Fundamental Understanding of Stages of Bone Mineralisation

It was previously shown that intracellular vesicles containing calcium were observed in *in vitro* osteoblasts, and that the initial *in vitro* mineral in the ECM was hypothesised to be originating from these vesicles that were transported to the ECM [120, 220]. In the first result chapter, we looked into understanding the changes that occurred in the initial *in vitro* mineral as it transformed into mature mineral in the ECM. Following the result of the published study mentioned earlier, it is reasonable to hypothesise that the initial mineral be in spherical morphology as the mineral precursor was initially bound within vesicle membrane. As shown by Habraken's work [133] and others [129, 132], and by the mature mineral morphology by our previous works [120, 220], it can be hypothesised that morphological transformation is one of the changes that may occur as the initial *in vitro* mineral matures.

Changes in the chemistry of the mineral may also occur along with morphological changes. Following up the test-tube experiment by Habraken *et al*. [133], it is reasonable to hypothesise the amorphous nature of the initial mineral, in which will later transform into a more crystalline nature. Changes in the Ca/P and carbonate content may also be seen as the mineral matures. It can be hypothesised that Ca/P will increase as the mineral matures, as shown in [121, 132], and that the carbonate content will decrease as the mineral matures, as shown in the previous *in vitro* studies [134, 135].

2.5.2. Understanding the Effect of Strontium Ion Supplementation to *In Vitro* Bone Cell Culture

Strontium ions have been studied in many different systems (various animal models and cell culture experiments) as agents to promote bone mineralisation. In second result chapter, we supplemented *in vitro* osteoblasts with strontium ions at different concentrations to further tease the effect of strontium ions on the osteoblast matrix during mineralisation. Previous studies showed the increase of collagen synthesis with the supplementation of up to 1 mM strontium ranelate before resulting in the lowering of collagen synthesis at higher strontium supplementation [154]. Similarly, we hypothesise that strontium supplementation will the increase in collagen synthesis in our system.

Twenty five to thirty five percent of supplemented strontium ions have found to be located either on the surface of HA crystals or absorbed in the matrix [183]. We thus hypothesised that the supplementation of strontium ions would affect the organisation of collagen fibrils: higher concentration of strontium ions supplementation would provide higher steric hindrance and would make the collagen fibrils organised more randomly.

Recently published study shed an interesting finding that in strontium ions might increase expression of genes that were later translated to increase in membrane cholesterol and lipid raft contents [205]. Hence, it is reasonable to hypothesise that, using Raman spectroscopy, we would detect a higher lipid contents in as higher concentrations of strontium ions were supplemented to our *in vitro* osteoblast culture.

3. Instrumentation and Sample Preparation

The purpose of this chapter is to describe two technologies used in this thesis: electron microscopy and Raman spectroscopy. After a brief introduction and description of the underlying physics of the instruments, general sample preparation methods and data processing techniques will be described.

3.1. TEM Resolving Power

Spatial resolution is a crucial factor in the world of imaging. This key term is defined as the smallest distance between two points where the two points still appears as two separate points [221]. Resolution power is dependent on the wavelength (λ) of either light or electrons, depending on whether a light or an electron microscope is used. The Rayleigh criterion for light microscopy states that the resolvable distance can be given approximately by:

$$Resolvable\ Distance = \frac{0.61\lambda}{\mu \sin \beta}$$

Equation 3.1 [221]

Where μ is the refractive index of the viewing medium, and β is the lens semiangle of collection; or $\mu \sin \beta$ for is known as numerical aperture.

The wavelength of an electron can be expressed as:

$$\lambda = \frac{h}{[2m_0 eV\left(1 + \frac{eV}{2m_0 c^2}\right)]^{0.5}}$$

Equation 3.2

Where h is Planck's constant, m_0 is the mass of electron, eV is electrons' kinetic energy, and c is the speed of light.

Using Equation 3.1 and Equation 3.2, the resolving power of light microscopes is in the order of 200 nm and 0.2 nm for electron microscopes [222]. This value for electron microscopes is their practical resolution since imperfections on the electromagnetic lenses (spherical and chromatic aberration, as well as astigmatism) place limits on the microscope's theoretical resolution [221].

3.2. Imaging with Transmission Electron Microscopy

In the imaging mode of a transmission electron microscope (TEM), the electron beam is generated by an electron gun, and is directed to the sample using various electromagnetic lenses (Figure 3.1). Upon interacting with the sample, the fast electrons from the source are scattered by elastic and inelastic scattering mechanisms (Figure 3.2). This phenomenon is then exploited to gain a variety of information about the sample.

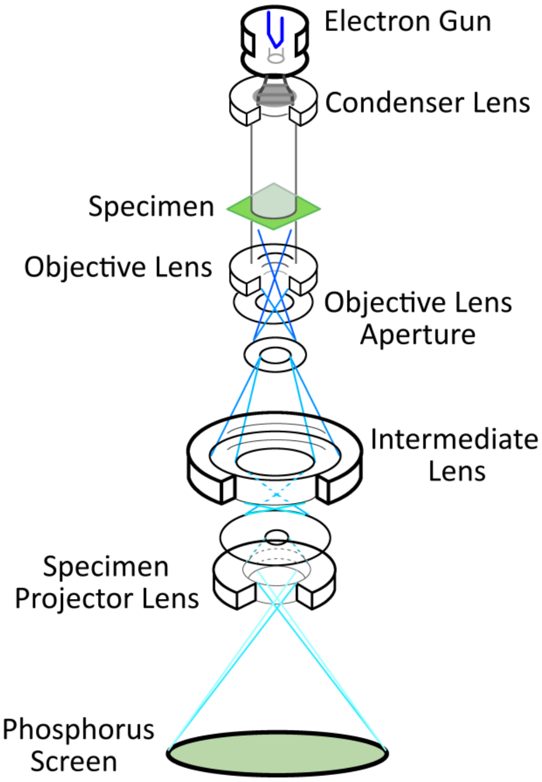

Figure 3.1 Schematic of JEOL FX2000. Figure adapted from [223].

For imaging biological samples, electron transparency is necessary so that fast electrons can pass the specimen without scattering (i.e. direct beam imaging). For this reason, a 100 nm thick sample or less is ideal. Electrons that are scattered (both inelastic and elastic) will form the basis of the spectroscopy analysis in this thesis while another imaging mode, such as electron energy-loss spectroscopy (EELS) and energy-dispersive x-ray spectroscopy (EDX), will be used later in this thesis.

There are two modes of imaging using TEM: bright and dark field (BF and DF, respectively) imaging. BF imaging selects the direct beam to form the image, and the scattered electrons are blocked using objective aperture. By contrast, DF selects the scattered electron rays using an objective aperture (Figure 3.3). In these modes, the contrast in image depends on the scattering angles of fast electrons. This angle depends on a sample's density, thickness, crystal structure, and is proportional to the square of the atomic number of the sample. Sample areas with higher atomic number that scatter to high angles (see Elastic Scattering) will appear dark in BF mode; in DF mode, such areas will appear bright if the scattered rays are chosen by the objective aperture (i.e. a complimentary contrast to the BF image). Such a mechanism of contrast is called the mass-thickness contrast (Figure 3.4; see Elastic Scattering). [221]

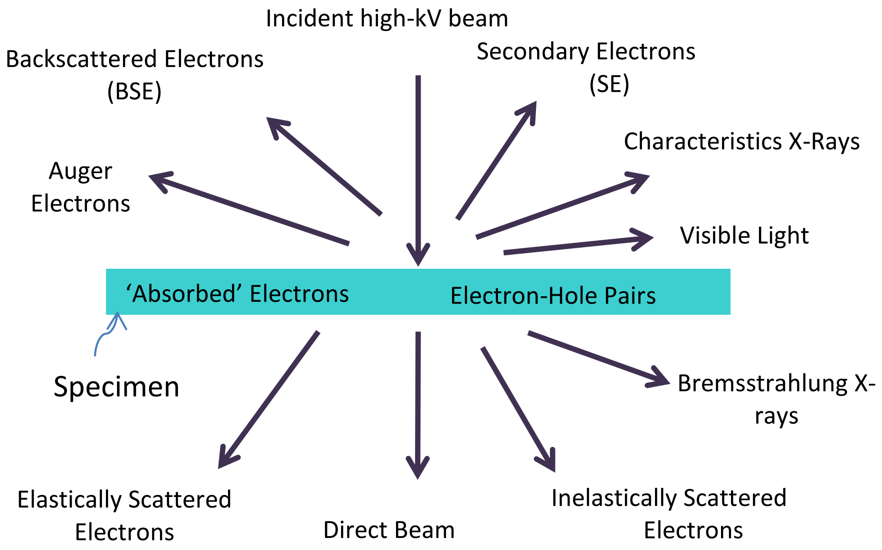

Figure 3.2 Various ways source electrons can interact with the sample. Upon interacting with a sample, electrons are scattered by different processes, and these scattered electrons generate different signals that contain specific information about the sample. Figure adapted from [221].

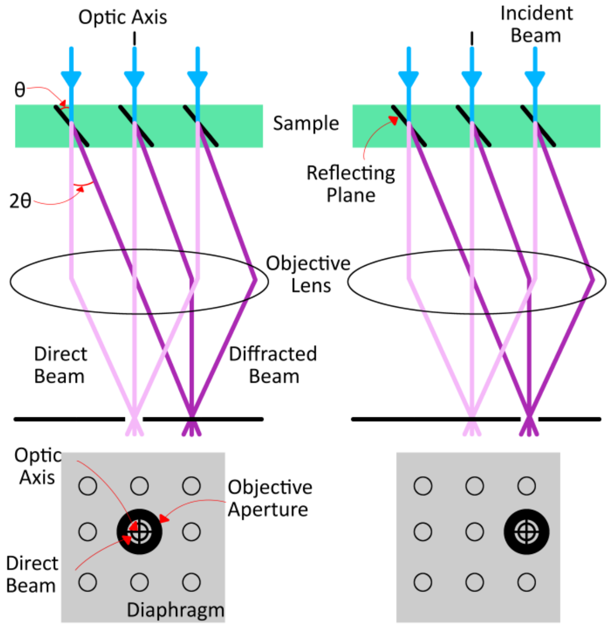

Figure 3.3 Schematic of BF (left) and DF imaging (right). To form the image, BF imaging selects the direct beam and uses objective aperture to block the scattered electrons. DF imaging uses scattered electron rays selected by the objective aperture. Figure adapted from [221].

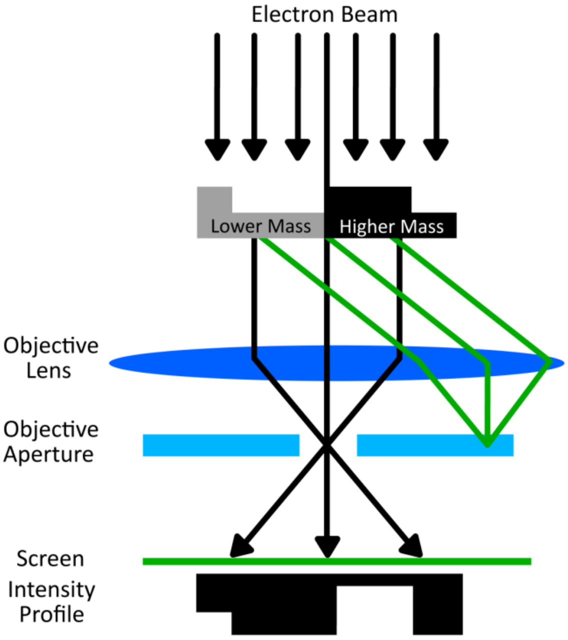

Figure 3.4 Mass-thickness contrast. Areas with thicker or higher atomic number will scatter more electrons off axis and appear darker on BF image (i.e. fewer electrons fall on the screen), but may appear brighter on DF mode given the right selection of diffracted rays. Figure adapted from [221].

3.3. Interaction Cross Section

Interaction cross section (σ) is the probability of a particular electron interacting with the sample. In a two dimensional case, the total cross section (Q_{total}) can be described as the function of number of atoms per unit volume (N) and the total scattering cross-section for an isolated atom (i.e. $\sigma_{\text{total}} = \sigma_{\text{elastic}} + \sigma_{\text{inelastic}}$); the units measurement for the cross-section is barn (or 10^{-24}cm^2). N itself is a function of the Avogadro number (N_A), sample density (ρ), and the atomic weight of the atoms in the sample (A):

$$Q_{total} = N\sigma_{total} = \frac{N_A\rho}{A}\sigma_{total}$$

Equation 3.3 [224]

The total probability of interaction of all atoms in the specimen with a small sample thickness (t) is given by:

$$p = Q_{total}t$$

Equation 3.4 [224]

Knowing Q_{total} also allows the calculation of its inverse, called mean free path (λ_m). Mean free path is the distance covered by an electron through the sample before it is interacting with the atoms in the sample:

$$\lambda_m = \frac{1}{Q_{total}} = \frac{A}{N_A\sigma_{total}\rho}$$

Equation 3.5 [224]

The calculation of mean free path allows for an understanding of how thick the specimen needs to be to avoid multiple scattering events (i.e. plural scattering). By ensuring sample thickness is less than the mean free path, plural scattering is avoided and will result in better imaging and spectroscopy.

3.4. Elastic Scattering

Electrons that are elastically scattered do not have detectable energy loss after they interact with the sample. Being scattered to an angle, these electrons do not form the direct beam. Elastic scattering can be either caused by the electron cloud of the specimen (weak), or by the atomic nuclei (strong; called Rutherford high-angle scattering). The work done in this thesis uses Rutherford scattering. A more detailed explanation of this technique follows.

Using the derivation for Rutherford scattering, the cross-section of the total Rutherford scattering is dependent on atomic number of the sample (Z), initial energy of the incident electrons (E_0), and scattering angle (θ):

$$\sigma_{nucleus} = 1.62 \times 10^{-24}\left(\frac{Z}{E_0}\cot\frac{\theta}{2}\right)^2$$

Equation 3.6 [224]

For a sample with thickness t, the above equation becomes:

$$Q_{nucleus}t = 1.62 \times 10^{-24}\left(\frac{N_A(\rho t)}{A}\right)\left(\frac{Z}{E_0}\cot\frac{\theta}{2}\right)^2$$

Equation 3.7 [224]

With the calculation of scattering cross-section, it is evident that heavier elements (higher Z) will scatter the incident electrons more strongly than lighter elements will. With the thickness of the sample considered, the atomic number of the sample has more influence in the scattering cross-section than the sample thickness does. These properties of Rutherford scattering are the origin of the mass-thickness contrast. [224]

For coherent elastic scattering events, where the incident electron waves have a fixed wavelength, and are in phase with one another, diffraction patterns will arise from the interference of scattered electrons. On this, Bragg’s law explains the condition for constructive interference:

$$n\lambda = 2d \cdot \sin\theta_{Bragg}$$

Equation 3.8 [224]

Where n is an integer, d is the distance between atomic planes, and θ_{Bragg} is the angle between the scattered plane wave and the atomic plane. These scattering events also lead to diffraction contrast in an image when small objective aperture is used to select some scattered electrons at a specific angle.

The interference between several diffracted and transmitted beams can produce a contrast mechanism called phase contrast. At high resolution TEM, the interference produces periodic intensity variations across the sample, showing its atomic columns. [224]

3.5. Inelastic Scattering

When incident electrons interact with a sample, they become scattered and lose energy. This is known as inelastic scattering, and these electrons and their subsequent emissions contain valuable information. For example, when fast electrons interact with the sample and lose energy, their losses can be detected as a spectrum. This creates the electron energy-loss spectroscopy (EELS), a spectroscopic technique explained in more detail below. The subsequent emissions of inelastic scattering events can be informative when X-rays emitted from the slowing down of the fast electrons are detected using the Energy Dispersive X-ray spectroscopy (EDX). Other emissions such as Auger electrons, photos, and bremsstrahlung can also be useful for other types of spectroscopic techniques. [224]

3.6. Scanning Transmission Electron Microscopy

Another mode of TEM is scanning TEM (STEM). In this mode, instead of using parallel illumination of the sample, the source electrons are converged using double deflection scan coils. The converged electrons form a probe that then is rastered across the sample (Figure 3.5). The image is formed by detecting the electrons that are scattered by the samples to different angles (Figure 3.6). BF is detected using fast electrons scattered to a semiangle less than 10 mrad, annular DF detects those scattered between 10-50 mrad, and high angular annular dark field (HAADF) detects those that are greater than 50 mrad. The image contrast is gained through the mass-thickness contrast. Since the image is formed without using a post-specimen lens, objective lens aberrations do not affect the resolution.

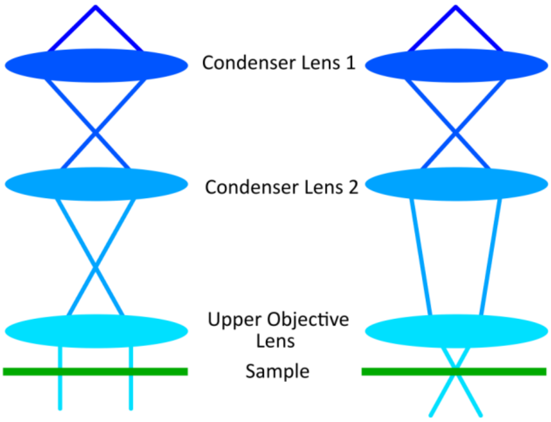

Figure 3.5 Parallel illumination in TEM mode (left) and condensed rays in STEM mode (right). Figure adapted from [221].

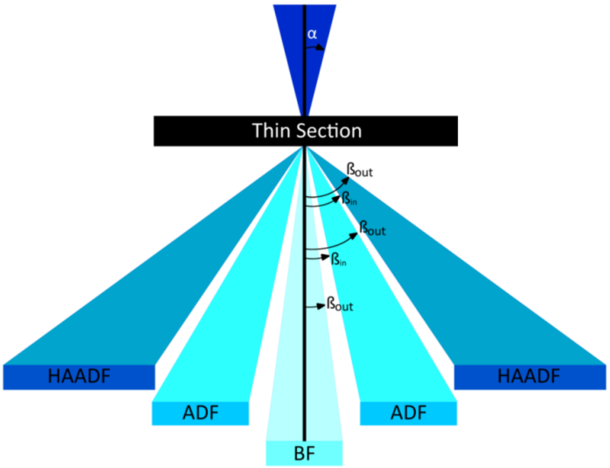

Figure 3.6 Geometry of HAADF, ADF, and BF detectors with their collection angles (ß). Figure is adapted from [221].

3.7. Electron Source

To generate images and perform other TEM characterisations, fast electrons from a source must be generated and bombarded to samples in vacuum chamber. This is done to avoid the fast electrons from interacting or being ionised and absorbed by air. An electron gun is used as the electron source, and its electrons are accelerated to high energies using an electrostatic field. There are two kinds of electron gun [221]:

3.7.1. Thermionic Emission Gun (TEG) (e.g. JEOL FX2000)

As high temperatures can cause electrons to break free from a material, the electron guns in this category are heated until their electrons overcome the barrier (called the work function) to form the electron beam. As a result, the material chosen for a TEG needs to have either a low work function or a high melting point (to minimise melting, vaporisation, or oxidation during the process). Lanthanum hexaboride or tungsten is commonly chosen as TEG materials for their low work function and high melting point, respectively.

3.7.2. Field Emission Gun (FEG) (e.g. JEM 2100F and TITAN)

One of the two kinds of FEGs is called a cold field emission (CFE) gun. CFEs operate at room temperature and rely on the presence of strong electric fields to break the electrons free from a metal source. The other kind of FEGs are thermally-assisted field emission (Schottky), which use thermal energy and an electric field to provide the source electrons with enough energy to become liberated.

The different types of gun source affect the quality of the image formed. For example, the brightness of the image is inversely proportional to the square of the semiangle that the electrons diverge to from the source. This semiangle, in turn, is proportional to the size of the electron gun tip. Hence, the bigger the tip of an electron gun (e.g. such like those of the TEGs), the lower the brightness of the images produced. A FEG, which has finer tip, produces brighter images. This size of the gun tip also contributes to the spatial coherency (i.e. whether the electrons come out from the same point at the source). A more coherent beam produces a sharper diffraction pattern, and the spatial resolution of the image is vastly improved. Taking in mind the aforementioned factors, it would be reasonable to assume that FEGs produce better images than TEGs. However, in terms of overall stability of emission currents, TEGs are considered more stable than FEGs, and because of this feature considerably higher vacuum and electrical feedback circuits are required to maintain their stability [221].

3.8. Electron Lenses and their Imperfections

The electrons generated by a source are focused by electromagnetic lenses. These lenses are made from a magnetic material as the casing or 'polepiece' with a hole called a 'bore'. The polepiece comprises double concentric cylinders, similar to a tall-doughnut shape, and often made of soft iron. Inside the metal 'doughnut' casing are loops of copper wire, which produce a magnetic field when an electrical current is given. Electrons that are travelling close to the wall of the lenses are deflected towards the optical axis, which focuses the electron rays. [221]

There are numerous issues with the use of electron microscope lenses (Figure 3.7):

3.8.1. Spherical Aberration

Spherical aberration is caused by over focusing of off-axis electrons and produces a disc (known as the 'disc of least confusion') as an image of a point object (Figure 3.7). This lens defect is the ultimate source of the inability to resolve the image. In TEM mode, it is the objective lens's spherical aberration that limits the image resolution; in STEM mode, it is the condenser lens that enlarges the probe. [221]

3.8.2. Chromatic Aberration

Not all of the fast electrons have the same energy when they interact with the sample. These electrons are also focused at different planes. Fast electrons that interact with the sample have different energies, particularly from >100 nm thick samples. Similar to spherical aberration, chromatic aberration results in the formation of a disc of least confusion. [221]

3.8.3. Astigmatism

Astigmatism is the result of the imperfections of magnetic field generated by the electron lenses. This is an inherent problem of lens manufacturing since there is a limit on how homogenous the microstructure of soft iron can be manufactured. Other possible causes of astigmatism are the imperfection of aperture positioning when placed in the pathway of the lens, and aperture contamination interacting and deflecting the electrons. [221]

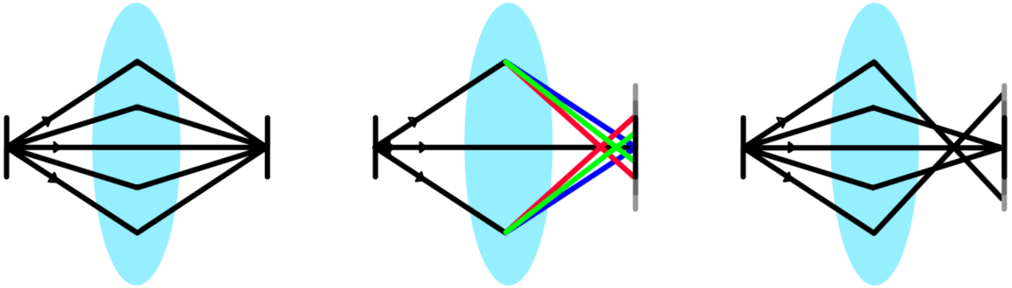

Figure 3.7 A perfect lens (left) is able to focus the beam into one single point, resulting in a focused image. With aberrations such as chromatic aberration (middle) and spherical aberration (right), the beam is not focused into a single point, which results in a disc of least confusion. Figure adapted from [225].

3.9. Beam Damage

There are two forms of damage that a TEM beam can generate: Knock-on and Radiolysis damage [221]. These forms of damage must be taken into consideration when imaging biological samples, which are usually prone to damaging.

Knock-on damage occurs when fast electrons transfer kinetic energy to the sample, causing atoms from the sample's crystal lattice to displace or cause point defects [226]. Knock-on damage mainly affects metals; however, it also affects samples containing hydrogen atoms, and worsens when samples containing low or medium atomic number elements are exposed to higher energy electrons (kV). As a result, the total electron dose (C/cm^2 or electrons/cm^2) should be minimised if higher electron energies are used during imaging and analysis [227]. Alternatively, the use of a lower operating voltage can reduce knock-on damage.

Radiolysis or ionisation damage is caused by inelastic scattering that causes chemical bonds to break and affects organic materials and polymers [226]. When chemical bonds break, molecules change in shape and shifts in position; such a change may cause the loss of crystallinity in a crystalline sample, a breakage of chemical bonds, the creation of non-native chemical bonds, and mass loss (i.e. thinning of the sample that may eventually lead to the creation of a physical hole in the sample). The use of high accelerating voltage (e.g. 300 keV) decreases the probability of electrons interacting and transferring energy to the sample, which reduces radiolysis damage. The trade-off in using high accelerating voltage is that the image contrast is reduced because of the lowered likelihood of elastic scattering events [227].

Since the tissue culture samples analysed in this thesis were not thermally conductive, the problem of specimen heating was encountered. Thinning the samples is one way to reduce specimen heating. The highest available accelerating voltage can also be used to reduce specimen heating, although at the expense of reduced contrast [221]. The experiments conducted in this thesis were conducted using a low acceleration voltage (80 kV) to maximise the contrast. In order to minimise beam damage, the samples were exposed minimally to the beam, and were blanked while experiments were being set up.

3.10. Energy Dispersive X-Ray Spectroscopy

Energy Dispersive X-Ray Spectroscopy (EDX) is an analytical technique to analyse the elemental content of a sample. This technique detects X-ray characteristics unique to each element. As the electrons from the microscope's source hit the specimen and knock out the electron in the inner electron shell, an X-ray is generated as the outer electron shell of the element replaces the knocked-out electrons of the inner shell (Figure 3.8). Depending on where the knocked out electrons originate, X-rays of different energies are produced. For example, K_α is the X-rays emitted by electrons in the L-shell replacing electrons in the K-shell, while K_β corresponds to X-rays emitted by M-shell electrons that replace electrons in K-shell [221]. In short, the EDX detects these different X-rays and separates them into a spectrum based on the rays' energies (plotting intensity or counts versus X-ray energy) [221].

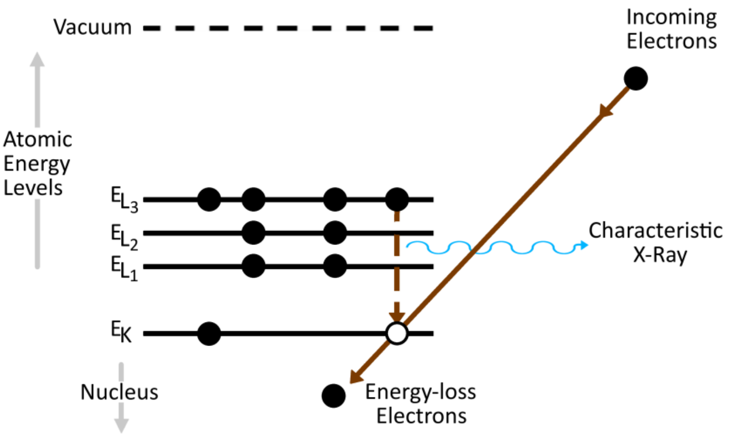

Figure 3.8 Schematic of incident electrons knocking out the electron in the K-shell, which is replaced by an electron from L-shell. The characteristic X-ray is the difference in energy between the knocked-out electron shell with the one replacing it (i.e. $E_{L3} - E_K$). Figure adapted from [221].

Two important parameters in EDX data collection are the pulse processing time constant (τ) and dead time [221]. τ is the time allowed for the processor to evaluate the magnitude of the pulse. The longer the τ, the better the system is able to assign energy to the incoming pulse (better resolution), with the expense of a high number of counts being processed in a given time (counts per second) [228]. Dead time is the time necessary for the detector to be switched off while the processor is analysing the pulse. Dead time is closely linked to τ; dead time will increase as more X-rays try to enter the detector [221]. Dead time can be defined as:

$$Dead\ time\ in\ \% = \frac{(Clock\ time - Live\ time)}{Live\ time} \times 100\%$$

Equation 3.9

Where Live time is the time that the detector must be live to receive the X-ray, and Clock time is the total time (live and dead times combined) that the EDX signal acquisition procedure is run. A large dead time results from in a large number of X-rays such that the collection becomes inefficient. With optimised parameters, elements present in a larger amounts, i.e. more than 10 wt%, will generate major peaks. Although the detection limit of EDX varies depending on the elements, elements present 1-10 wt% will generate a high enough peak for detection [229].

In the work featured in this thesis, EDX will be used to calculate the ratio of elements Calcium and Phosphorus (Ca/P). For this, a standard with known Ca/P (measured with XRD) was used to calculate the constant that relates the peak intensity ratio of both elements to the concentration ratio, according to the Cliff-Lorimer equation:

$$\frac{True\ Concentration_{Ca}}{True\ Concentration_{P}} = Constant\frac{EDX\ Intensity_{Ca}}{EDX\ Intensity_{P}}$$

Equation 3.10

Once the constant is calculated using the known Ca/P standard, the unknown Ca/P of a sample can be calculated using the Constant and the peak intensity of the standard's Ca and P.

3.11. Electron Energy-Loss Spectroscopy

Electron energy-loss spectroscopy (EELS) is the analysis of energy distribution of TEM-source electrons that lose some of their energies after interacting with specimen electrons. This energy loss is caused by source electrons' inelastic interaction with either the inner or the outer shell of the specimen's electrons (Figure 3.9). [224, 230]

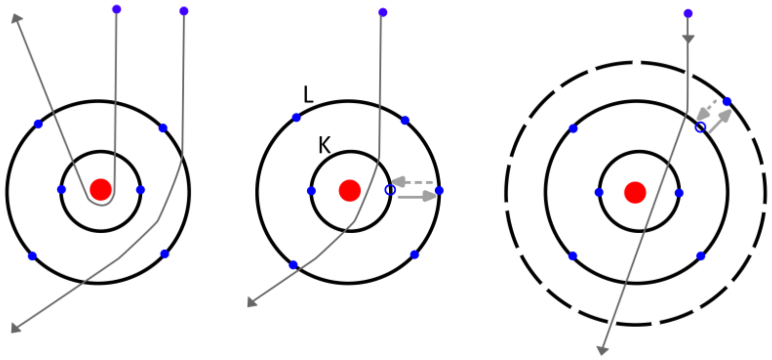

Figure 3.9 A schematic of a single carbon particle with elastic scattering occurring when fast electrons pass through without any loss of its energy (left). Inelastic scattering of fast electron can occur with the inner (middle) or outer (right) shell electrons. The fast electrons' energy loss will be graphed into an electron energy-loss spectrum. Figure adapted from [230].

For this technique, a standard TEM or scanning TEM (STEM) is fitted with a magnetic prism spectrometer and several electromagnetic lenses. Installed beneath the camera system, this spectrometer resolves the array of energy losses that will then be focused by the lenses and projected to a scintillation counter (i.e. YAG scintillator). With a scintillation counter connected to a photodiode (i.e. a charge-coupled device or CCD) at the other end, the signal is converted to a voltage, which is then digitised to an electron energy-loss spectrum (Figure 3.10). This spectrum shows the scattered intensity as a function of the decrease in kinetic energy of the electrons.

The energy-loss spectrum can be divided into two parts (Figure 3.11): low-loss (between 0-50 eV) and core-loss (higher than 50 eV) regions. In low-loss regions, the signal at zero energy loss (i.e. zero-loss peak) represents the electrons transmitted without measurable energy loss (elastic scattering), those whose energy lost is less than the experimental energy resolution (those electrons having excited phonon), and those not scattered by the specimen. Plasmon peaks also exist in the low-loss region. These peaks are composed of peaks created by fast electrons' inelastic scattering from outer-shell electrons (i.e. valence electrons). Zero loss peak and plasmon peaks enable the measurement of specimen thickness that can be used to correct the effects of plural inelastic scattering (multiple scattering of an electron when the specimen thickness is greater than the electron's mean free path) in quantitative EELS analysis of the core-loss region. [230]

The core-loss region of the EELS spectrum represents the intensity of TEM source electrons that inelastically interact with inner-shell specimen electrons. With the inner-shell electron energies dependent on the atomic number of the respective atoms, the ionisation edges present in the EELS spectra indicate the elements that exist in the specimen (i.e. elemental analysis). In this case, the source electrons have sufficient energy (the critical ionisation energy or ionisation threshold) to make the inner-shell electrons escape the atoms' nuclear forces, causing the atoms to be ionised. The fast electrons' energy that is lost in this process is measurable using EELS. What follows is the emission of the characteristic X-ray (detectable by EDX) or an Auger electron (detectable by Auger Electron Spectroscopy) to bring the excited atoms back to their ground state (Figure 3.12) [230]

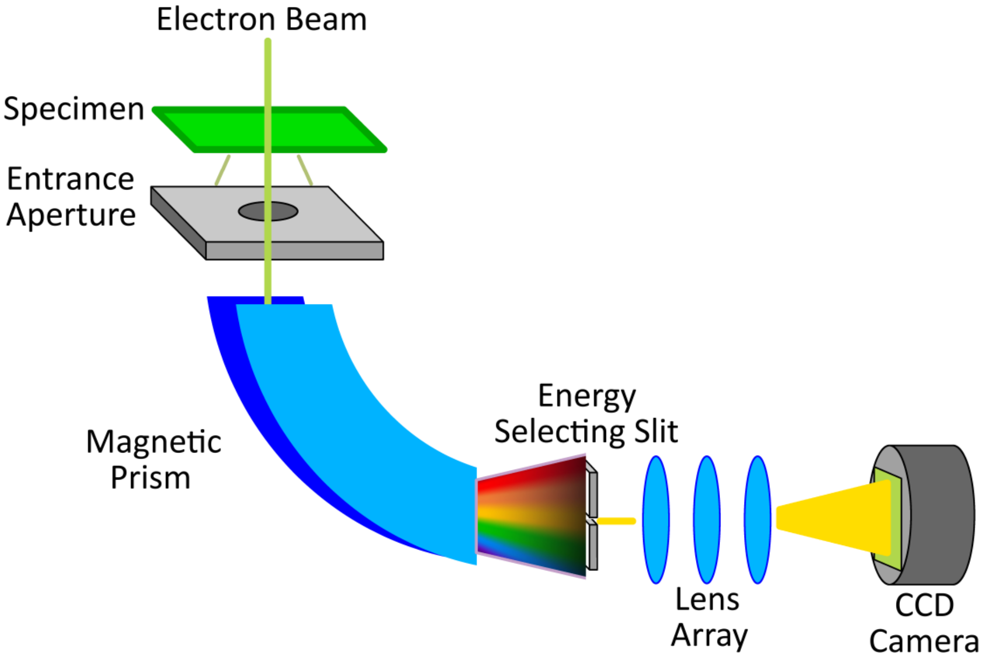

Figure 3.10 Schematic of EELS TEM setup. Figure is adapted from [231].

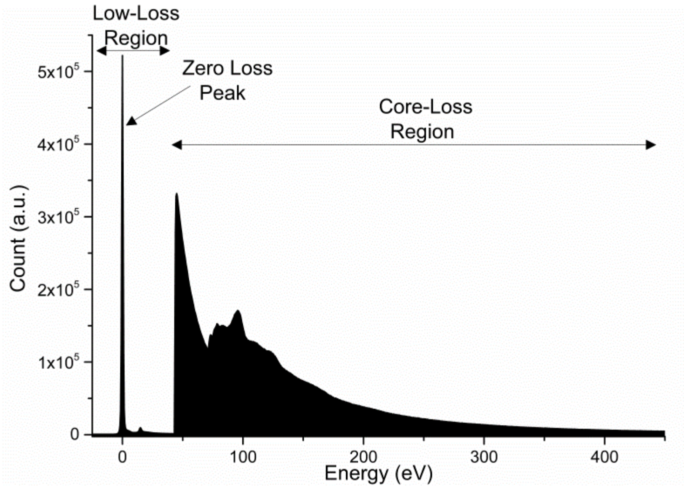

Figure 3.11 A typical energy-loss spectrum. The low-loss region consists of the zero loss peak, where the electrons detected are elastically scattered and did not lose energy. Core-loss region (depicted 100,000 times) contains electrons that are inelastically scattered upon interacting with the specimen. Figure adapted from [232].

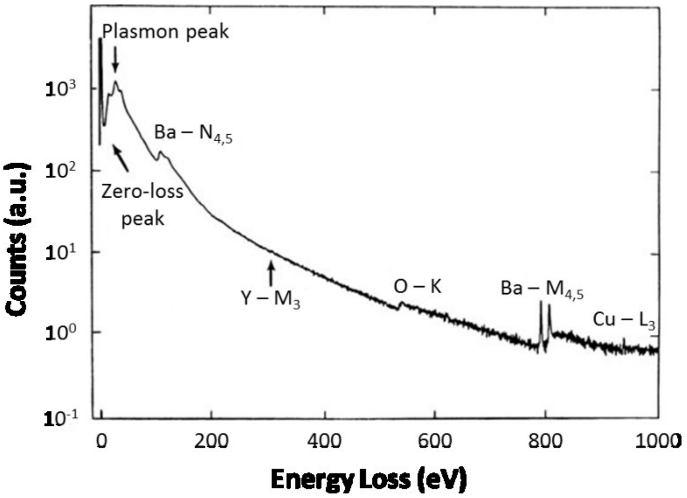

Figure 3.12 Schematic of electron-loss spectrum from zero-loss peak and plasmon peak in the low-loss region, as well as the core-loss region above 50 eV. The core edges are labelled according to their corresponding ionised shells: K – 1s, L – 2s/2p, M – 3s/3p/3d, N – 4s/4p/4d/4f and 0. Figure adapted from [230].

The core-loss region of the EELS spectrum not only gives elemental information, but also allows for the elemental environment or chemical bond analysis. The ability to see a difference in energy loss as a result of difference in chemical bonding is attributable to the excited specimen electrons, which do not have an equal probability of filling up empty energy levels (termed as density of unfilled states or DOS). DOS is very sensitive to bonding or valency changes (i.e. if an atom changes its coordination with other atoms). Finally, as energy loss intensity is higher at high DOS regions, the fine structure at the ionisation edge can determine the bonding environment of the observed atoms.

In quantifying EEL spectra, the measured intensity can be converted to elemental ratios (i.e. Ca/P) by incorporating the contribution of the cross sections (i.e. the probability of an incident electron being scattered by a given atom), which is a function of the collection angle, range of energy loss (or dispersion), and incident electron energy [230]. Quantitative elemental and bonding analysis of EELS spectrum can be done by measuring the area under the appropriate ionisation edge, while taking into account the background intensity. The background intensity (I) of the high-loss region is subtracted using the power law model, according to the equation:

$$I = AE^{-r}$$

Equation 3.11

Where E is the energy loss, A and r are constants of curve fitting.

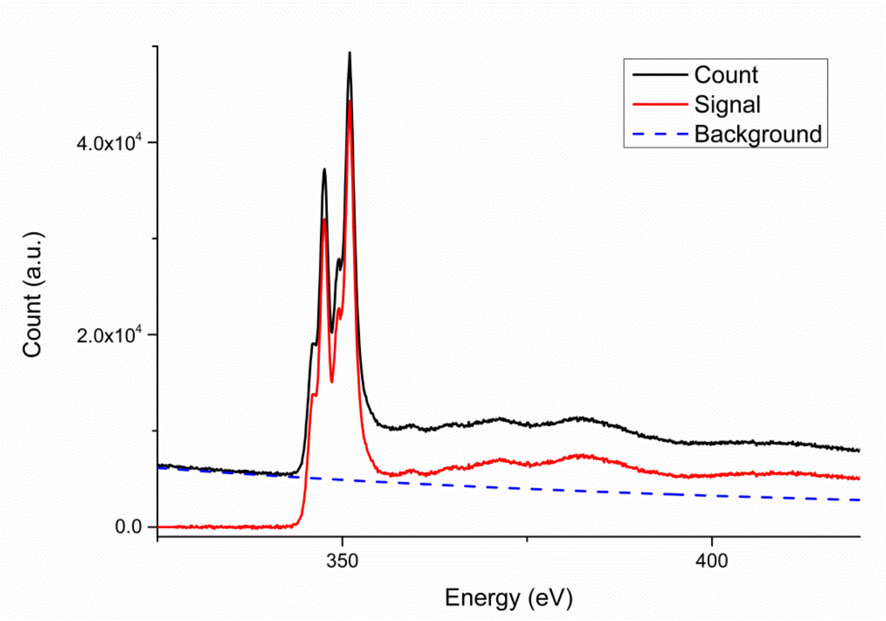

Figure 3.13 Decreasing power-law background subtraction (blue dashed line) is done on original EEL spectrum (black line) resulting in a background subtracted signal (red line). A good background leaves a residual that is close to zero and with little fluctuation.

3.12. EELS Processing

EELS spectrum images (or EELS mapping) contains 3-dimentional data: *x*- and *y*-coordinates (2-dimentional space), as well as the intensity at the different energy-loss (eV). With many spectrum images taken to account for reproducibility, high number of data has to be processed, and it becomes impractical to examine each spectrum in each pixel manually. The two methods used in this thesis to treat large number of spectral analysis will be briefly reviewed: principle component analysis (PCA) fitting and multiple linear least squares (MLLS).

3.12.1. Principle Component Analysis

Also known as multivariate statistical analysis, the PCA method does not require prior knowledge of the components present in the sample. This analysis is used to mainly smooth EELS spectra; in other words, PCA is able to isolate the most important contribution from the noises by calculating the minimum number of 'principal components' necessary to construct a new dataset of all significant information. With PCA, the spectrum is assumed to be composed of linear sum of a finite amount of specific characteristics. The spectrum can be decomposed into [233]:

$$I = PC_1c_1 + PC_2c_2 + \ldots + PC_nc_n$$

Equation 3.12

Where $\mathrm{PC_n}$ is the $\mathrm{n^{th}}$principal component, and $\mathrm{c_n}$ measures the contribution of $\mathrm{PC_n}$ to the pre-processed or original spectrum.

To calculate the principle components, the 3D dataset is first arranged into a 2D matrix, $\mathrm{D_{N\times P}}$, where P is the spectra in each pixel (i.e. (x,y)), and N are the energy points. A covariance matrix $\mathrm{Z_{N\times N}}$ is then calculated by multiplying D with its transpose [234]. The eigenvalues of Z are the principal components. Small eigenvalues correspond to low-amplitude statistical variations in the dataset and experimental noise. The removal of these components will be plotted back as noise-filtered representation of the original data [233]. In this thesis, PCA was used to smooth the spectrum corresponding to each element: pre-edge background-subtraction was done for a particular element, before the PCA was used at 5-10 eV prior to the first edge for the element, and continued for around 30-40 eV.

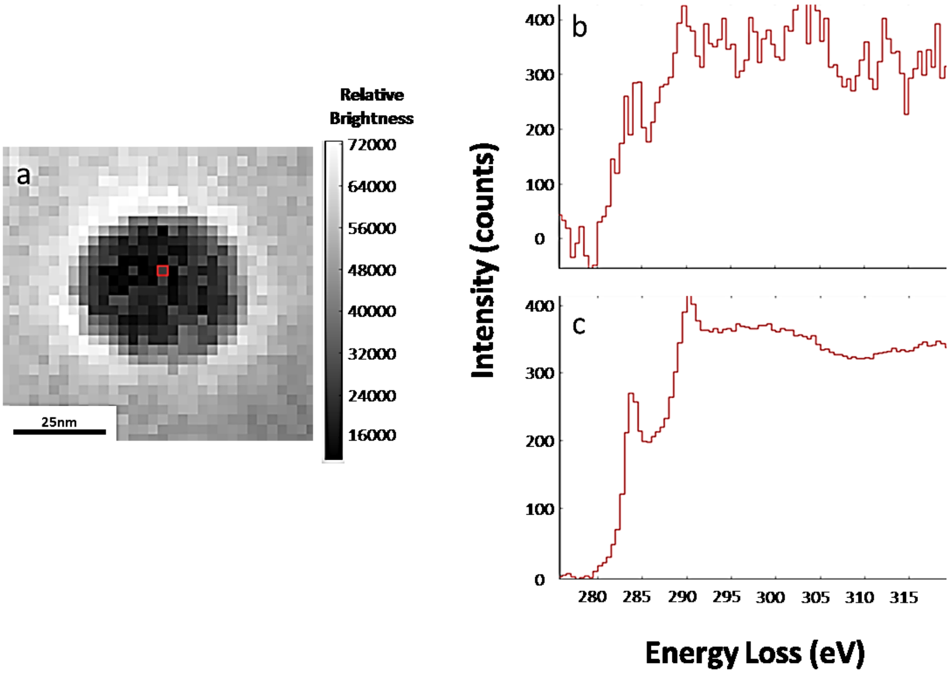

Figure 3.14 An example of the use of PCA in smoothing a spectrum. A pixel of a particle (a; in red square) has a carbon-edge spectrum. Graph b shows the pre-PCA noisy spectrum, while the post-PCA spectrum (c) shows much cleaner spectra (three-principal component treatment was used).

3.12.2. Multiple Linear Least Squares

Multiple linear least square is also known as singular value decomposition. Unlike PCA, MLLS fitting requires prior knowledge of all the components in the sample and spectra. Here, the experimental spectrum is decomposed to linear combination of its chemical components:

$$I = I_1\mathrm{t}_1 + I_2\mathrm{t}_2 + \ldots + I_n\mathrm{t}_n$$

Equation 3.13

Where I is the intensity of the experimental spectrum, $\mathrm{t_n}$ is the mass thickness, and $\mathrm{I_n}$ is the spectral intensity of component n. The mass thickness $\mathrm{t_n}$ is the fit coefficient determined by solving the linear Equation 3.13 . In physical terms, the higher the fit coefficient of a component, the higher concentration of that particular component present in the sample. As complete knowledge of the sample is often not possible, internal reference spectra can be created. For this, regions containing different components are identified by manual inspection. The spectra at these regions then become the internal references during the fitting [235].

3.13. Biological Sample Preparation for TEM

Most biological samples originate from hydrous environment, which requires them to be treated for the vacuum condition in the TEM. Treating a sample for TEM needs to ensure the sample keeps its original state, such as its shape and chemistry. Achieving complete sample preservation is a complex process compared to preserving just one aspect of the sample. As a consequence, studies have often used complimentary methods of sample preparation to gain knowledge about the original sample state. This review focuses on techniques used in this thesis.

One of the most common treatments of a biological sample is the chemical fixation method (Figure 3.15). Contrary to what the name may suggest, this preparation method does not entirely conserve the chemical nature of the sample. The name simply refers to the sample's fixation using a chemical agent. A cross-linking agent (e.g. formaldehyde or glutaraldehyde) is used to cross-link the amino acid of the cellular membranes, resulting in the conservation of cellular structure. This route of sample preparation is a good means by which to obtain TEM micrographs. To further obtain contrast at the TEM imaging stage, the cell organelles are stained with a heavy metal such as osmium tetroxide, uranyl acetate, or lead citrate. These post-fixation stains can also act as secondary fixative incorporated into the unsaturated carbon bonds in lipids. Following fixation, the sample becomes dehydrated, and the water content is slowly replaced by alcohol. Graded concentrations of ethanol are used to prevent the samples from collapsing as water slowly goes out of the cell (via osmosis) and the ethanol slowly replaces the water. The now-anhydrous cell sample is slowly infiltrated with anhydrous liquid polymer, before curing it (e.g. using UV or heat). As

TEM requires ultra-thin samples (~70-100 nm), the cured polymer (resin) preserves the cellular shape and location as it is mechanically sliced using a diamond knife using ultramicrotome, or milled using a focused ion beam (FIB) [236].

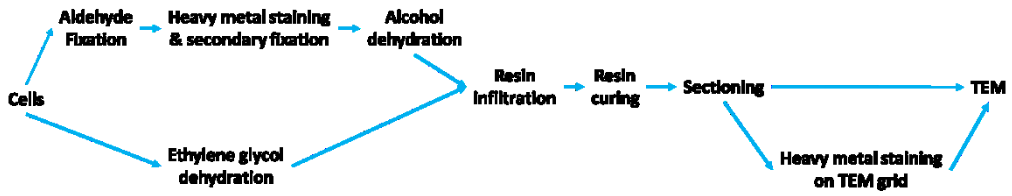

Figure 3.15 Flowchart of various TEM sample preparation routes. Chemical fixation uses aldehyde fixation before staining and resin work. Anhydrous fixation uses ethylene glycol dehydration. Heavy metal staining is performed on sectioned samples on TEM grid.

The chemical fixation method is a relatively simple treatment for biological samples for TEM. However, one of its major drawbacks is that it does not completely preserve the chemical composition of the sample. This is a key challenge in understanding how bone mineral matures as there may be unseen chemical changes occurring [66, 121, 129, 132, 237] (reviewed in Literature Review). Because of this drawback, a second way of preparing the sample is to treat it with anhydrous ethylene glycol as the dehydration agent right from its native state (skipping the aldehyde and heavy metal fixations and alcohol dehydration) before proceeding with the polymer embedding (Figure 3.15). Although this anhydrous method [120, 238, 239] conserves the chemical components and crystalline structure of the sample (i.e. bone mineral), the cellular and other organic structure are not fully preserved (since the fixation step is avoided). Even if a slight preservation of the organic component is achieved, the TEM imaging contrast is not attained since heavy metal staining is not performed before resin curing. To circumvent this challenge, post-staining with uranyl acetate and lead citrate can be performed on sectioned, cured samples on the TEM grid.

3.14. Overview on Raman Spectroscopy

Raman phenomenon was discovered by Sir Chandrasekhra Raman in 1928 and has been extensively used to characterise a wide variety of biological samples. A laser is used to interact with the sample, which causes the sample's molecules to be excited to higher energy states. Upon relaxation, the excited molecules emit photons. However, instead of returning to their original state, they return to states more energetic than initial. As a result, the emitted photons' energy is less than the total energy given by the laser (Figure 3.16). The difference or shift in the vibrations is the effect observed providing a sample's characterisation. [240]

Scattering events are initiated by a laser's electric field, which forces the electrons in the sample to oscillate about their equilibrium position. Compared to the various excitation events that happen when a laser interacts with a sample, a meaningful Raman signal is low. Most of the laser's power is absorbed into the sample and only a low percentage is scattered. From the scattering events, elastic scattering events (Rayleigh scattering; photons stays at the same frequency, but change in direction) represent the majority. The small remaining fraction of the scattering events contributes to the Raman characterisation: the inelastic scattering or Stokes and Anti-Stokes scatterings (photon changes both frequency and direction).

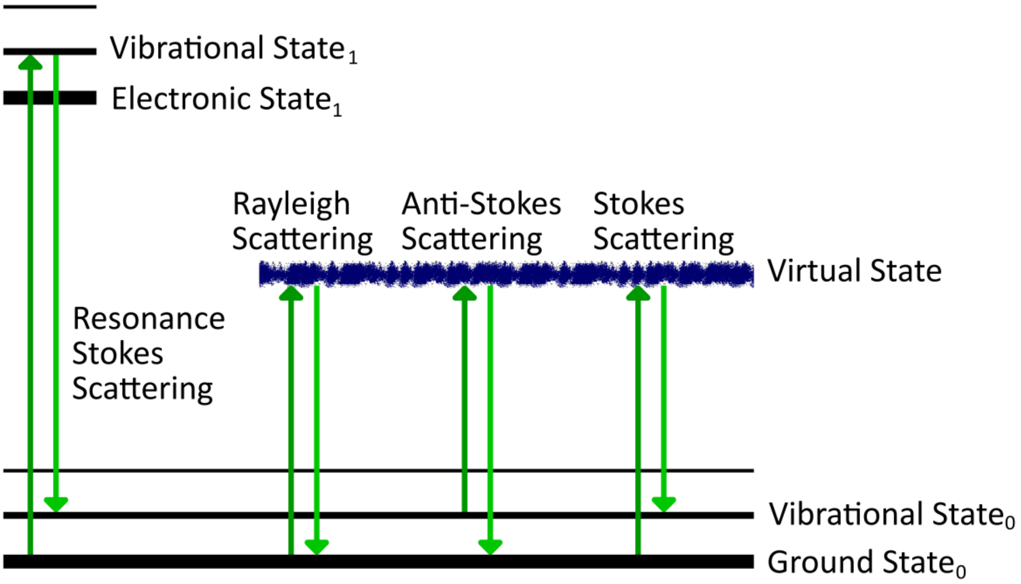

Figure 3.16 A diagram showing the energy state of sample undergoing various scattering events. The arrows pointing upwards represent the shift in energy levels upon excitation, followed by relaxation and emission of secondary photon (downward pointing arrows).

As sample molecules are interacting with the laser in scattering events, the electron distribution of their chemical bonds changes and the molecules go to an unstable virtual state. In inelastic scattering events, the photons emitted when molecules relax have either higher or lower energy than the amount of energy given to the molecules. The resultant states of the molecules are lower or higher than their initial energy levels (namely Stokes and Anti-Stokes, respectively). The work done in this thesis is based on Stokes scattering since the excitation energy used is much smaller than the energy of the molecule's first electronic state. As a result of this change, the sample molecules will not change to higher electronic states following their interaction with the laser.

3.14.1. Raman Acquisition for Biological Samples

One of the most exploited features of Raman spectroscopy for biological samples is its ability to gain meaningful signal from hydrated samples. This is because water molecules scatter Raman signals weakly. In this thesis, *in vitro* cellular mineralisation is investigated, and Raman spectroscopy is used to characterise fixed and hydrated *in vitro* soft tissue. Raman spectroscopy is also able to detect crystallinity and substitutions in minerals [241, 242].

In essence, the hardware for Raman characterisation will include a laser source to excite the sample (a 785 nm laser is used in this study), specimen stage (a motorised stage is used in this study), some lenses that act as filters to reject elastic scattering events, dispersion elements, and a detector (Figure 3.17). With such hardware and a proper calibration, it is possible to take spontaneous and dispersive Raman spectroscopy that is technically simple, yet robust and cost-effective.

Raman acquisitions result in spectra of scattered intensity (arbitrary units) against the energy difference between incident and scattered photos (i.e. 'Raman Shift'; cm^{-1}). The Raman spectrum and its intensity will depend on the range of the shift to be detected, the acquisition energy and power of the laser, and the number of accumulation repeats per spectrum and each of their acquisition times.

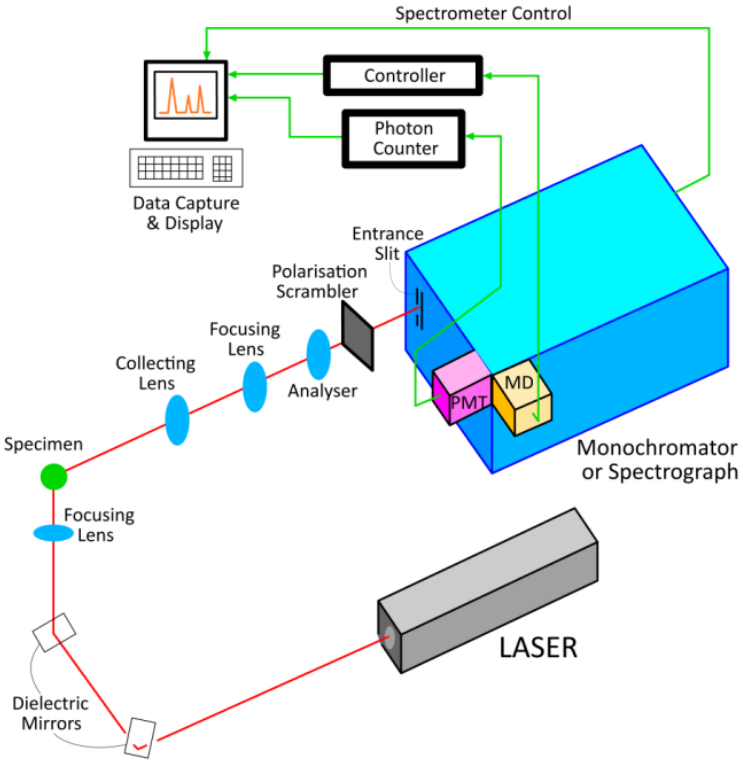

Figure 3.17 Raman Spectrometer hardware schematics. Figure adapted from [240].

4. Nanoscale Analysis of *In Vitro* Bone Mineral Alludes Sequential Crystal Maturation Processes

4.1. Introduction

Investigations into how bone starts to mineralise began more than 25 years ago, in the early 1990s. Bone has been studied at multiple levels of hierarchy from the whole bone level to the level of the collagen fibrils, however little is known about how the chemistry and morphology of the mineral changes in the extracellular matrix (ECM) in the earliest stage of mineral maturation. Bone is a nano-composite materials and it is generally accepted that that poorly crystalline carbonated apatite-like crystals associated with the collagen fibrils [83]. The mechanism of mineralisation involves precipitation and crystal growth of amorphous calcium phosphate (ACP) precursors within the collagen fibrils [129, 132]. Several questions remain unanswered about the mineralisation process including: how is the collagen contributing to the mineralisation process, where does the mineral precursor originate from, is the chemistry and crystallinity of the early mineral precursor the same as its mature form, and how does the morphology and chemistry of the mineral change during mineral growth on the collagen. In particular, the spatial relationship between the precursor ACP and the mature apatite crystals is poorly understood.

There has been much debate in the literature about whether calcium phosphate (CaP) precursor phases are delivered to the collagen and whether these precursor phases wholly account for mineralisation of the collagen fibrils [121]. Numerous mechanisms have been proposed to explain early bone mineral formation [121, 132] including: (1) a cell-independent (protein-assisted) process where charged non-collagenous proteins associate with the gap zones in collagen and mediate the mineral nucleation from ions in solution [84, 243]; (2) a cell-controlled mechanism where mineral seeds are formed within intracellular vesicles that are released from the plasma membrane and subsequently rupture and disperse their contents on the extracellular matrix (ECM) [120, 121]; and (3) an acellular route in which amorphous

CaP mineral precursors are produced and deposited in collagen fibrils where they transform into more crystalline apatite platelets [84, 129, 133]. It has yet to be determined whether these mineralisation processes act cooperatively or in parallel.

An outstanding question in the literature is how the transient mineral precursors mature and grow into carbonated crystalline apatite on the collagen *in vivo,* and the processes by which their morphology, chemistry, structure, and coordination environment evolve over time and as they grow into mature bone mineral. Mature bone is composed of poorly crystalline carbonated apatite that contains up to 6 wt% of carbonate in the apatite crystals [64, 244], and ACP is generally believed to be the transient precursor phase of bone. Different formats and chemistries of CaP have been detected in mineralising bone using different models and at different spatial locations relative to collagen and cells. For example, the growth zones of forming zebrafish fin bones contain spherical ACP particles that are 10-20 nm in diameter with a low Ca to P ratio (Ca/P) [129, 132, 245]. These studies also detected submicron-sized globules around the collagen fibrils and suggested that these were composed of the ACP subparticles, which eventually become part of mature bone. However, cryo-scanning electron microscope (SEM) observations in these experiments did not have the spatial resolution to confirm this hypothesis. In mammalian systems, ACP granular deposits have also been detected in the mitochondria of mineralising rat osteoblast cells [121]. Micrometre-sized globular-like structures comprised of apatite crystallites have been found in mineralised nodules formed from osteoblast cells [120].

Various *in situ, in vitro* and *in vivo* models have been used to understand how bone mineral precipitates and grows into mature CaP crystals. *In vivo* fish models have illustrated the presence of spherically-shaped dense granule CaP materials in the early mineralisation regions, and submicron-sized globules comprised of apatite crystals associating with the collagen and needle-textured spherical CaP in the more mature regions [83, 129, 132]. However, these studies did not provide direct evidence that the nanospherical particles were amorphous or the relationship between the granules of CaP and the submicron-sized globules [129, 132]. *In vitro* models have focused on where the initial CaP (*i.e.* the spherically-shaped CaP) originates. These studies observed the occurrence of intracellular vesicles containing

CaP and hypothesised that CaP granules are found within osteoblast mitochondria and intracellular vesicles, which then transport material to the ECM [120, 121]. Using acellular models, the mineralisation of isolated and reconstructed collagen fibrils without the presence of bone cells, has been studied. Directed by protein, the CaP particles nucleated within the collagen fibrils and later grew into elongated crystals within the fibrils [84]. Finally, an *in situ* system was used to study the nucleation of CaP where a 10 mM phosphate-containing solution was added to a gently-stirred solution of calcium ions (10 mM) [133]. Without the presence of bone cells or ECM, the CaP was found to first form a polymeric chain before condensing to spherically-shaped CaP. A similar observation was made using *in vivo* fish models. The spherical dense CaP granules then start forming needle-like texture within them, analogous to what has been observed in other models [133].

Direct observation and an in-depth characterisation of the steps by which the CaP precursor phases change chemically and morphologically, using relevant biomineralisation models as they grow into mature bone mineral, are yet to be explored. Many key questions still remain both about the process that precedes the mineral's propagation on the ECM and the physicochemical format in which the mineral is delivered to the collagen fibrils. Very few techniques are available which provide spatially-resolved information about the chemistry and coordination environment of the different physicochemical formats of CaP in mineralising tissues. The aim of the present study was to apply high resolution transmission electron microscopy (HRTEM) and electron energy loss spectroscopy (EELS) in the scanning transmission electron microscope (STEM) to provide very high spatial resolution information about the step-by-step process by which mineral grows into mature poorly crystalline carbonated CaP. The study also investigated how the chemistry and coordination environment of the mineral changes during their growth on the collagen fibrils. It was envisaged that this information will provide insight into how collagen fibrils are mineralised in bone, which can be used to direct the design of improved synthetic bone implants. This information was then correlated to high resolution images showing the crystallinity of the mineral. The study utilised primary mouse calvarial osteoblast cell culture as a mineralisation model, which has been published previously [3, 120].

EELS can be used to probe the chemical composition and bonding environment of atoms in of the examined material. Electrons, travelling through a sample, lose a portion of energy to excite inner-shell electrons to higher states. These energy-losses (known as core-losses) can be related to the presence of specific elements. In the present study, the K-edges of carbon (~283-303 eV), nitrogen (~396-416 eV) and oxygen (~530-550 eV), and the $L_{2,3}$ edges of phosphorus (~134-154 eV) and calcium (~344-364 eV) were examined. K-edges arise due to excitations of 1s electrons, and $L_{2,3}$ edges arise due to excitations of 2p electrons. Individual peaks in the edges within a spectrum, the energy-loss near-edge structure (ELNES), provide insights into identify the bonding environment of an element.

4.2. Experimental Design

4.2.1. Cell Culture

Cell culture protocols used were previously described in [3, 120]. In short, osteoblasts were derived from two-day old neonatal CD-1 mice. The mice were sacrificed by cervical dislocation according to Imperial College London ethical guidelines. Calvarial tissue from all of the pups in a litter were removed and pooled, washed in phosphate-buffered solution (PBS) (Invitrogen), removed from all soft tissue. The calvaria were then minced with sterile scissors. The minced calvaria were digested in a 1 mg/mL collagenase (Sigma) in Hank's Balanced Salt Solution (Invitrogen) with 10% (vol/vol) solution of 0.05% (wt/vol) trypsin/EDTA (Invitrogen). Four times of digestion (20 minutes each) were followed by a fifth digestion (2 hours). Cells were collected from by centrifugation of the last three supernatants. Cells were then plated in α-minimum essential medium (αMEM) (Invitrogen) supplemented with 15% (vol/vol) foetal bovine serum (FBS) (Invitrogen) and 1x solution of penicillin/streptomycin (P/S) (Invitrogen). For the experiments conducted in this study, cells from the third or fourth passage were used.

4.2.2. Mineralisation Protocol

Neonatal mouse calvarial osteoblasts were cultured on glass cover slips to form mineralised nodules as previously described [3, 120]. Briefly, to induce mineralisation, 30,000 cells/cm^2 was seeded on glass cover slips, and grown in αMEM supplemented with 15% (vol/vol) FBS, 1x Penicillin/Streptomycin (Sigma), 50 µg/mL ascorbic acid (Sigma), and 10 mM ß-glycerophosphate (Sigma), a widely used mineralisation protocol [246]. At the beginning of day 14, 1 µM dexamethasone

(Sigma-Aldrich) was added to the culture. Culture medium was changed every two days. At day 28, the cells were prepared for transmission electron microscopy (TEM).

4.2.3. TEM Anhydrous Sample Preparation

The cells were rinsed with PBS twice and then immersed in anhydrous ethylene glycol (Sigma) for three hours at room temperature [238]. This preparation route is the only room-temperature method which preserves mineral crystallinity, morphology and chemistry [238]. However, this method only weakly preserves the structure of the organic components (i.e. the collagen and cell organelles) because it does not crosslink the proteins [120, 238]. Further, as this method is performed at room-temperature, unbound ions are not preserved since they are lost during washing. The samples were then immersed in dry acetronitrile (Sigma) for ten minutes and replaced with fresh dry acetonitrile another two times (*i.e.* a total of 30 minutes in acetonitrile). The samples were infiltrated with a Quetol-based resin as previously described [3]. Samples were sectioned using ultramicrotome (Leica) for 70 nm thickness and immediately placed on 300 mesh copper lacey-carbon copper grids (Electron Microscopy Sciences). Uranyl acetate (Electron Microscopy Sciences) and lead citrate (Sigma-Aldrich) staining were used in some of the thin sections to enhance the organic or cellular contrast.

4.2.4. Electron Microscopy Imaging and Analysis

All TEM observations were made after viewing multiple areas of at least three separate cell cultures, and all of the mineral analysed in this study are extracellular. Selected area electron diffraction (SAED) patterns were collected by Dr. Suwimon Boonrungsiman [220].

Preliminary bright-field TEM imaging was performed on a JEOL 2000 operated at 80 kV with spot size 1 to maximize mass-thickness contrast with the largest condenser aperture inserted. An objective aperture was used to maximise contrast and minimise sample tearing (knock-on damage).

The JEOL 2100 operated at 200 kV was used for EDX acquisition (Oxford Instruments, IncaEnergy). The sample was tilted in the x-axis for 015 degrees for optimal x-ray collection.

Bright-field TEM, high-angle annular dark field scanning TEM (HAADF-STEM), and STEM-EELS were performed on a Nion Ultrastem™ (SuperSTEM, Daresbury, UK) at 100 kV with 32 mrad and 36 mrad convergence and collection angles, respectively. HAADF-STEM was conducted using 79-195 mrad half angles, and 0.5 eV/channel EELS spectra were acquired from thin areas of relative thickness (t/λ) of less than 0.5.

For the purpose of the damage study, a dose experiment was conducted using a TITAN 30/300 STEM/TEM operated at 80 kV to best replicate the SuperSTEM conditions. The damage experiment evaluated how fine structure at the EELS oxygen edges changed during acquisition and whether the crystallinity of the mineral altered. A dose rate of less than 10^3 electrons/nm^2 per second and a total dose of 10^4 electrons/nm^2 were used according to previous studies [247, 248] as prior work has shown that radiolysis damage can be avoided below this threshold. Phase contrast images were taken using 0.2 s exposure time.

4.2.5. EDX Analysis

To calculate the calcium to phosphorus ratio (Ca/P), the highest height of the EDX peaks of Ca (K_α) and P (K_α) of the sample were processed using Cliff-Lorimer equation according to [120, 248] (refer to Instrumentation Chapter). For the standard, carbonated hydroxyapatite (CHA) standard (Ca/P of 1.76) was used, as described previously in [248]. CHA standard was produced via a sodium free wet chemical precipitation reaction first described by Gibson & Bonfield [249]. CO_2 was bubbled through the $Ca(OH)_2$ solution until the pH dropped to around 4. Aqueous H_3PO_4 (85 vol/vol % Fisher Scientific) was then added a rate of 5 mL/min. No pH control was necessary, as the pH remained above 10.5. CHA sample was provided by Prof. Serena Best, Cambridge University. Statistical calculation was done on ‘n’ areas from two independent cell cultures at a minimum of two ultra-microtomed sections per independent culture.

4.2.6. EELS Analysis

DigitalMicrograph software was used for all TEM images and EELS analysis. The intensity of all the elemental edges were calibrated to the carbon K-edge at 284.5 eV, and shifted along the y-axis. Background subtractions were performed using a power law model (refer to Instrumentation Chapter) modelled with a 30 eV window or wider before the onset of the edge. For the phosphorus edge, background subtraction was performed with a 10 eV pre-edge window to avoid the presence of silicon contamination peak at 99 eV. Identification of phosphorus, carbon, calcium, nitrogen, and oxygen peaks was performed previously by Dr. Michal Klosowski using the CHA standards mentioned earlier [248]. Hyperspy software was used to obtain spectra corrected by Principal Component Analysis (PCA) [250, 251].

Semi quantification of the presence of carbonate (an additional carbon K-edge peak at 290.2 eV [248, 252]; Figure 4.1) was done using curve fitting (multiple linear least squares or MLLS) in the Digital Micrograph software [253]. Post-PCA spectra of amorphous carbon and the combination of [amorphous carbon + carbonate signal] were used as standards for MLLS (Figure 4.1). Pixels containing greater than 80% match to the carbonate spectrum were counted as carbonate-containing pixels. The number of carbonate-containing pixels was divided by the number of mineral pixels to give the percentage of carbonate content. Statistical calculation was done on ‘n’ areas from two independent cell cultures at a minimum of two ultra-microtomed sections per independent culture.

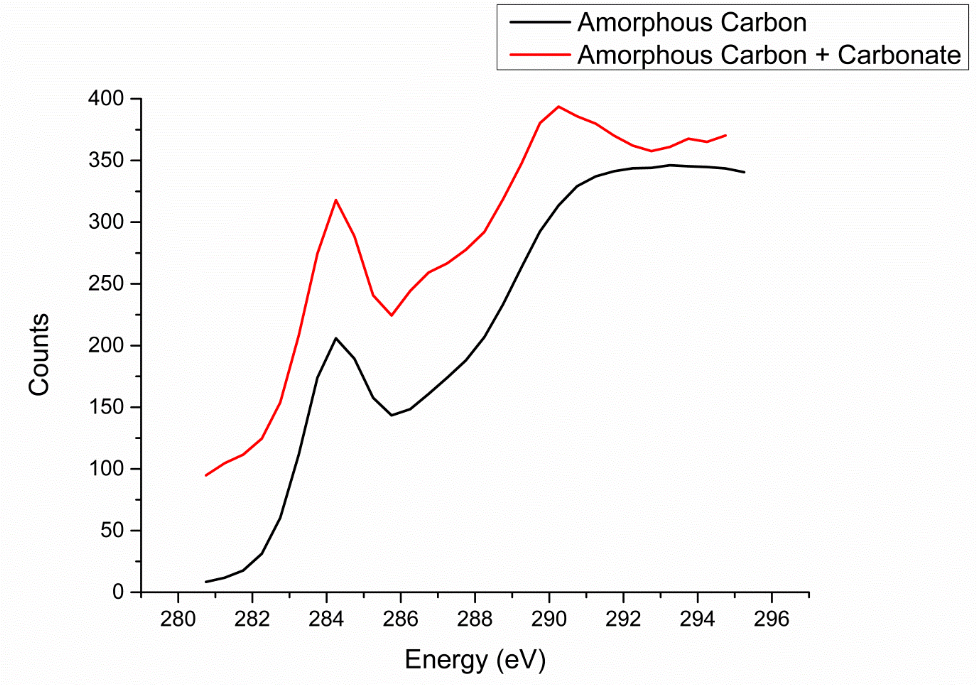

Figure 4.1 Standard curves used for MLLS. The carbonate peak at the carbon K-edge is present at 290.2 eV [248, 252].

4.2.7. Statistical Analysis

Statistical differences between data sets were calculated using one-way Anova with Bonferroni post-test, with *p*-value of less than 0.05 as statistically significant (n>3, where ‘n’ is the number of areas from two independent cell cultures at a minimum of two ultra-microtomed sections per independent culture).

4.2.8. Author’s Declaration

Kharissa Nitiputri performed some of the cell isolation, cell culture, and TEM sample preparation and all of the analysis of the data. Dr. Suwimon Boonrungsiman also performed some of the cell isolation, cell culture, TEM sample preparation, and diffraction experiment. Kharissa Nitiputri performed all of the post-embedding sectioning and staining, EDX acquisition, EELS and EDX data analysis, and writing manuscript. TITAN experiments were done by Dr. Catriona McGilvery together with Kharissa Nitiputri. SuperSTEM experiments were done by Dr. Quentin Ramasse, together with Kharissa Nitiputri.

4.3. Results and Discussion

4.3.1. ECM-Associated Mineral Deposits Vary in Size and Crystallinity and May Represent Different Stages of Maturity

We first investigated the morphology and crystallinity (using SAED) of mineral deposits forming in bone nodules after culture of neonatal mouse calvarial osteoblasts for 28 days in osteogenic differentiation medium. At day 28, preliminary observations of heavy metal-stained sections showed the presence of cells and the ECM (Figure 4.2a). In higher magnification images of the ECM taken from unstained sections, islets of high electron density were present and the SAED pattern taken from these islets show a typical polycrystalline hydroxyapatite (HA) pattern consistent to the known hexagonal crystal form of HA [254] (a= 9.37 Å and c = 6.88 Å) (Figure 4.2b and inset). Some clusters of the mineral crystallites were isolated from the large mineral islets (Figure 4.2b, Figure 4.5; circled areas).

For compositional analyses, we analysed the mineral morphologies which dominated the ECM, using High-Angle Annular Dark Field Scanning Transmission Electron Microscopy (HAADF-STEM) (Figure 4.3). Here the electron beam is condensed down to a probe and rastered across the sample to build up an image. Because of the electron probe size (~1 Å), high resolution images of the mineral structures can be obtained and can be combined with analytical techniques to give chemical information on the nanoscale. Higher resolution images of the isolated clusters of calcium phosphate revealed two different morphologies: smaller- and dense granules (<80 nm in diameter; Figure 4.4, Figure 4.2e (arrow), and Figure 4.3a), and needle-like globules of apatite (100-300 nm in diameter; Figure 4.4, Figure 4.2c, and Figure 4.3b). These isolated clusters have been proposed to be the precursor of the mature mineral (Figure 4.3c), in an acellular system [133] (reviewed in Literature Review Chapter).

Our previous study showed that intracellular mineral granules are present inside the cells and become transported to the ECM [120]. Kuhn *et al*. [255] also observed using TEM circular aggregates of apatite crystals amongst loose apatite crystals in *in vitro* culture. The different CaP morphologies observed in this study were proposed by Mahamid *et al*. [121, 129, 132] in zebrafish fin and rat *in vivo* models. They proposed a progression of bone mineral from a young small-spherical mineral granule to needle-like globules made of apatite crystals that then spread throughout the collagen fibrils. In this study, we observed mineral emanating around the needle-like calcium phosphate globules, which may indicate the needle-like globules as the precursors of the mature needle-like mineral (Figure 4.5b; red arrows). The observation of the mineral spreading from spatially isolated needle-like calcium phosphate globules along collagen fibrils is also consistent with prior work [256].

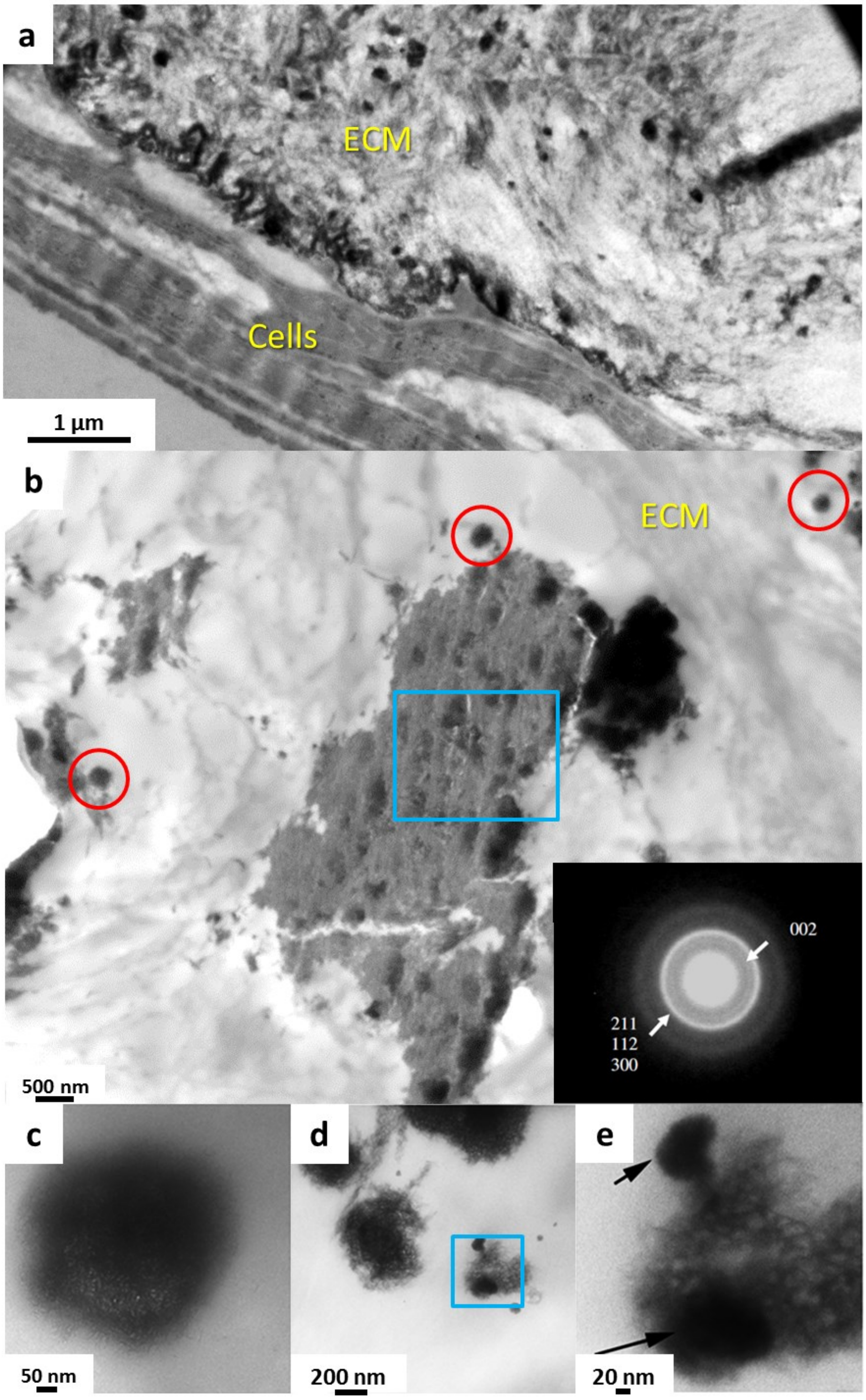

Figure 4.2 Bright field TEM images of anhydrously preserved *in vitro* mineral at 28 days in culture. Image a is post stained using of uranyl-acetate and lead-citrate. Images b-e are not post-stained. Low magnification image showing the presence of cells and the ECM, where the minerals are found (a). Low magnification image (unstained) showing a variety of islet mineral morphologies islets (boxed) and isolated circular aggregates (circled) (b). The insert shows an SAED pattern of an area corresponding to the boxed region. High magnification of the isolated globular structure, showing the needle-like mineral morphology within it (c). Within the globular structures, smaller dense granules were observed (d); the boxed regions are magnified in (e). Changes in the amount of carbonate moieties within the different mineral morphologies will be explored further using TEM spectroscopic analysis (EELS).

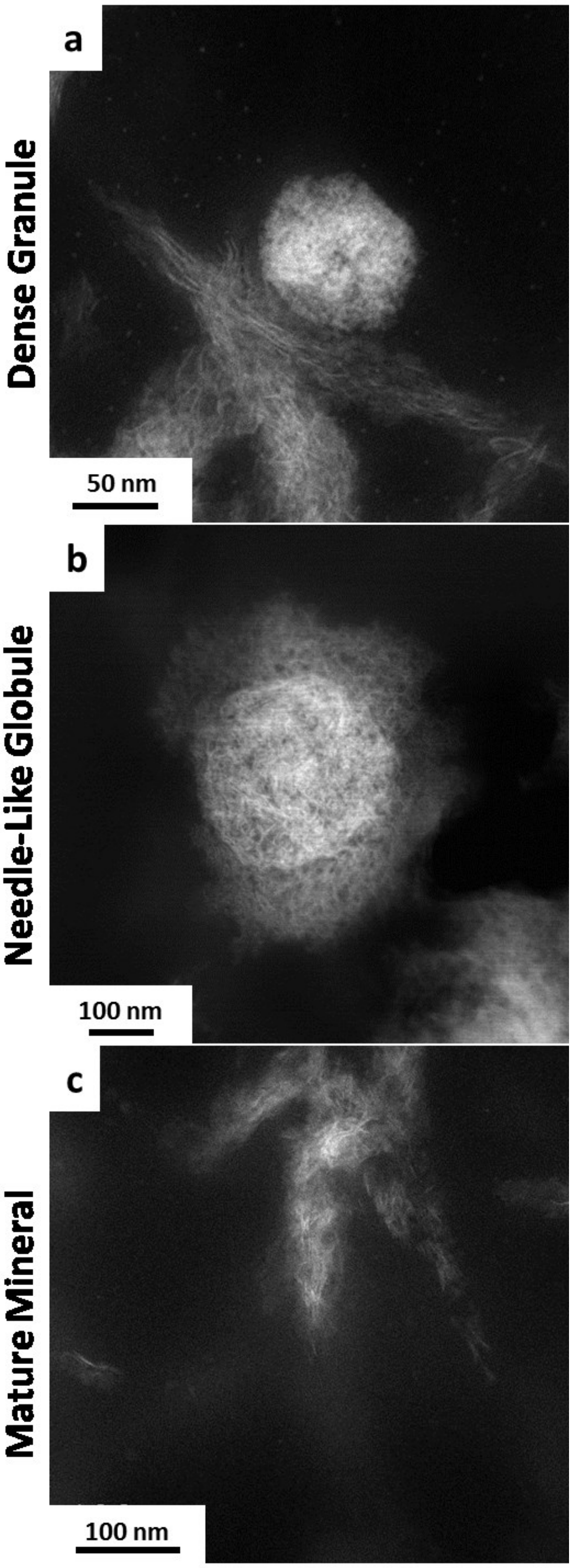

Figure 4.3 Representative HAADF images of anhydrously preserved *in vitro* osteoblast mineral at 28 days in culture showing various morphologies: a dense granules <80 nm diameter (a) (in this case co-existing with the mature mineral), globular apatite comprised of needle-like crystals >100 nm diameter (in this case with mineral emanating from the globular core) (b), and mature mineral with collagen template seen as white smear in the background (c). HAADF images allow better identification between dense granules and needle-like calcium phosphate globules.

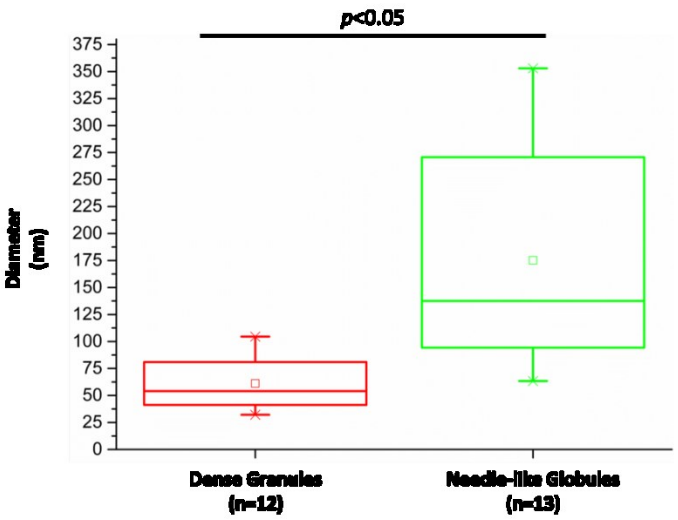

Figure 4.4 Size comparison between dense granules and needle-like calcium phosphate globules. Statistical significance was achieved (p<0.05) between the two groups. The average of sizes of the dense granules and the needle-like globules were 61 nm (standard deviation of 25 mm) and 175 nm (standard deviation of 97 mm), respectively. The maximum and minimum ranges of the values are denoted by the vertical lines above the box of the box plot. The end whiskers (horizontal line) of the box plot represent the 5th and 95th percentiles, which in this case is also coincide with the 1st and 99th percentiles denoted by ×. The box of the box plot represents the 25th and 75th percentiles with the mean denoted by ▫. The horizontal line going through the box represents the median of the data set. 'n' represents the number of areas from two independent cell cultures at a minimum of two ultra-microtomed sections per independent culture.

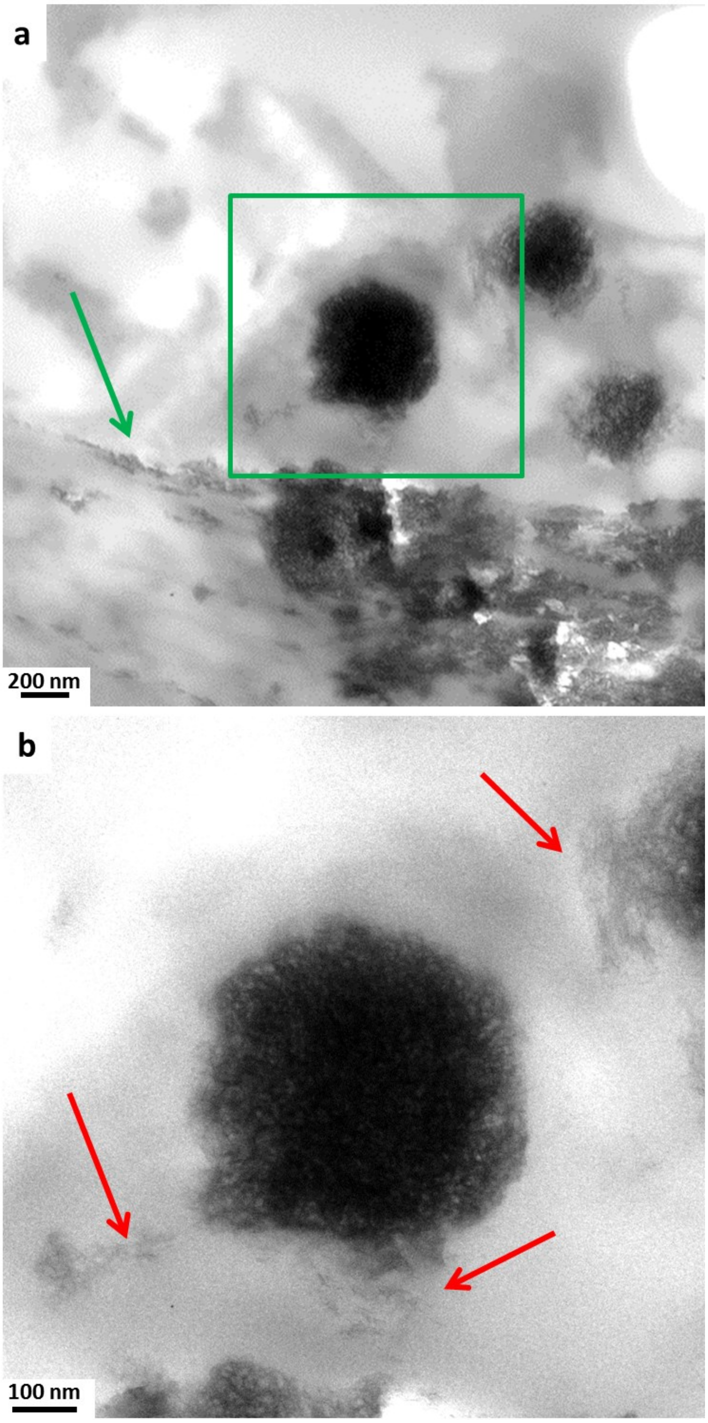

Figure 4.5 Bright field TEM images of anhydrously preserved *in vitro* osteoblast mineral at 28 days in culture. These images of an unstained section of shows mineralising areas and needle-like mineral globules on the surface of, and surrounding of needle-like mineral globules. Collagenous areas are the regions with grey contrast around the mineral (here shown to be partially mineralised; green arrow) (a). A higher magnification image of the boxed region in a (b), with red arrows showing the spreading of the mineral apatite from the globule, indicating that the mature mineral observed (in Figure 4.2b-boxed region and Figure 4.3c) originates from the globule.

4.3.2. Crystalline Domains observed for the First Time in All Undamaged Mineral Types

A damage experiment was previously conducted in [248] by measuring the occurrence of an oxidation peak at around 530 eV of the oxygen K-edge (Peak X at

Figure 4.6). The study showed that 10^4 electrons/nm^2 is the threshold dose before the onset of damage can be detected [247, 248], and hence the EELS acquisition would need to be conducted using doses below this number. This 530 eV peak at the oxygen K-edge is a good marker of early damage modifications of the sample's chemistry, and is induced by formation of O_2 oxygen molecules [257] or other forms of oxygen radicals, like OH or CO. Further, a total dose of more than 10^5 electrons per nm^2 would result to the oxygen K-edge resembling that of calcium oxide [24]. The experiments conducted here employ a dose below this threshold for damage.

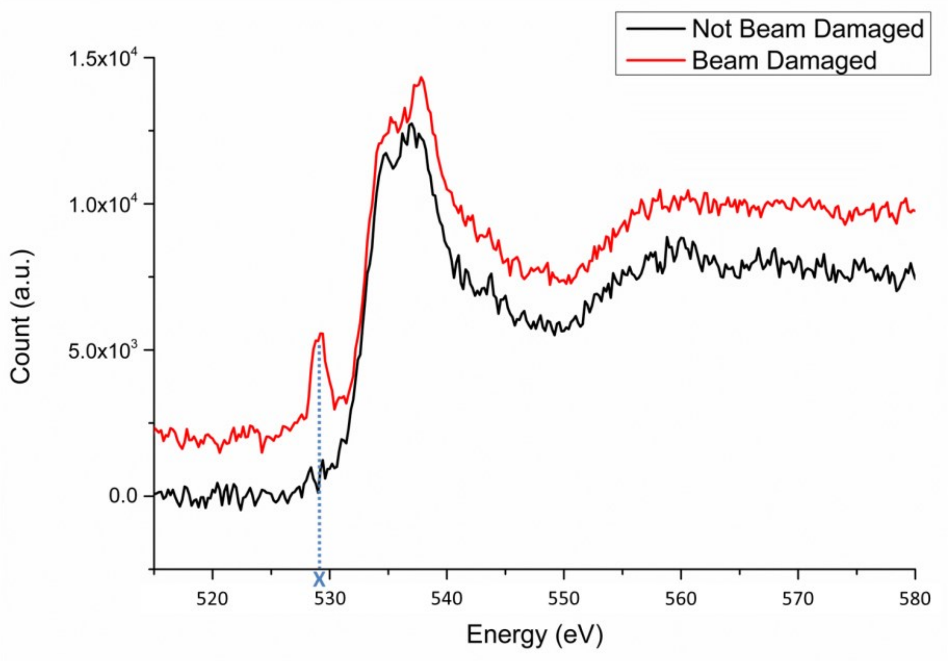

Figure 4.6 EEL spectra of damaged day-28 anhydrously prepared *in vitro* osteoblast mineral particles are detected with the appearance of the peak X at around 530 eV at the oxygen K-edge.

The crystallinity of the mineral apatite found in the sample was observed using low-electron-dose imaging using a dose of less than 10^4 electrons/nm^2 [247, 248] in phase contrast HRTEM mode. Lattice fringes (~10 nm) showing crystalline domains were detected from within all of the different mineral morphologies indicating a degree of crystalline order within these structures (Figure 4.7). The observation of crystallinity by SAED in the needle-like globules and mineralised ECM (mature mineral) is consistent with previous studies on *in vivo* mouse bone and mouse osteoblast culture [120, 132]. Our observation that crystalline domains exists in the initial *in vitro* mineral has yet been reported as the bulk characterisation performed previously showed the initial mineral to be amorphous via SAED [121, 129, 132]. However, our observation is consistent with previous work by Wang *et al*. that showed the presence of crystalline domain of around 5 nm in amorphous calcium phosphate in supersaturated aqueous solution [258].

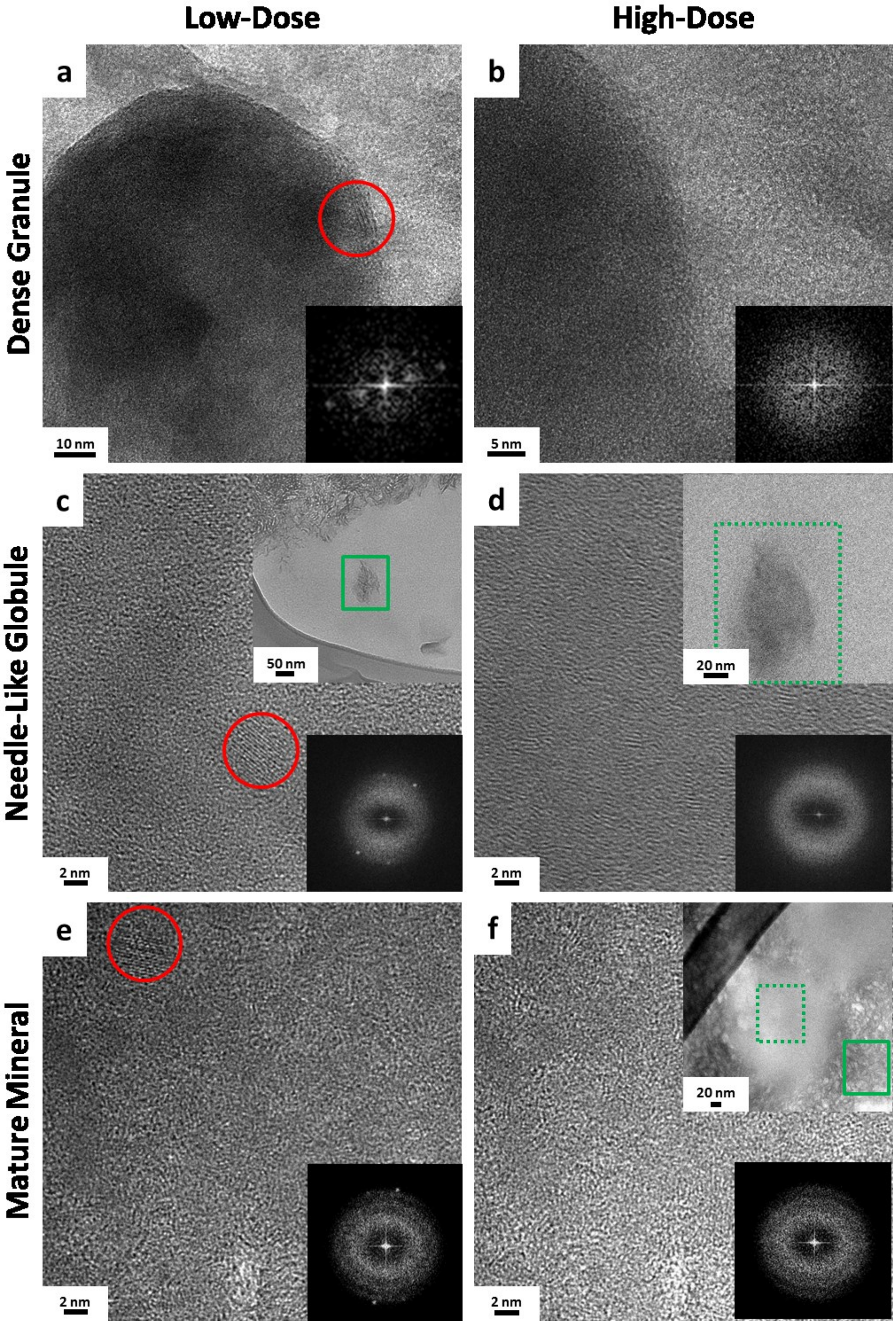

Figure 4.7 4.8 Phase contrast images of anhydrously preserved *in vitro* osteoblast mineral at 28 days in culture; their respective fast Fourier transforms at right bottom corner of each images (taken from the whole image), showing the presence (red circles) or absence of lattice fringes. Images a, c and e were taken using doses (<10^4 electrons/nm^2), which is a low dose experiment. Another set of images (b, d, f) were taken after the samples were exposed to >10^4 electrons/nm^2. Lattice fringes were seen on dense granules at low electron dose (a), needle-like globular apatite (c), and mature mineral (e). After exposure to an electron doses >10^4 electrons/nm^2, lattice fringes were not detected (b, d, f). The inset in f showed damaged (fuzzy; non-textured; dashed-green rectangle) and undamaged areas (solid-green rectangle) surrounding the damaged area.

We also observed that lattice fringes disappeared after prolonged beam exposure of around one or two seconds after taking the first image with a 0.2 s exposure time. When regions with no lattice fringes were exposed to higher electron doses, they preserved their lack of atomic order, demonstrating that beam damage does not induce crystallisation of the mineral. Mentioned previously, some studies have shown that the precursor mineral is amorphous by the means of SAED. This measured difference to our own work may have arisen due to lack of controlled experiment which evaluate the effects of beam damage on the crystallinity of the mineral during the acquisition of the diffraction pattern [121, 129, 132].

Taken together, our findings support the notion that there is a progression of maturation of the mineral - prior to ECM mineralisation, ACP could be converted to crystalline apatite via an intermediate phase composed of globules of CaP comprised of crystalline needles, where a dense core acts as a seed for CaP growth. To confirm this hypothesis, we next examined the chemical composition of each of the mineral morphologies in the ECM.

4.3.3. Chemical Composition Analyses Demonstrate Variations in Ca/P of Mineral Morphologies Indicating Different Stages of Maturity

To test the hypothesis that the different mineral morphologies represent mineral at different stages of maturation, we characterised the Ca/P from EDX spectra. The dense granules had a Ca/P ratio of 1.29 (standard deviation of 0.26) that was statistically lower than the needle-like globules (ratio of 1.58; standard deviation of 0.19) and mature crystallites (ratio of 1.51; standard deviation of 0.17). Dense granules had a Ca/P that was lower than that measured from synthetic ACP of 1.5 [259] and synthetic crystalline hydroxyapatite mineral of 1.67 [260]. Overall, the Ca/P values were within the values of biological apatites as reviewed in [59]. With an *in vivo* mouse model, Mahamid *et al*. averaged the values of Ca/P to be around 1.58 for mature extracellular matrix, and around 0.75 for the intracellular mineral-containing vesicles that were hypothesised to be the precursor of the mature material [121]. The values of the Ca/P between this study and Mahamid’s are not exactly the same, and this may be because of the difference in where the mineral is found (i.e. intracellular vs. extracellular) and their maturity; nevertheless, the trend of increasing Ca/P as bone mineral matures was similarly observed both in [121, 129] and in our studies. In our calculation of the Ca/P, the dense granules are categorised as biological amorphous calcium phosphate [59]. Together, these data indicate that the Ca/P ratio increases successively between the dense granules, the needle-like globules and the mature crystallites formats, which further supports the hypothesis that the former are a transient precursor phase in mineralising bone.

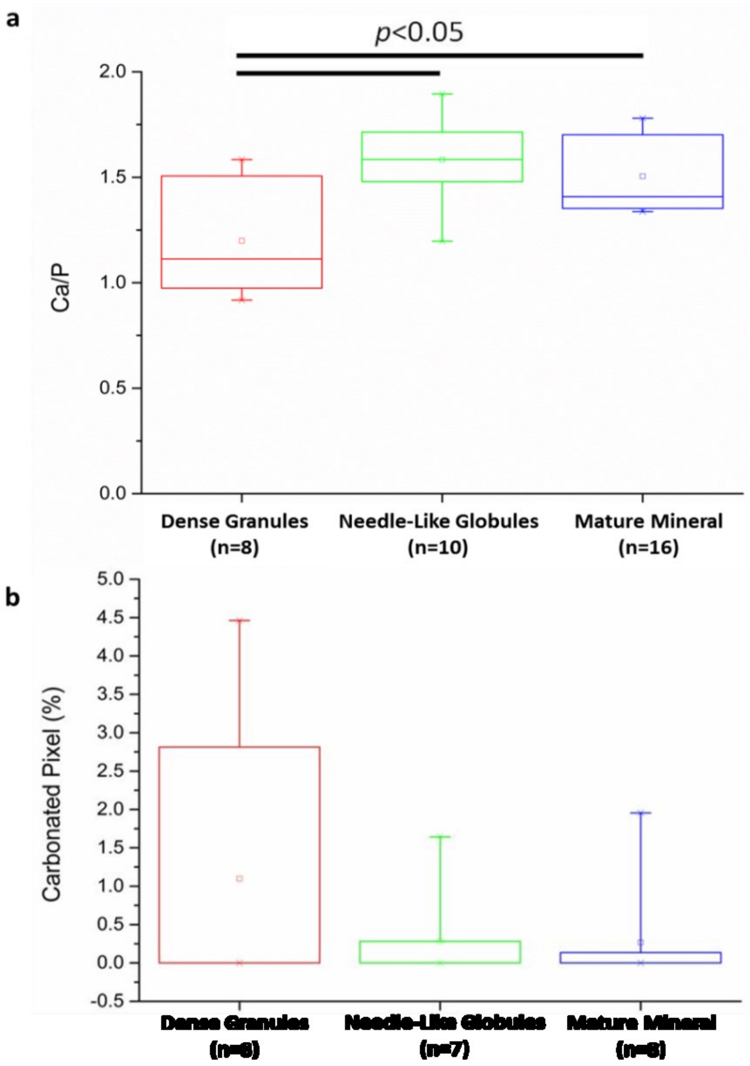

Figure 4.9 Calcium and phosphorus ratios taken from EDX spectra of anhydrously preserved *in vitro* osteoblast mineral at 28 days in culture (a) and semi-quantification of the carbonate peak taken from the EEL spectra (b), in the different stages of mineral maturation. The youngest minerals (dense globule) have the lowest Ca/P ratio (average = 1.29), and more mature minerals (needle-like globules and mineralised collagen, averaged at 1.58 and 1.51, respectively) have higher values. Median of figure b is zero. Refer to Table A 4 for a complete list of Ca/P values measured. The youngest mineral has the highest carbonate content. The maximum and minimum ranges of the values are denoted by the vertical lines above the box of the box plot. The end whiskers (horizontal line) of the box plot represent the 5th and 95th percentiles, which in this case is also coincide with the 1st and 99th percentiles denoted by ×. The box of the box plot represents the 25th and 75th percentiles with the mean denoted by ▫. The horizontal line going through the box represents the median of the data set. 'n' represents the number of areas from two independent cell cultures at a minimum of two ultra-microtomed sections per independent culture.

4.3.4. EEL Spectrum Imaging Demonstrates a Dense Cluster of Intense Carbonate Signal in the Core of the Granules which Becomes Less Intense and Less Localised as the Mineral Matures

To further elucidate whether the chemistry differs between each of the mineral morphologies, and to provide further insight about how the mineral nucleates and grows as it matures, we performed EEL nanospectroscopy to map the chemical composition, bonding and coordination environment of atoms in the three different mineral morphologies. The electron probe is moved serially across the sample and an EEL spectrum is recorded at each probe position, thus forming a 'spectrum image' from which chemical information can be extracted. In all morphologies, we confirmed the presence of, in varying amounts, phosphorus (L2,3-edge), calcium (L2,3-edge), nitrogen (K-edge), oxygen (K-edge), and carbon (K-edge) of the apatite mineral are shown in Figure 4.10 and Figure 4.11. EEL reference spectra were taken using CHA standards [248]. We have included the bond assignments for each of these edges in Table A 2 and Table A 3, based on known energy losses for these bonds.

The most striking variation between the different mineral morphologies were observed in the fine structure of the carbon K edge, which allowed us to study differences in the level of carbonate. It is well known that *in vivo* bone carbonate content increases as bone matures [134, 135, 261, 262], and we considered that it might be the case that we could track carbonate substitution in the maturation of mineral in this study.

Further smoothing of the carbon K-edge was done using PCA to identify and semi-quantify smaller carbonate peaks. Small peak was detected at 290.2 eV, contributed by the main core 1s transitions to vacant π*-A states of CO_3 groups, could be assigned to the presence of carbonate group (Figure 4.11; blue line) [252, 263, 264]. The observation of a carbonate group using EELS is consistent with our previous study using Raman spectroscopy on the bone nodules of cultured mouse osteoblasts used in this study [3].

Semi-quantification of the number of regions of mineral containing carbonate was conducted to assess whether the amount of carbonate present within the mineral changes between the different morphologies [261, 265]. The dense granules contained more carbonate than the more mature crystallites. The greater spread of carbonate content in the dense granules may be contributed to a carbonate signal that is below the detection limit in some pixels. On the contrary to *in vivo* system's increasing bone carbonate content overtime, higher presence of carbonate in the young *in vitro* mineral than that in older mineral has been seen in previous *in vitro* studies performed by Rey *et al*. using bulk techniques (X-ray diffraction and FTIR) [134, 135].

It is also observed that the majority of the carbonated areas were located in the middle of the dense granules (Figure 4.11a and d). This measurement supports the findings of a recent study that hypothesised that calcium-carbonate deposits are the bio-seed of the calcium phosphate deposition process [136].

Spectra taken from the dense granules (Figure 4.11a) and the needle-like calcium phosphate globules (Figure 4.11b) also showed a shoulder at 287.5 eV (red line) [266] that originated from the 1s→π* of the carbonyl (R-C=O) group. The presence of the carbonyl peak may be the result of proteins present within the mineral, as some proteins were seen to stabilise minerals [267], such as fetuin [56], osteopontin and osteocalcin [268]. Detection of the nitrogen K-edge from these regions (discussed in the next section 4.3.5) within the mineral also supports this hypothesis.

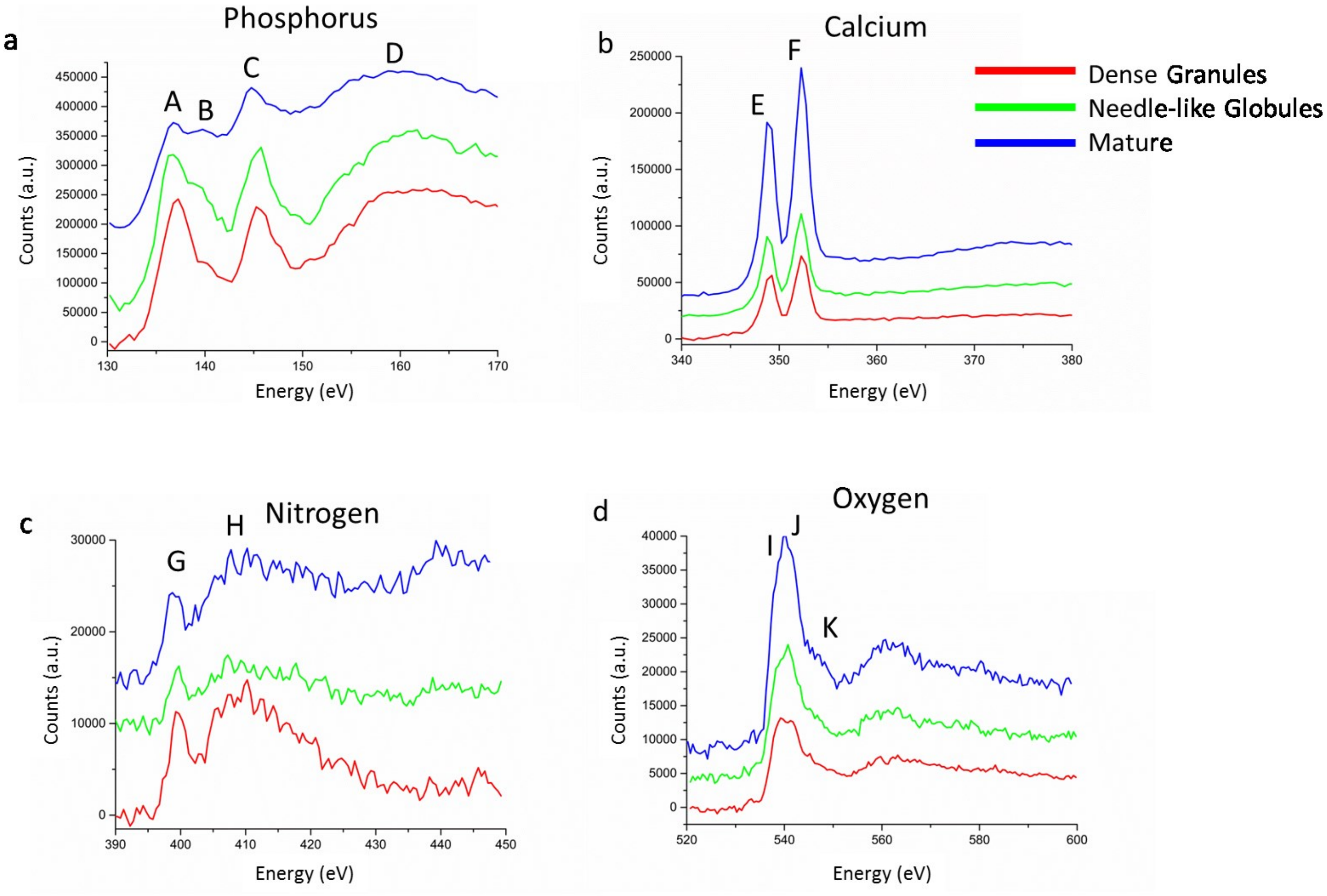

Figure 4.10 Representative EEL spectra of various elements from the different mineral morphologies of day-28 anhydrously prepared *in vitro* osteoblast. The $L_{2,3}$-edge for phosphorus, $L_{2,3}$-edge for calcium, K-edge for nitrogen, and K-edge for oxygen. The peaks (A-K) are described in the appendix (Table A 2) and have been assigned using [248].

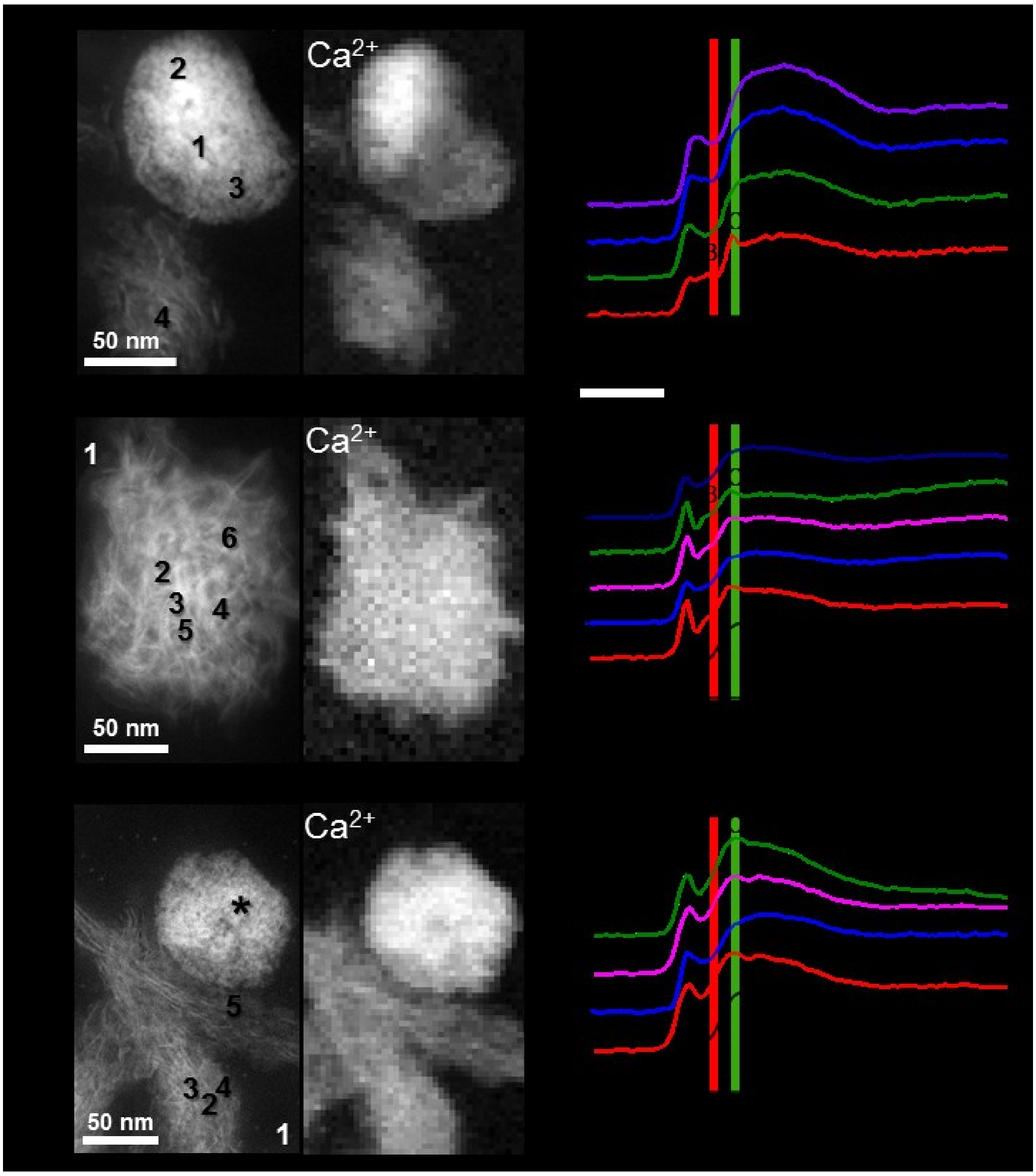

Figure 4.11 HAADF images of anhydrously prepared day-28 *in vitro* osteoblast minerals with their corresponding EEL spectra. An example of carbon-K-edge EELS spectra taken from various points within a dense granule (a), a needle-like globules (b), and mature mineral (c). Dense granule is shown in (a) and its corresponding carbon edge in (d). Figures b and c, are examples of submicron sized needle-like globules and mature regions of the mineralised tissue, respectively, and figures e and f shows their respective carbon edges. The presence of the carbonyl group (position indicated by red line and 'B' in figures d, e, f) can be detected from a small peak at 287 eV. The presence of carbonate (position indicated by blue line and 'C' in figures d, e, f) can be detected from the small peak at 290.2 eV (spectra 2, 3, and 4 in d). The carbon K-edge was also detected from the resin-only areas (treated as the controls). The description of the other peak positions is presented in the appendix (Table A 3) [248]. Asterisk in figure c represent a dense granule.

4.3.5. Nitrogen K-edge Indicating the Presence of Collagen or Non-Collagenous Proteins

The presence of protein moieties can be detected by the presence of carbonyl group at the carbon K-edge and by the detection of nitrogen K-edge. The nitrogen edge was obtained using the steps used to obtain the carbon K-edge. The nitrogen K-edge spectra consists three peaks at ~400 eV, 401 eV, and a broad peak at ~410 eV [269]. Because of the low energy-resolution, the first two peaks are seen to be creating one peak (Figure 4.10).

The peak at 400 eV is thought to be associated with 1s-π* transitions from nitrogen incorporated in an aromatic ring (an essential part of collagen crosslinking) [270-273]. The peak at 401 eV is thought to be connected with oxidised pyridine [270, 271], or 1s-π* transitions in the nitrated carbon structure [272, 274], or 1s-π* transitions in glycine amide groups (C=ONH) [275]. The broad peak at ~410 eV is attributed to 1s-σ* transitions in amino compounds [270]. With the peaks assigned, the nitrogen detected may result from either the collagen environment [29] or the presence of non-collagenous proteins (such as those mentioned in the previous section). The nitrogen signal was either seen to co-localise to the mineral or to white-cloudy structures around the mineral, which are possibly collagen fibrils (Figure 4.12). The nitrogen signal detected from within the dense globules and needle-like calcium phosphate globules, could also account from the presence of non-collagenous protein that has been proposed to stabilise young minerals [89, 267, 276].

4.4. Discussion and Conclusion

Mineralisation processes represented by the animal models or acellular models used in previous works may not be fully relevant to that in humans [84, 121, 129, 132, 133]. For instance, the body temperature of fish is regulated by ambient water temperature, whilst human is kept relatively constant at 37°C. This difference in body temperature may affect the phase transformation kinetics of the nucleating and maturing mineral [121]. Furthermore, models that simplify the bone environment even more [84, 130, 133] (i.e. acellular model or completely inorganic model) is simplified and may lack constituents which control bone mineralisation processes in humans. Studies have used models that more closely mimic the human environment than the mentioned models did. For instance, i*n vivo* mammalian [121] or mammalian cells have been utilised for *in vitro* studies [120, 121, 135, 277]. For instance, Mahamid *et al.* reported that the ACP mineral precursor phases found in the fish model were also found in a mouse model. However, in the cold-blooded fish model, the intracellular mineral-containing vesicles were granulated and not organised into 80 nm individual granules like that found in the mouse model [121, 129, 132].

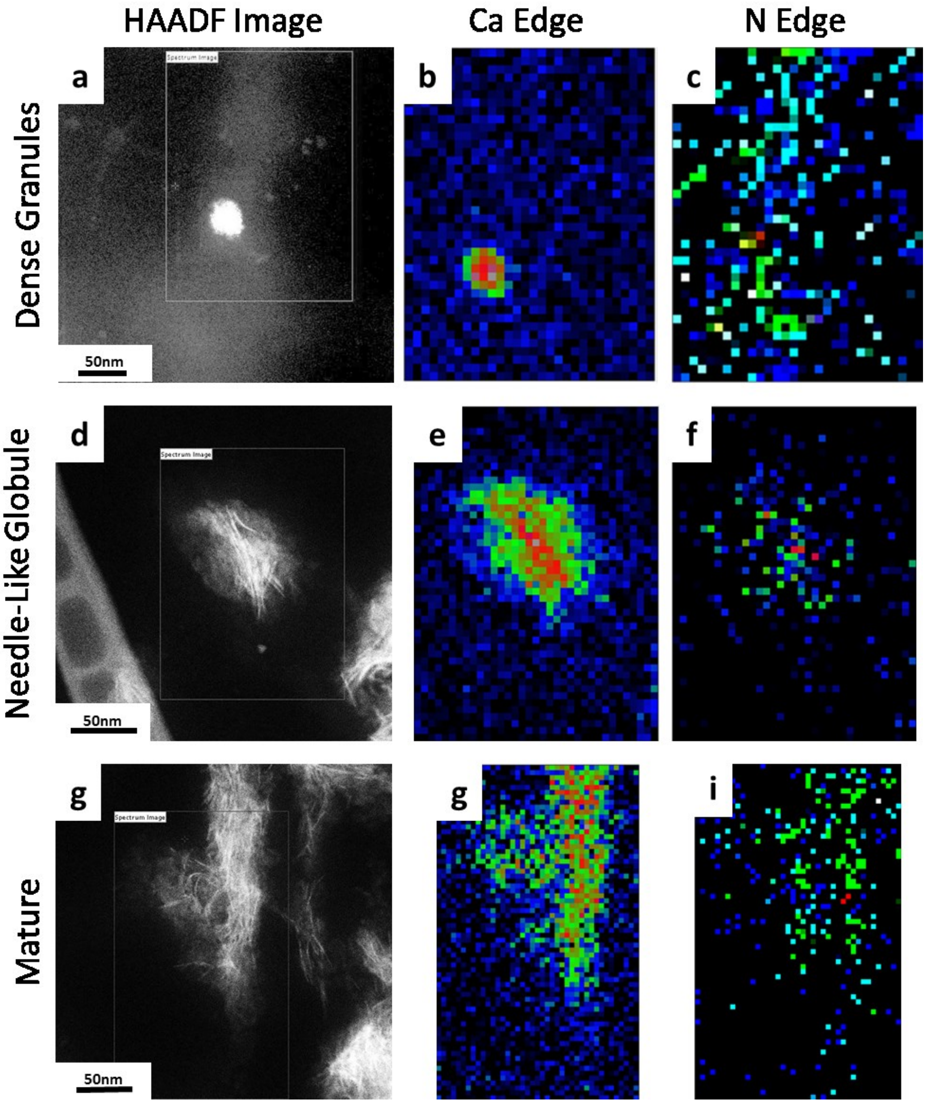

Figure 4.12 HAADF images of anhydrously prepared day 28 *in vitro* osteoblast minerals with their corresponding calcium and nitrogen heat maps. Calcium and nitrogen maps (from the integrated nitrogen signal at the nitrogen K-edge; integrated window was 30 eV starting from the onset of the EEL spectra peaks of calcium and nitrogen edge taken from different mineral morphologies, which may represent different stages of mineral maturation.

In this study, we showed the presence of three different CaP structures within the mineralising osteoblast cultures: <80 nm dense granules with low a Ca/P ratio and crystalline domains; needle-like globules comprised with diameter >100 nm, and mature mineral, both with statistically higher Ca/P ratios compared to that of the dense granules. Many of the submicron granules were interspersed around the fibrillar structures containing nitrogen, which are probably are the collagen fibrils. Our high resolution TEM also revealed the presence of crystalline domains in the dense granules and the needle-like globules, an observation that was not previously detected by SAED [120, 133].

Several previous studies have suggested that early mineral precursors originated from the cells [120, 121]. These studies showed the existence of phosphate-rich intracellular vesicles that are hypothesised to provide the appropriate environment for ACP nucleation. Boonrungsiman *et al*. suggested that mitochondria act as mineral stores for CaP granules which conjoin with the phosphate-rich vesicles inside the cells which deliver CaP to the ECM [120]. Mahamid *et al*. showed that the intracellular vesicles contained ACP globules of ~80 nm in diameter (similar to the size of our dense granules) that is composed smaller spherical subunits [121]. These nucleated mineral precursors would then be deposited in the ECM before undergoing further maturation transformations [120].

The studies mentioned above showed the existence of intracellular CaP-containing vesicles that were hypothesised to be the precursor mineral for bone mineralisation [120, 121]. These studies, however, did not show the direct link between the granular intracellular mineral and the extracellular mature mineral. With the recent publication of acellular experiment by Habraken *et al*. showing morphological changes from dense granules to needle-like globules and then mature mineral [133], we hypothesise that our dense granules are the youngest mineral that links the intracellular mineral with the extracellular mature mineral. We also hypothesise that as the dense granules mature, their morphology is transformed to become the needle-like globules, and finally the mature mineral (mineralised collagen).

It is well known that *in vivo* bone carbonate content increases as bone ages [57, 127, 135]. However, previous studies have noticed that the trend is reversed in *in vitro* cultures [134, 135]. These previous bulk measurements using FTIR showed that the carbonate content of *in vitro* cultured chick osteoblasts was halved to 0.3% when the culture period was extended from 30 days to 60 days [134, 135]. Using EELS, we have detected and mapped the presence of carbonate in apatite mineral. A greater carbonate content value was detected from the younger dense granules than from the more mature minerals, which is in line to the trends observed previously [134, 135]. With a decrease of only 0.3% achieved in 30 days in the mentioned studies, it is not surprising to see that the carbonate content measured here (in one time point; day 28) is not statistically significant.

With high spatial resolution EELS mapping, we were able to provide spatially resolved maps showing the distribution of carbonate in the mineral. We found that the carbonate was located in the middle of the apatite granules, suggesting that the nucleation of the younger mineral starts with a carbonate-containing precursor. This observation aligns will with a recent study that suggests that calcium-carbonate deposits are the bioseed for calcium phosphate deposition processes in bone, although direct evidence for this hypothesis was not provided [136]. Further, other studies looked into spontaneous precipitation of ACP in solution containing calcium and phosphate ions [278, 279]. These studies observed that stable ACP was produced in the presence of carbonate ions from supersaturated aqueous solutions. Taking these previous observations and ours, it is possible that the carbonate seen in the middle of our youngest mineral may be a residue of the initial stabilisation events during which rapid precipitation of calcium phosphate occurred from supersaturated aqueous solutions.

The existence of ACP in bone was first proposed in 1965 [280]. Its beginning and transformation into crystalline apatite were only recently shown close to fifty years later [130, 133]. Generally, amorphous mineral precursors, such as ACP, had been previously suggested to be a universal transient precursor to mature mineral in vertebrates and invertebrates [121, 129, 132, 281-283]. Previous acellular studies had shown that ACP could be converted to crystalline apatite *in vitro* in a solution containing calcium and phosphate [133, 258, 278, 279], showing that ACP was more labile than crystalline apatite. It is argued that being labile, ACP may serve as immediate precursor for bone apatite or as a readily available source of mineral ions for metabolism [70].

The presence of nitrogen within and surrounding the mineral was also showed by the EEL spectra. Along with the possible detection of carbonyl (R-C=O) peaks, these observations could indicate the presence of protein, which mostly contributed by collagen [28, 29, 248]. The nitrogen signal found in the centre of the mineral (e.g. Figure 4.12f) may also indicate the presence of a mineral stabilising or nucleating protein.

This chapter analyses minerals from day-28 old culture. After day-14 of culture, similar mature mineral to that in day 28 cultures on the collagen fibrils were observed (Figure 4.13), however the ACP dense granules and needle-like globules were not found in this minimal preliminary observation. The reason for this difference could be that protein-assisted collagen mineralisation precedes the cell-mediated mineralisation. Another hypothesis was described by Habraken *et al.* [133] who showed that some of the calcium phosphate strands directly transformed into mature apatite (needle or platelet-shaped), bypassing the spherical (dense granule) precipitation. Using their observations, it could be possible that at the earlier time point, the maturation process is dominated by the direct transformation to apatite, and only later that granular particles are 'produced' on the collagen template which help to direct this transformation.

In summary, we have combined scanning transmission electron microscopy (STEM) with electron energy-loss spectroscopy (EELS), as well as high resolution transmission electron microscopy (HRTEM), to analyse anhydrously preserved samples for the first time. This provides high spatial resolution (probe size of ~1 Å) analytical information about the step-by-step process by which the mineral grows into mature poorly crystalline carbonated hydroxyapatite in the ECM of *in vitro* calvarial osteoblasts. Specifically, we demonstrated that carbonate rich calcium phosphate dense granules are found at the collagen matrix, and may act as seed for growth into larger, submicron-sized, needle-like globules of apatite mineral with a different stoichiometry: these globules appear to mineralise the collagen fibrils forming crystalline textured crystals with a higher Ca/P ratio and with lower carbonate content as the mineral phase of bone. The use of a carbonate rich, ACP spherical bioseed, could be a process by which a soluble CaP phase is stabilised and delivered to the collagen for subsequent maturation and collagen mineralisation. There are some evidences that mineral-stabilising protein may be involved in mineral maturation. Future work using membrane sensitive stains is needed to assess whether the calcium phosphate material is localised within matrix vesicles.

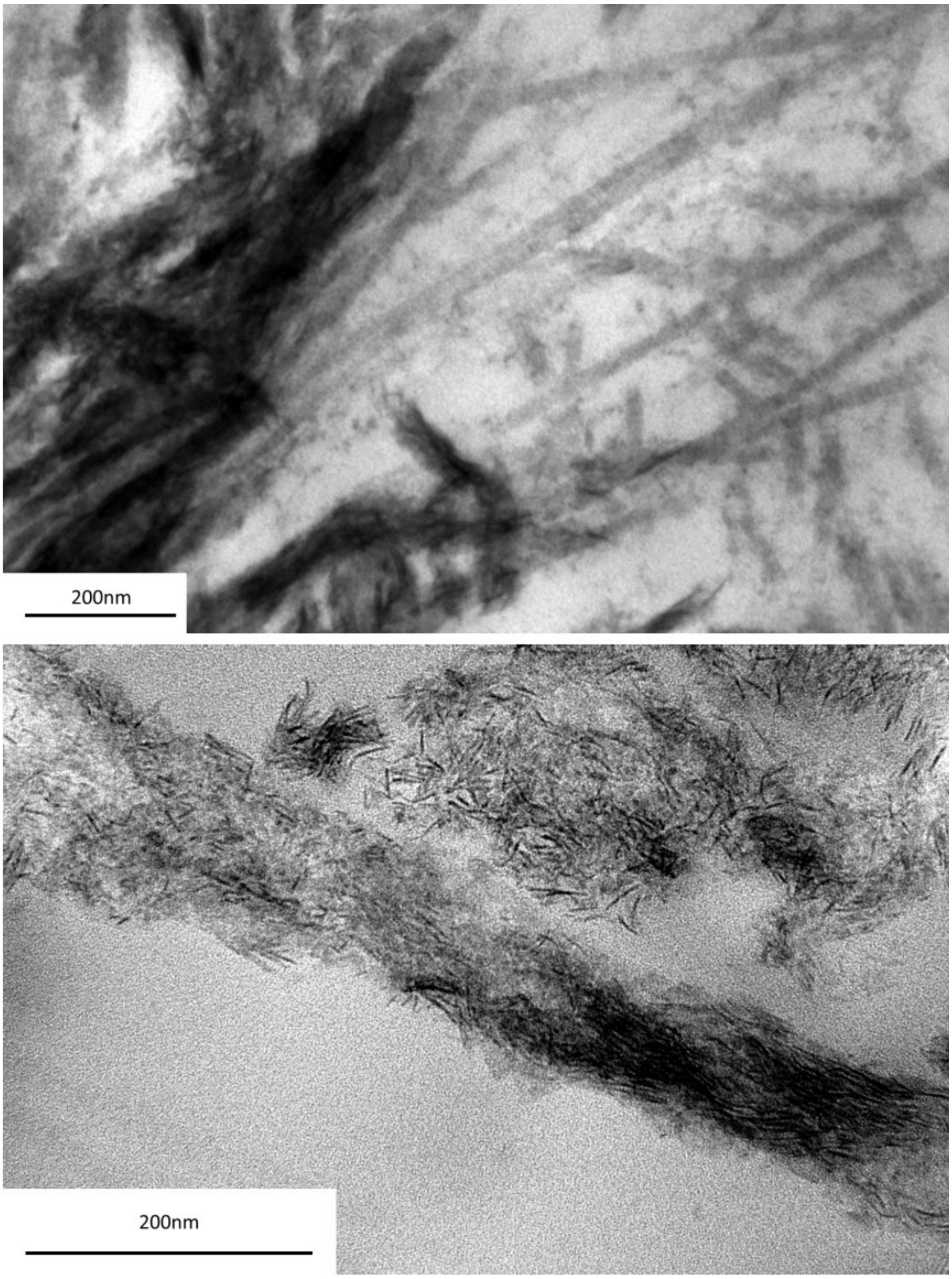

Figure 4.13 Bright field TEM images of anhydrously prepared day 14 *in vitro* osteoblast minerals. Stained section (Top) shows the presence of collagen fibril as the template of mineralisation. Unstained section (bottom) shows the presence two different morphologies of mineral: amorphous (fuzzy) and needle-like mineral.

5. Effect of Strontium Ion Supplementation on *In Vitro* Osteoblast Matrix

5.1. Introduction

The use of strontium ions has been popularised as an anti-osteoporotic agent by Servier's strontium-ranelate drug Protelos® [187]. It has been suggested that strontium ranelate treatment increases bone strength and mass with increased in bone volume and trabecular number and thickness [146]. These led to the reduction in the risk of fractures in women with postmenopausal osteoporosis, and led to a significant improvement in the quality of life after five years of treatment [147, 148].

The main effects observed in osteoporotic women treated with strontium ranelate are related to the presence of supplemented strontium ions. In fact, strontium ions in different salt forms have been also found to have positive effects on bone mineralisation [284, 285]. For example, there have been *in vivo* studies showing that strontium chloride did not produce deleterious effects on body growth, and stimulated bone formation when given to rats as its dietary supplement for eight weeks [186, 197]. It was observed that strontium chloride supplementation increased osteoid surface, osteoblast surface, and bone forming surfaces in rats [144]. Bone resorbing cells were also seen to be transiently reduced with the strontium supplementation in mice [145]. Following these studies, many bone substitutes have incorporated strontium in their compositions [205, 286-289], and many studies have focused on investigating the effects of strontium ions and their mechanism of action.

To reduce the complexity of *in vivo* investigations, *in vitro* systems are often used to elucidate how strontium ions produce such positive effects in bone mineralisation. Broadly speaking, these studies look into how strontium ions affect bone cells, bone matrix, and bone mineral (reviewed in more detail in Literature Review chapter):

The effect of strontium supplementation *in vitro* has been well documented: strontium-supplemented bone culture showed strontium chloride's inhibitory effect on bone resorption after 10 days in the concentration of 5 mM [188]. Another study showed that 1 mM strontium ranelate transiently stimulated the replication of preosteoblasts in calvarial bone cultures in two days [155]. These authors also showed that strontium treatment on cells pooled from calvaria had an increased number of fibroblasts, pre-osteoblasts, and osteoblasts, and that increases in collagen and non-collagenous protein synthesis within 24 hours were detected from pooled osteoblasts [155].

Most recently, studies by Querido *et al*. and Rossi *et al*. looked into the changes that 0.05 mM and 0.5 mM strontium ranelate caused to mineralisation in osteoblast cultures [182, 290]. These studies confirmed previous findings that strontium was incorporated into the newly-formed bone [149-151] and did not cause severe changes to the mineral [150, 152]. However, Querido *et al*. more importantly showed that strontium incorporation into the mineral in a dose-dependent manner resulted in an increase of lattice parameters a and c while preserving the mineral's crystallinity. Strontium incorporation also did not cause changes in the overall cation-to-phosphorus ratio (i.e. the Ca/P was the same as the [Ca+Sr]/P). It was also found that 0.5 mM strontium ranelate supplementation led to an increase in carbonate content (CO_3^{2-}) in the mineral. This increase was postulated to be responsible for the creation of vacancies in calcium and hydroxide sites to maintain charge neutrality [290].

The studies mentioned above did not analyse the contribution of strontium supplementation to bone matrix where the mineral is found. As a consequence, one of the aims of the study was to decipher the effect of strontium ions on bone matrix. Very few *in vivo* studies have investigated the effect of strontium supplementation on the bone matrix [151, 184]. However, it has been argued that the interaction between strontium and collagen may still be involved in the cross-linking of collagen, as well as collagen and mineral ionic coupling [183]. Since about 25-35% of the present strontium was reported to be located in the matrix [183], further studies are needed to understand the effect of strontium on bone matrix including whether different doses of strontium supplementation result in various effects on the bone matrix.

Studies are also yet to comprehensively address the impact of strontium counter ions or species on bone mineralisation. To the best of our knowledge, only a study by Yamaguchi and Weitzmann has reported such a case by comparing: (1) strontium ranelate groups (intact strontium ranelate); (2) strontium chloride groups; and (3) groups treated with a combination of strontium chloride and sodium ranelate, where all groups have the same final strontium ion concentration [291]. In their study, it was reported that MC3T3 mineralisation at day 17 was promoted only by those supplemented by intact 200 µM strontium ranelate [291]. Hence, this study indicates that various strontium counter ions or species contribute to the overall effects of strontium supplementation.

The purpose of this current study is to evaluate the effect of strontium supplementation in an *in vitro* osteoblast system. Greater focus will be directed to the analysis of the effect of strontium supplementation on to the osteoblast matrix. This current study uses TEM and Raman spectroscopy to allow collagen fibril's submicron observation and comprehensive analysis on the chemical level, respectively. Due to the paucity of studies reporting on the effect of different forms of strontium salts to bone mineralisation, we have investigated two different forms of strontium salts (strontium chloride and strontium ranelate) in addition to different doses. As it has been previously suggested that strontium supplementation may influence cellular processes, there we hypothesised that the supplementation of strontium would affect collagen fibril in the chemical level since procollagen molecules are produced by osteoblast cells. Alternatively, the supplementation of strontium may affect the assembly and/or organisation of procollagen into collagen fibril as the addition of strontium may affect its physiochemical environment.

5.2. Methods

5.2.1. Cell Culture

MC3T3-E1 (MC3T3) subclone 4 (mineralising sub-clone) was purchased from ATCC. MC3T3 is a suitable model for an *in vitro* model for osteoblasts development, differentiation, and mineralisation [215, 216, 292]. By using the MC3T3 cell line, the non-homogeneity of primary cell batches can be eliminated and the reproducibility of the experiment is improved. Cells were expanded in tissue culture treated flasks (Corning) in αMEM (without ascorbic acid; GIBCO; A1049001) with 10% (v/v) FBS

(Hyclone FBS; Thermo Scientific) according to ATCC's suggested protocol. The cells were routinely passaged with trypsin-EDTA (Life Technologies) to ~80% confluence.

Mineralisation was achieved by seeding cells at 30,000 cells/cm^2 in αMEM (without ascorbic acid) with 10% (v/v) FBS, 50 µg/mL ascorbic acid (Sigma-Aldrich), and 2 mM ß-glycerophosphate (Sigma-Aldrich). The cultivation of the cells was continued until day 14, unless stated otherwise. The culture media was changed every two days.

5.2.2. Alizarin Red Staining

Alizarin red staining was performed to stain the bone nodule formed on cell culture by staining calcium-rich deposits [293]. On days 14 and 42 when alizarin red staining was performed, the cell monolayer was washed with phosphate-buffered saline (PBS) twice and then fixed with 4% (v/v) paraformaldehyde (Sigma-Aldrich) for 20 minutes before being washed again with PBS twice. The monolayer of cells was incubated in 2% (w/v) Alizarin Red-S (Sigma-Aldrich) solution for one minute. The cell monolayer was then washed with double-distilled water until the rinsing solution was no longer red. All light microscopy images were viewed with an Olympus BX51 microscope equipped with an Olympus DP70 camera.

5.2.3. ICP-OES

ICP-OES measurements were performed to evaluate whether calcium phosphate precipitation occurred as a result of increased media ionic strength when more ions were supplemented. The measurement was also conducted to observe whether there were differences in the strontium ions released from strontium ranelate and strontium chloride salts[3]. Cell-free media samples were incubated in the cell culture incubator at 37°C for three days before being filtered using 0.2 µm membrane filter. If calcium phosphate precipitation occurred, the precipitates were filtered off from the media and the phosphorus levels were lowered. Elemental concentrations (Ca, Sr, P, Mg) in the medium samples were determined by ICP-OES using an iCAP6000 Series ICP spectrometer (Thermo Scientific) using at least three independent samples.

5.2.4. Von Kossa Staining

Von Kossa staining was used as an inexpensive way to visualise mineral deposits in mineralising cultured cells on days 10 and 14 [294]. In summary, silver cations react

---

[3] The amount of strontium ranelate and strontium chloride supplemented to the media was calculated using the total molecular weight of the compound.

with phosphates and carbonates in calcium deposits. The deposits are reduced to a black coloured deposit by light. The cultured cell monolayers were washed with PBS and fixed with 4% (v/v) paraformaldehyde in PBS for 20 minutes. The fixed cells were washed with double-distilled water at least three times before being submerged in 5% (w/v) $AgNO_3$ (Sigma-Aldrich) for 20 minutes in darkness. The cells were washed again with double-distilled water at least three times before being submerged for two minutes in 5 g Na_2CO_3 (Sigma-Aldrich) in 75 mL double-distilled water and 25 mL 4% (v/v) paraformaldehyde (in PBS). The cells were washed again with double-distilled water at least three times. The cells were then submerged for two minutes in 5% (w/v) sodium thiosulfate (Sigma-Aldrich). The cells were washed with double-distilled water for at least three times. Haematoxylin (Sigma-Aldrich) was used to counterstain the cells (two-minute incubation) before the final washes with double-distilled water until no purple colour was seen in the washing water.

5.2.5. Hydroxyproline Quantification

The collagen content of day-14 cell monolayer was estimated by quantifying the hydroxyproline component following an assumption that hydroxyproline makes up 10% of collagen [295]. The monolayer sample was grown in a 6-well plate (Corning) and digested with 300 µL papain digest solution made of 5 mM EDTA (Life Technologies) + 5 mM L-cysteine (Sigma-Aldrich) in double distilled water; pH adjusted to 7.4; 10 µL papain (Sigma-Aldrich) per 5 mL EDTA-L-cysteine solution. The digestion was performed in wax-sealed Eppendorf tubes in 60°C for 48 hours. Papain digested samples were hydrolysed in 6 N HCl (Sigma-Aldrich) at 110°C for 18 hours in a Teflon-sealed glass tube (Thomas Scientific). The hydroxyproline of the hydroxylate was determined by Ehrlich's reagent assay (Chloramine-T; Sigma-Aldrich) that changed colour (at 560 nm) depending on the hydroxyproline concentration [296]. The standard curve was generated with L-hydroxyproline (Sigma-Aldrich).

5.2.6. DNA Assay

A DNA assay was used to quantify DNA amount as a means to normalise the hydroxyproline quantification at day 14 of culture. DNA was quantified using Quant-iT™ PicoGreen® dsDNA Reagent and Kits (Molecular Probes, Invitrogen; P7589). PicoGreen stains nucleic acids and fluoresces (Excitation = 485 nm; Emission = 535 nm; Cut-off = 515 nm). The concentration of DNA was determined from the generated standard curve according to the manufacturer's instructions.

5.2.7. Transmission Electron Microscopy Sample Preparation

TEM was used to view cells and collagen fibrils at a submicron level at day 14 of culture. Hundreds of TEM micrographs were analysed to calculate how the fibrils were aligned and organised. Cultured cells were washed twice with PBS and then fixed in 4% (v/v) glutaraldehyde (Sigma-Aldrich) in 0.1 M PIPES (Electron Microscopy Sciences) buffer (pH 7.2) at 4°C for two hours. After twice washing with 0.1 M PIPES buffer, the fixed samples were post fixed with 1% (w/v) osmium tetroxide (Electron Microscopy Sciences) for one hour at room temperature to provide contrast for TEM observation. Post-fixed samples were washed six times with 0.1 M PIPES (pH 7.2). The samples were dehydrated at room temperature using a graded ethanol series from 50%, 70%, and 90% (2x5 minutes per ethanol concentration), and with 3x10 minutes of 100% ethanol. The samples were immersed in dry acetonitrile (Sigma-Aldrich) for 3x10 minutes at room temperature. The samples were immersed in Quetol-based resin (Electron Microscopy Sciences) at room temperature with increasing resin-to-acetonitrile ratios: 1:1 (for 2 hours), 3:1 (overnight), 100% resin (for two days in atmospheric pressure, and one final day under vacuum condition; resin was changed daily with freshly prepared resin). The resin was polymerised at 60°C for 24 hours.

5.2.8. Ultramicrotomy

70 nm thick sections (silver-gold coloured sections) were cut onto a water bath using ultramicrotome (Leica) with a glass knife or a 45° diamond knife (Diatome). The sections were collected immediately on bare 300 mesh copper TEM grids (Electron Microscopy Sciences) and dried immediately on filter paper. The TEM grids with the sections were put into a ~37°C oven for approximately ten minutes to help smooth the TEM sections adhere to the grid.

5.2.9. Collagen Organisation Image analysis

Analysis of collagen organisation was done by evaluating the fibril organisation using TEM micrographs (JEOL FX2000) of day-14 collagen fibrils. An averaging or median filter (MATLAB) to remove salt-and-pepper background noise was applied to the original TEM micrographs (Figure 5.1). Dark areas or blobs were removed using a multi-scale gradient masks. A Hessian-based Frangi Vesselness filter was used to separate the collagen fibrils from background; this filter produced two images to represent: (1) the presence of collagen; and (2) the orientation vectors of the collagen fibrils. When the image representing the presence of collagen was crossed multiplied with the orientation vectors, the orientation of collagen could be mapped out and the frequency of collagen at different orientation angles was graphed as a histogram. The kurtosis value of the histogram was calculated by MATLAB to indicate how aligned the collagen fibrils were to each other; the more aligned or organised the fibrils are, the steeper the histogram and the higher the kurtosis value.

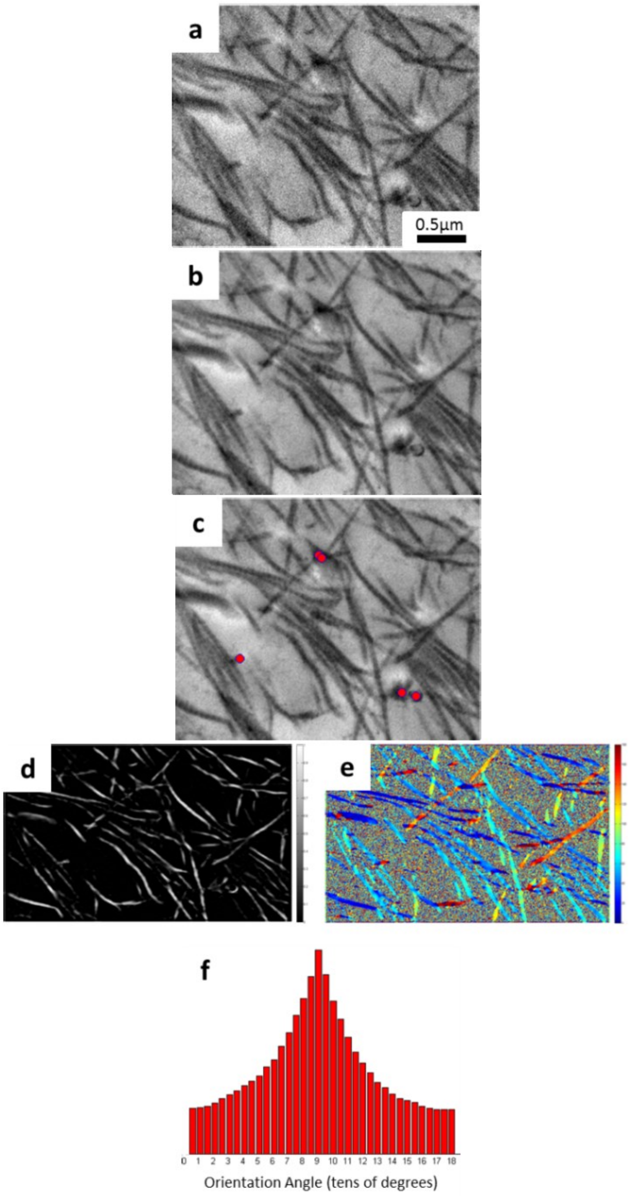

Figure 5.1 Schematic of image analysis done to TEM micrographs to measure the collagen organisation. An averaging or median filter to remove salt-and-pepper background noise was applied to an original bright field TEM micrograph (a) resulting in a smoother image (b). To remove dark areas or patches, a multi-scale gradient masks was used to image (b), which resulted in the identification of non-collagenous regions (c), which were to be unaccounted for in the subsequent analysis. A Hessian-based Frangi Vesselness filter was used to separate the collagen fibrils from the background; this filter produced two images to represent the presence of collagen (d) and the orientation vector of the collagen (e). When image (d) and (e) were crossed multiplied, an analysis of the frequency of the collagen fibrils at different orientation angle could be graphed into a histogram (f). The kurtosis value of (f) was calculated by Matlab to indicate how aligned the collagen fibrils were to each other. Scale bar in (a) applies to (d-e).

5.2.10. Raman Spectroscopy and Spectra Analysis

Raman spectral analysis allowed the analysis of day-14 cell matrix at the chemical level. The Raman spectroscopic imaging system used consisted of a sapphire laser (λ_{ex} = 488 nm, maximum output: 40 mW, Coherent) and a Renishaw RM2000 (Renishaw) dispersive spectrometer equipped with an 1800 groove/mm grating. The spectrometer was connected to an upright Leica microscope with a Renishaw MS20 piezo-electric stage for scanning. Raman signals were collected using a Nikon 60× (NA = 1.0) (Nikon) water immersion objective with 20 mW at the sample. The emission lines of a spectral calibration lamp (Renishaw) were used for wavelength calibration. The system acquires Raman spectra in the spectral range from 800-1800 cm^{-1} with a resolution of ~5 cm^{-1} using the 488 nm laser excitation. The microscope was focused onto the tissue, ensuring maximum Raman signal generation and collection. Hyperspectral Raman images were collected in 45 × 45 pixel rasters using a piezoelectric stage scanning over a 1000 × 1000 µm area to average over the heterogeneities in the tissue construct (e.g. cells, connective tissue).

Since the intensity-calibrated raw Raman spectra represents a superposition of Raman signals and varying degree of autofluorescence background, a fifth-order polynomial constrained to the lower portion of the spectrum (800-1800 cm^{-1}) was fitted to the autofluorescence background in the spectrum. This polynomial was then subtracted from the calibrated spectrum to yield the Raman spectra alone. All spectra were normalised to the integrated area prior to analysis to reduce variation such as caused by laser power and focusing. This enables a comparison of the relative spectral changes in the tissue.

Principal component analysis (PCA) was used to evaluate the spectral difference between samples. Briefly, PCA decomposes the spectra into orthogonal variations called principal components (PCs). Each PC contains a loading corresponding to variations with successive decreasing percentage of influence. The projections of Raman spectra on the loading are termed scores. The number of PCs retained in this study was based on the percentage explained variance. Spectral variations accounting for less than 1% were not considered in this study.

PCA is a common method to analysing Raman spectra, able to provide patterns, groupings, and detection of outliers [297]. PCA is also suitable for the analysis of large datasets, and able to group data points according to their biochemical content and identify spectral features that contain the highest degree of variability in the data set [298, 299]. With the high number of spectra obtained in this study, PCA's ability to simultaneously compare each spectrum makes it appropriate to be used for the current study. PCA requires no *a priori* knowledge of the samples; such a trait is also appropriate to be used in the current application since well-characterised samples are not available to be used as a 'standard' for pattern recognition (i.e. *a priori* knowledge of each sample) for each Raman spectrum from each treatment to be compared to [297].

5.2.11. Authors' Declaration

Kharissa Nitiputri designed and planned the studies, conducted all the cell culture experiments, and prepared cell cultures for Raman spectroscopy and TEM imaging. Kharissa Nitiputri also performed the hydroxyproline quantification, alizarin red staining, light microscopy and TEM imaging. The Raman acquisition was mostly done by Charalambos Kallepitis and Mads Bergholt, with assistance from Kharissa Nitiputri. TEM image analysis was done by Lucas Hadjilucas. Kharissa Nitiputri interpreted the data and wrote the chapter.

5.3. Result

5.3.1. Experimental Design Optimisation

The supplementation of 10 mM ßGP to induce mineralisation in osteoblast cultures has widespread use [3, 300-302]. However, it has been questioned if such an excess of phosphate can result in dystrophic precipitation [300, 303]. Some studies supplemented 5 mM ßGP to their culture system [302, 304-306]. Therefore, a preliminary experiment was performed to evaluate the ability of MC3T3 to mineralise with ßGP supplementation less than 5 mM in culture conditions. We experimented with a 'conservative' ßGP supplementation of 2 mM as Chung *et al.* indicated that medium supplementation with ßGP above 2 mM would lead to non-physiological mineral deposition in the bone cell culture [300]. Hence, a preliminary experiment with 0 mM, 2 mM, and 10 mM of ßGP was conducted.

Observation with light microscopy showed some mineral deposition that started as early as 10 days for groups that was supplemented with 2 mM ßGP (Figure 5.2b). This was verified by Von Kossa staining (Figure 5.2e). At day 14, the 10 mM ßGP culture was mineralising while the no-ßGP cultures were not mineralising, which was as expected. Visual inspection showed that 2 mM ßGP supplemented culture produced more mineral compared to 10 mM ßGP groups. TEM observation of 2 mM ßGP supplemented culture at day 14 also showed normal matrix mineralisation (Figure 5.3). With these observations, the following experiments were conducted using 2 mM ßGP supplementation.

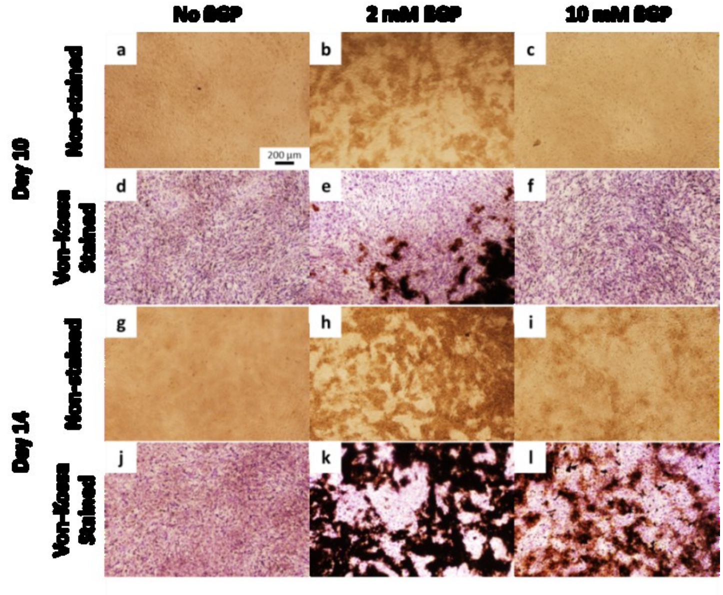

Figure 5.2 Bright field light microscopy observation of MC3T3 grown on tissue culture plastic for days 10 and 14 showing representative images from an experiment to verify the ability of osteoblast cell cultures supplemented with different amounts of ßGP in the osteogenic (i.e. mineralising) medium to mineralise. Mineralisation is marked by the formation of dark areas (a, b, c, g, h, i) (bone nodules) that visually become more prominent after Von Kossa staining (d, e, f, j, k, l).

After the osteogenic medium supplementation was selected, strontium supplementation experiments were conducted to choose the appropriate dosage of strontium chloride. Originally, three groups were chosen (Table 3): control (Ost), 1 mM $SrCl_2$ (1Sr), and 3 mM $SrCl_2$ (3Sr). Supplementation of 1Sr was chosen based on the commonly used strontium concentration for cell culture [154, 155, 188]. This concentration was also previously found to be the concentration of strontium ion contributed by our strontium-containing bioactive glass to its conditioned media [205]. The supplementation of 3 mM $SrCl_2$ (3Sr) was chosen as many studies have conflicting reports as to its effect; higher strontium concentration might increase the strontium's desirable benefits [188], while other studies have reported that higher strontium supplementation adversely affects bone [291].

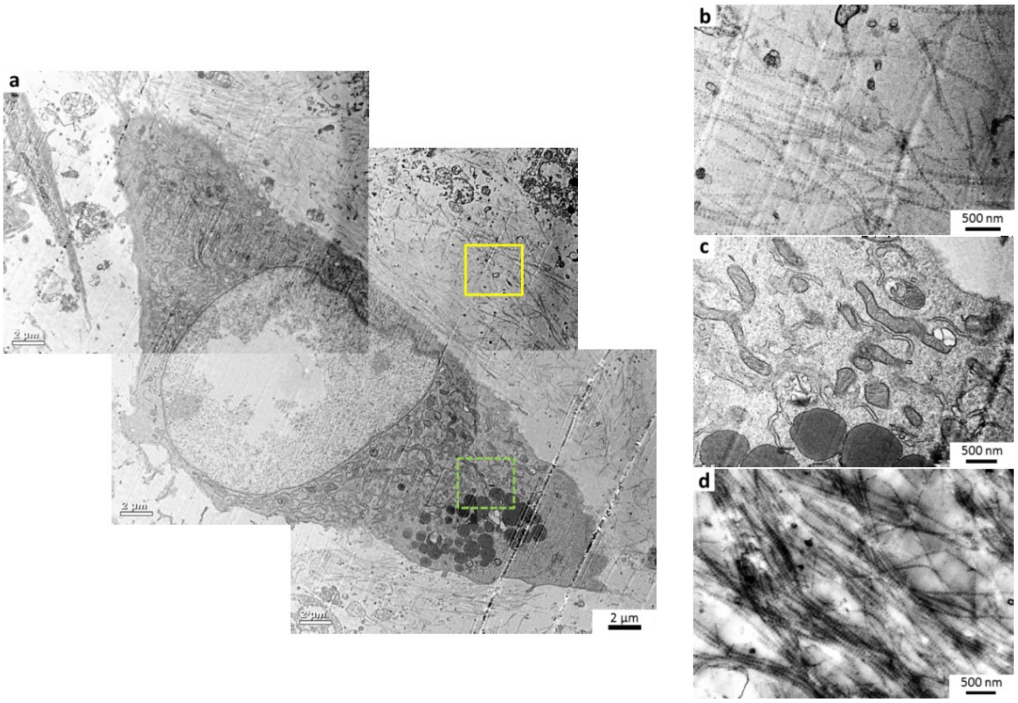

Figure 5.3 Bright field TEM micrographs of MC3T3 cultured in osteogenic medium supplemented by 2 mM ßGP at day 14 prepared by chemical fixation. Collage of an MC3T3 cell surrounded by collagen fibrils (a). A higher magnification image of the solid-yellow box in (a), showing the collagen fibrils (b). A higher magnification of the dashed-green box in (a) showing healthy cell organelles (mitochondria and vesicular structures) (c). A higher magnification of mineralised collagen, showing banding pattern (d).

Table 3 Various cell culture media used in this study.

Cell Culture Media	Explanation
Growth Media	αMEM + 10% (v/v) FBS
Mineralising or Osteogenic Media (Ost; Control)	Growth Media + 2 mM ßGP + 50 mg/mL L-ascorbic Acid
0.1Sr (or 0.1SrRan)	Ost + 0.1 mM $SrCl_2$ (or Sr-Ranelate)
1Sr	Ost + 1 mM $SrCl_2$
3Sr	Ost + 3 mM $SrCl_2$

The first set of experiments showed that only the Ost group showed macroscopic matrix mineralisation as early as day 14, whilst 1Sr and 3Sr groups failed to show macroscopic matrix mineralisation as late as day 42 (Figure 5.4). Based on this finding, another group having a $SrCl_2$ concentration lower than 1 mM was included in the study. 0.1 mM strontium supplementation (0.1Sr) was chosen based on the 0.12 mM strontium serum concentration of osteoporotic patients treated with 2 g/day strontium ranelate [146]. 0.1 mM of strontium ranelate (0.1SrRan) was also included in the study to provide comparison to the 0.1Sr group.

At day 42 of culture, Alizarin Red staining of the MC3T3 culture was done to show nodule calcification [293]. The 0.1Sr and 0.1SrRan groups showed macroscopic matrix mineralisation comparable to the control group starting at day 14. Nodules were formed in the 1Sr and 3Sr groups (darker regions in Figure 5.4h and i), however they did not stain red, indicating that they failed to mineralised (Figure 5.4m and n). When compared to cultures treated with the same amounts of supplemented calcium (Figure 5.4p, q, r), mineralisation was observed as early as day 14. Calcium supplementation also seemed to increase the mineralised area. This effect on mineralisation may be the result of a higher calcium presence that provided more calcium more readily during mineralisation. This result meant that 1 and 3 mM strontium supplementation specifically altered mineralisation of the culture and may have meant that the cells produced collagen fibrils to form nodules. However, fibril mineralisation seemed to be altered, preventing the growth of the mineral. This experiment revealed that there was an optimum strontium concentration that resulted in normal macroscopic matrix mineralisation.

Christoffersen *et al.* studied the effects of strontium ions on growth of synthetic hydroxyapatite [206], and showed that increasing strontium ion concentration increased the inhibition of apatite deposition. A study by Fujino also showed through X-ray diffraction pattern that calcium-strontium apatite has lower crystallinity than pure calcium apatite has, and this trend becomes more obvious as strontium substitution get higher, and that calcium-strontium apatite may crystallise more slowly than pure calcium apatite [307]. Verberckmoes *et al*. later showed that highly strontium substituted synthetic hydroxyapatite (12.7-60% Sr/[Sr+Ca]) to have higher solubility than non-strontium substituted hydroxyapatite [207]. Combined together, these studies suggested that the substitution of calcium in hydroxyapatite by strontium caused the expansion of hydroxyapatite crystal lattice to accommodate strontium's larger atomic radius (than that of calcium's). In turn, this increased the inhibition of and slowed down crystal formation, as well as lowers the crystallinity and increase the solubility of the strontium-doped hydroxyapatite [207]. With these studies, it is plausible to conclude that the non-mineralisation observed at high strontium supplementations in the current study was due to the physiochemical effect of strontium ions: strontium inhibited and slowed down the crystallisation of *in* *vitro* mineral, and strontium also increased the solubility of mineral or mineral precursor that might had formed.

ICP-OES measurement conducted on media incubated (in cell culture incubator) for three days showed there was no precipitation of calcium phosphate as the phosphate levels between Ost and media supplemented by other ions did not show statistically significant difference. This measurement was an important check especially for cultures supplemented with more calcium. Since precipitation was not detected by ICP-OES, mineralisation in calcium supplemented cultures was not the result of spontaneous precipitation of calcium and phosphate in the media; instead, it was the result of normal mineralisation. The ICP-OES also showed the statistical insignificance of the [Sr] between 0.1Sr and 0.1SrRan, showing that both the chloride and ranelate forms of strontium provided the same amount of strontium ions in the cell media (Figure 5.5). This measurement was necessary since even though company product information (Sigma-Aldrich) showed that strontium ranelate was soluble up to 1 mg/mL (1.95 mM of strontium ranelate) in warmed H_2O, the cell culture environment contained various ions and proteins (from serum) that made the solubility of strontium ranelate lower.

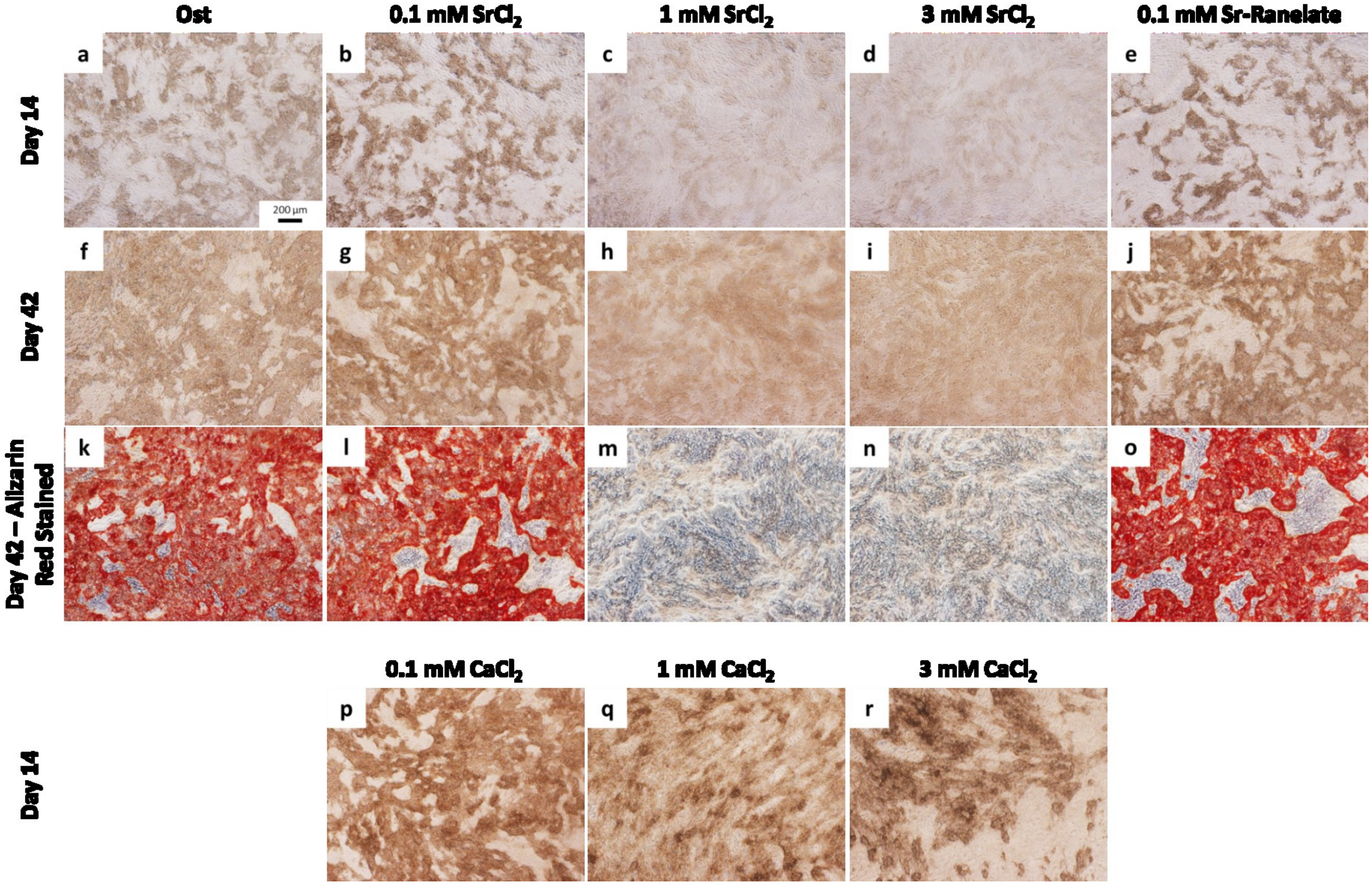

Figure 5.4 Light microscopy of MC3T3 grown on tissue culture plastic for 14 and 42 days with $SrCl_2$, $CaCl_2$, or strontium ranelate supplements. Bright field imaging showed the extent of macroscopic matrix mineralisation (a-j, p-r). Alizarin red staining was used to show the presence of calcium ions (k-o). Scale bar in (a) applies to all images.

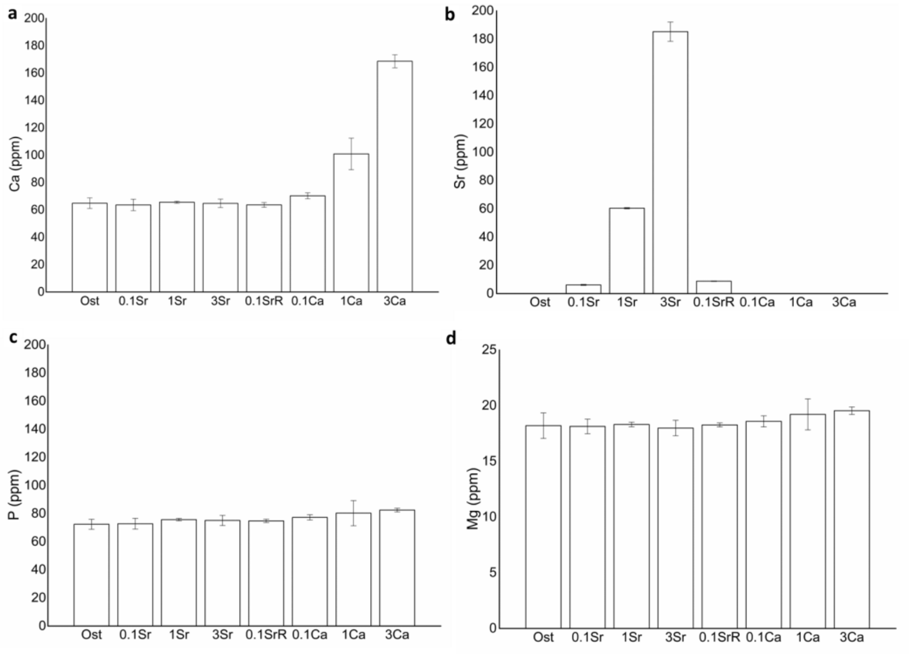

Figure 5.5 Concentration of various ions in the cell culture media measured by ICP-OES. No statistical differences in the [Ca] between Ost and 0.1Ca was observed (a). No statistical differences in the [Sr] between 0.1Sr and 0.1SrRan was observed (b). No statistical differences in the [P] and [Mg] between all groups (c, d). Error bar shows standard deviation; *n*=3.

5.3.2. TEM Observation of Collagen and Collagen Alignment Quantification

TEM was conducted to observe the collagen fibril mineralisation and fibril organisation (Figure 5.6). MC3T3 cells were grown for 14 days in osteogenic media with, or without, the addition of strontium ions. The TEM sample preparation route chosen allowed the preservation of organic materials such as cell membrane and collagen fibrils. The mineral component of the culture was not analysed as the aqueous sample preservation would alter the original mineral crystallinity. The 65 nm periodic banding pattern of the collagen fibrils was observed in all treatments (Figure 5.6f, g, h, i, and j). However, as observed by low-magnification light microscope in Figure 5.4, high-magnification TEM imaging showed that collagen fibril mineralisation was observed only in the Ost, 0.1Sr, and 0.1SrRan (Figure 5.6a, b, e, respectively)[4]. Small circular dark structures of 50 nm in diameter were observed around the collagen fibrils of the 3Sr groups only (Figure 5.7). These dark structures appeared similar to matrix vesicles, which are hypothesised to be involved in the progression of collagen fibril mineralisation.

---

[4] Figures f, g, j in Figure 5.6 were produced in areas where fibril mineralisation was not captured in the field of view. This was done so that the low-contrasted collagen banding became more visible due to the inexistence of high contrast minerals in the field of view (e.g. in Figure 5.6a, b, e).

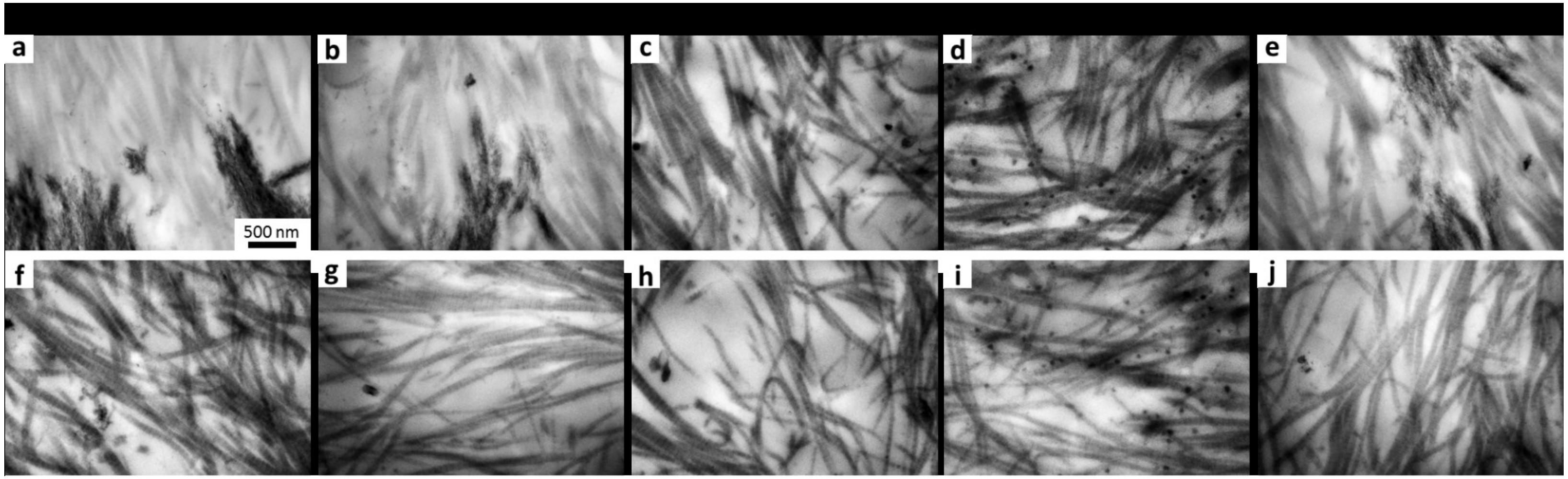

Figure 5.6 Bright field TEM images of day 14 collagen of MC3T3 cultured in various conditions prepared using chemical fixation. Mineral deposit was seen in Ost, 0.1Sr, and 0.1SrRan, but not in the 1Sr and 3Sr cultures as the dark regions on the collagen fibril in figures a, b, e. Figures f, g, and j shows the predominantly unmineralised collagen in Ost, 0.1Sr and 3Sr groups, respectively, and presented to clearly show the banding of the collagen. Circular dark structures were seen interspersed around the collagen fibril of the 3Sr group (d, i).

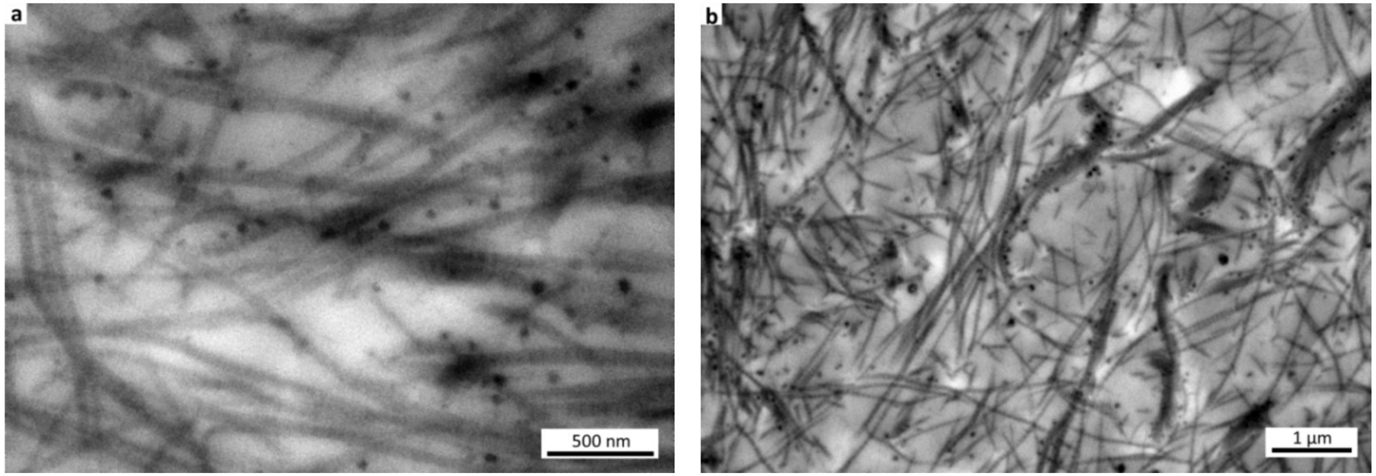

Figure 5.7 Bright field TEM micrographs of MC3T3 cultured in 3Sr condition at day 14 and prepared by chemical fixation showing collagen fibrils and matrix vesicle-like entities. A higher magnification image showed that the matrix vesicle-like entities were around 50 nm in diameter (a), and a lower magnification image showed the localisation of matrix vesicle-like entities around the collagen fibrils (b).

Further study of how strontium may affect collagen fibril was performed as extensive studies on collagen have not yet been reported. In this study, we looked into the organisation of collagen by quantifying the relative organisation of collagen fibrils to each other. Using hundreds of TEM micrographs of collagen fibrils at randomised areas, image analysis measured the frequency of collagen fibrils in each image according to their directionality. The kurtosis (i.e. a measure of spread of the frequency or how steep a curve is) of the frequency histograms became a measure of how aligned the fibrils are to one another (i.e. the more aligned the fibrils were, the steeper the histogram and the higher the kurtosis value).

Figure 5.8 plots the kurtosis values obtained from individual TEM micrograph and groups them according to treatment. Routine statistical analyses are represented by the corresponding box plots. The combined figure (Figure 5.8d) shows that the groups treated with the higher strontium supplementation (1Sr and 3Sr) resulted in lower kurtosis value (i.e. less alignment of collagen fibrils), while 0.1Sr and 0.1SrRan behaved closer to the control group. When statistical analysis was calculated using each of the kurtosis values as individual n, no significant difference was achieved between the 0.1Sr and 0.1SrRan, while both of these groups have statistically higher kurtosis values with respect to the control group (Bonferroni analysis; p<0.05). Using the same method, 3Sr has statistically lower kurtosis values than the rest of the groups. Nevertheless, when statistical analysis was calculated using the average of each repeat as the n, no statistical significance was attained. Visually, it can be observed that higher concentrations of strontium supplementation at 1 and 3 mM tend to shift the organisation of the collagen fibrils towards more randomly organised fibrils. The groups treated with 0.1 mM of strontium chloride and strontium ranelate appeared to shift the organisation of the fibrils towards a less random organisation, or the same arrangement, as the control group.

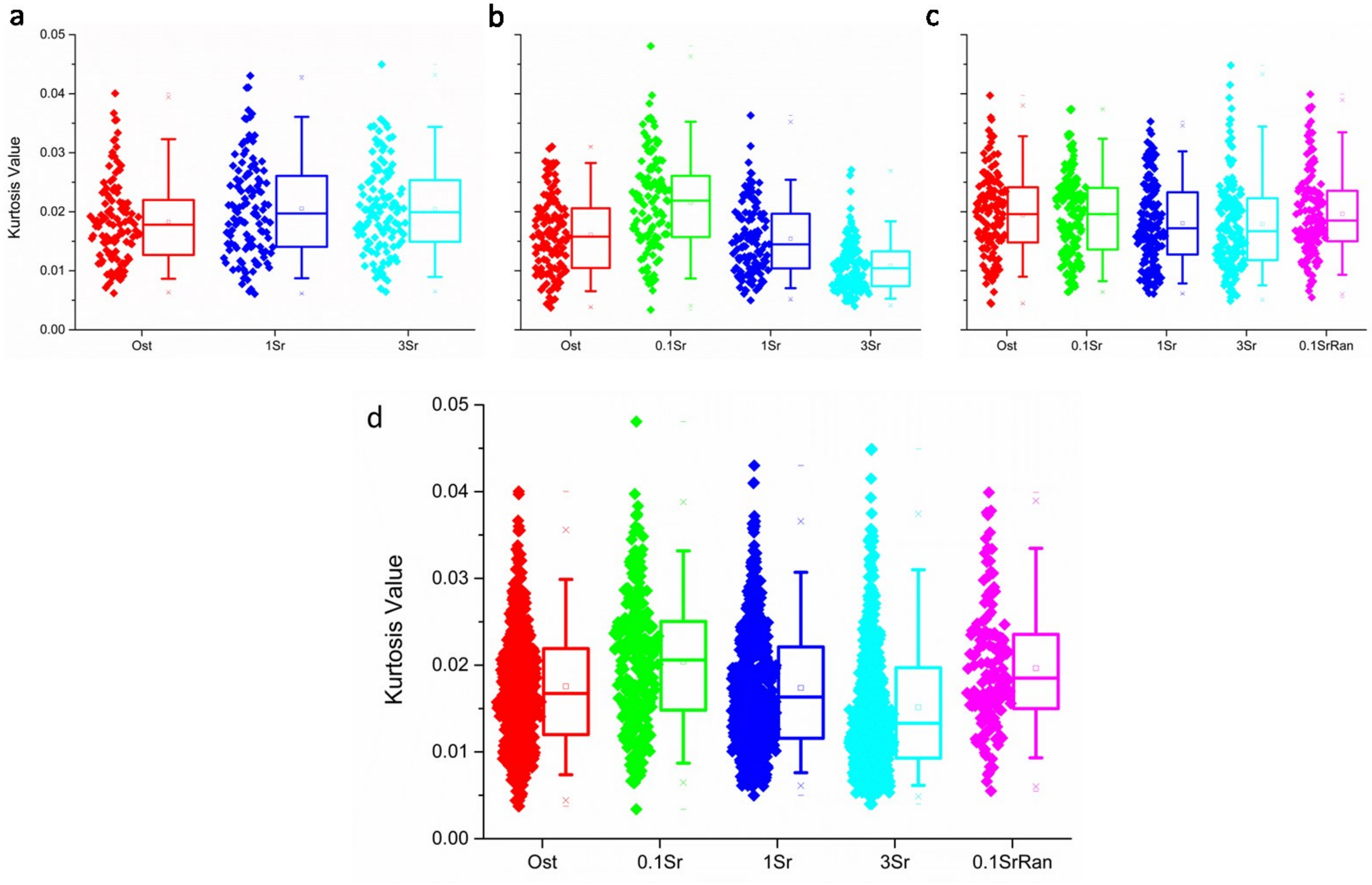

Figure 5.8 Frequency histogram kurtosis values of collagen fibril organisation of MC3T3 at day 14 cultured with various strontium supplementation. Each dot represents a kurtosis value of collagen fibril organisation frequency within a TEM micrograph. Three batches of experiments (a, b, and c) were conducted, each with the addition of new treatment group. A combined graph (d) shows a similar trend of the each individual batch. The final graph shows 3 independent replicates for Ost, 1Sr and 3Sr groups, and 2 independent replicates for 0.1Sr and 1 replicate for 0.1SrRan. The box plots represent the 5th to 95th percentiles. The whiskers denote the maximum and minimum values. The horizontal line across the box plot denotes the median value.

5.3.3. Raman Spectral Analysis

Raman spectra were acquired from day 14 culture to evaluate chemical differences between matrices produced as a result of the various treatments (Figure 5.9a). The mean spectra were largely attributed to the collagen signature (Figure 5.9b), while cell components (such as cytoplasm, lipid, and DNA) were minor contributors to the spectra. The most intense Raman peaks are listed in Table 4. Apatite mineral signature at 960 cm^{-1} was not observed owing to technical difficulties with the cell culture. This lack of mineral peak might be advantageous as differences in the matrix are of greater interest than the differences in the mineral component. However, great care was ensured in the interpretation of this Raman data when done together with other analyses using different techniques (e.g. biochemical techniques, TEM).

Table 4 Most intense Raman peaks and their peak assignments

Raman Spectra (cm^{-1})	Peak Assignment [3, 308-310]
853	Proline and hydroxyproline
936	C-C
1004	v_s(C-C) ring breathing of phenylalanine
1265	amide III v(C-N) and δ(N-H) of collagen
1445	δ(CH2) deformation of collagen
1655	amide I v(C=O) of collagen

To reveal the differences between the groups, subtractions between the spectra of each group were performed (Figure 5.9c, d, e). The differences between the spectra (±1 standard deviation) showed subtle differences between tissues. Generally, differences were more apparent between strontium supplemented groups and the control group; some differences were also seen between 0.1Sr and the rest of the strontium-treated groups (i.e. 1Sr, 3Sr, and 0.1SrRan). Minimal differences were seen between the 1Sr, 3Sr, and 0.1SrRan groups, which suggested that 0.1 mM strontium ranelate supplementation acted similarly to the 1 and 3 mM strontium chloride supplemented groups than to the 0.1 mM strontium chloride group. A more thorough analysis on the Raman regions contributing to the differences will be discussed in conjunction with principal component analysis in the following paragraphs.

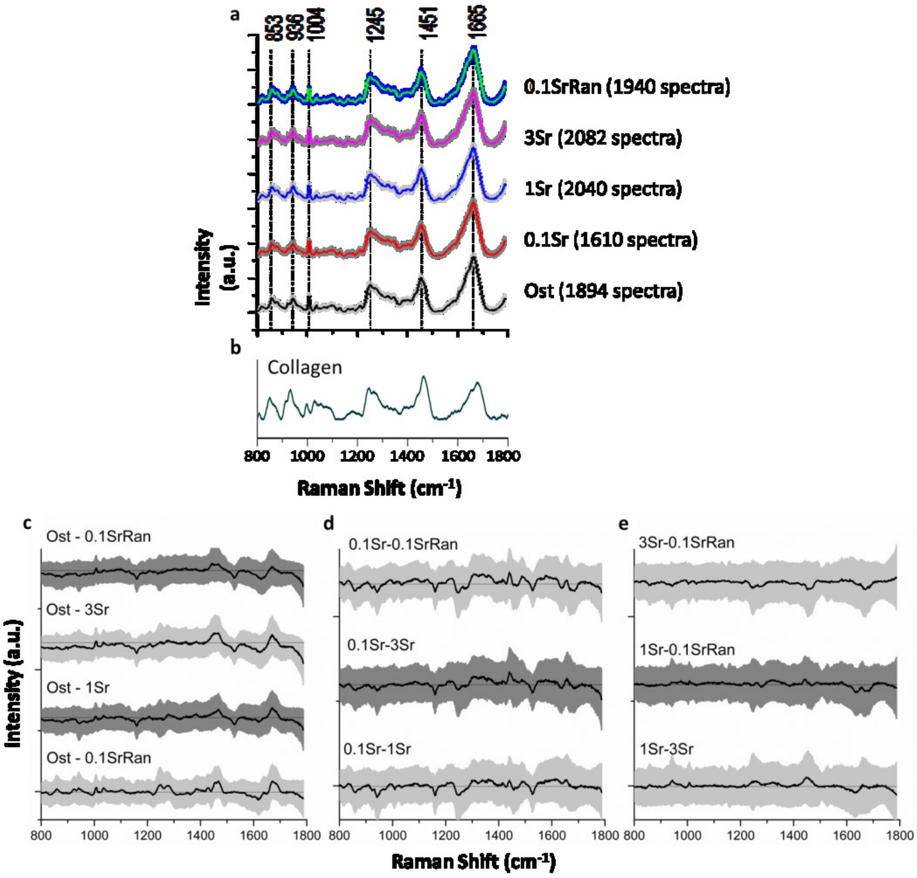

Figure 5.9 Raman spectra of the MC3T3 cell and matrix of various strontium supplementations and control group at day 14 (a). Raman spectrum of collagen type I reference spectra (b) adapted from [311]. Subtractions between the spectra of each group were performed to reveal subtle differences (c, d, e). The mean of each subtraction is shown by solid black line, and ±1 standard deviation is shown by the grey regions around the mean.

Principal component analysis (PCA) was used to further reveal the chemical differences between the groups that may not be picked up by simply subtracting the spectra between the treatments.[5] The loading of the two most important principal components (PCs) was plotted against the Raman shift in the x-axis (Figure 5.10k) to show which Raman regions contribute to meaningful differences between treatments. The Raman regions with more positive or negative loading values in Figure 5.10k represent more meaningful differences between treatments. Figure 5.10k used together with the scatter plot of PC1 scores versus PC2 scores (Figure 5.10a-j) determines the differences between treatments.[6]

---

[5] When subtracting the original spectra successfully shows differences between treatments, the PCA analysis may not necessarily add further information as only the first and second principal components (i.e. 7.6% and 4.3% of the whole component, respectively) are involved in the analysis.

[6] PC loadings (Figure 5.10k) greater than zero correspond to positive correlation between the relative positions of crosshairs between treatments (Figure 5.10a-j); while PC loadings that are less than zero correspond to a negative correlation between the relative positions of crosshairs between treatment.

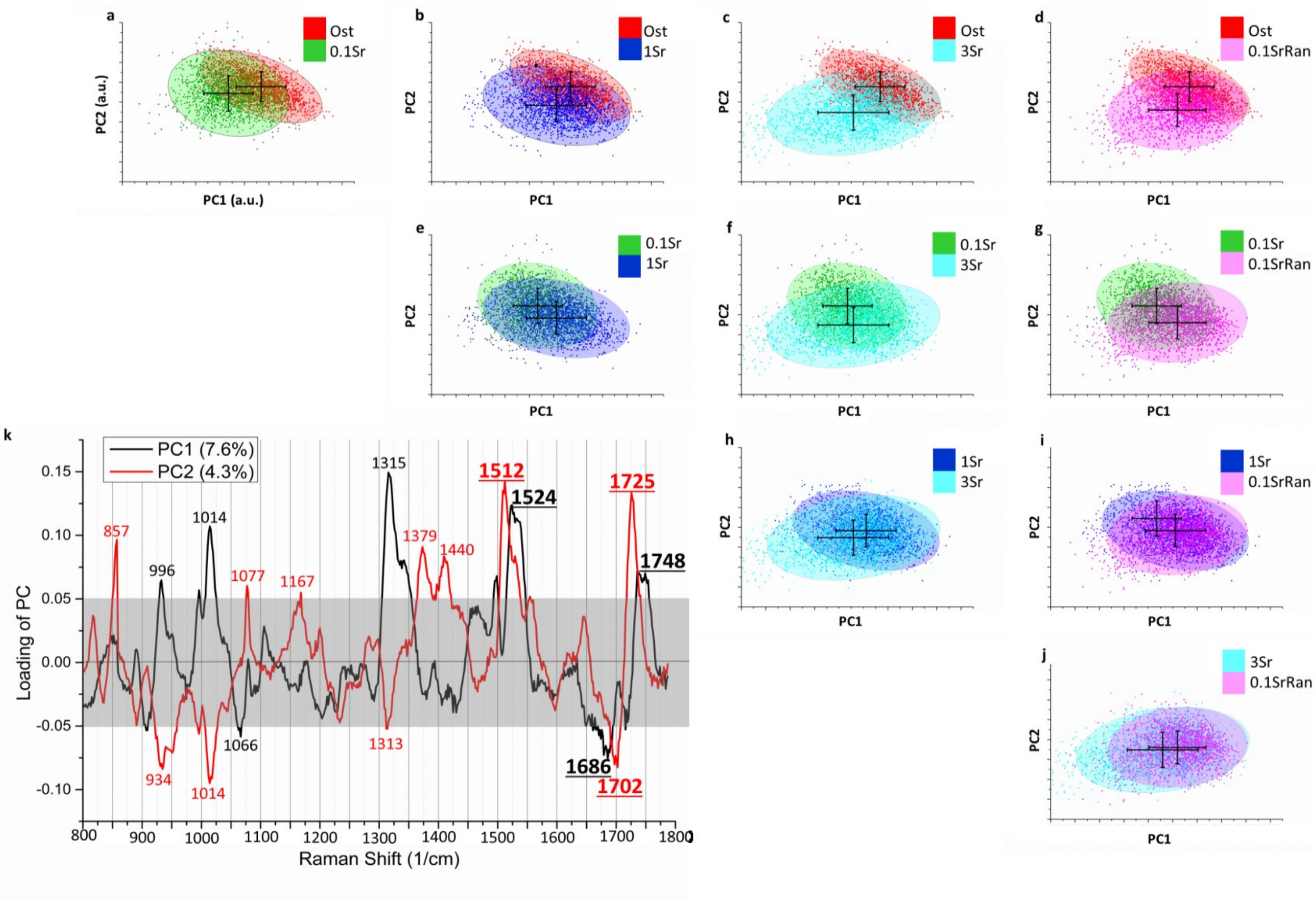

Figure 5.10 Principal component analysis of the Raman spectra acquired from MC3T3 cultured for 14 days in media containing various strontium supplementation. The highest principal components (namely, PC1 and PC2) between two groups are plotted against each other. Confidence ellipses for each group showed 95% confidence level, and the crosshairs represent the averages of PC1 and PC2 scores with their respective ±1 standard deviation. The loadings of the PC1 and PC2 are plotted against the Raman shift (k) showing various Raman regions contributing to the difference between the treatments; the peaks beyond the shaded area will be analysed as they contributed to more meaningful differences between the treatments. The bolded and underlined peak assignments represents the peaks having both PC1 and PC2 beyond the shaded areas, with both of their values either greater or less than ±0.05. Figures a-j are graphed with same *x*-axis range and *y*-axis range.

The distance between the crosshairs between the groups (Figure 5.10a-j) reflects the similarity or difference (i.e. how close or far apart the crosshairs are, respectively) between the two groups. As with the earlier observation established using the subtraction of Raman spectra between two groups, Ost is the most different out of all groups, which may be interpreted that strontium supplementation affects the chemical characteristics of the culture (further explained in the following subsections on Lipid (C=O and C=C) and Protein (Amide I) characteristics). Furthermore, the 0.1Sr group is more similar to the strontium-free control group than the 0.1SrRan group, and the 0.1SrRan group is more similar to the higher strontium supplemented groups (1Sr and 3Sr groups).

Given that the differences between the treatments are subtle, great care was applied in the analysis of Figure 5.10. The analysis will focus on the Raman regions having both PC1 and PC2 loadings that are either greater than 0.05 or less than -0.05 (i.e. beyond the shaded region in Figure 5.10k; greater than +0.05 or less than -0.05) to give more certainty to the interpretation, i.e. the Raman regions discussed in the following analysis corresponded to the regions having differences observed (by subtraction between Raman signal between two groups), as well as having both PC1 and PC2 loadings to be greater than 0.05 or lower than -0.05 (i.e. [PC1 and PC2 ≤ -0.05] *or* [PC1 and PC2 ≥ 0.05]).

5.3.3.1. *Lipid Signature*

5.3.3.1.1. C=O (regions above 1710 cm^{-1})

The Raman region above 1710 cm^{-1} has previously been identified as the lipid signature (i.e. ν(C=O)) [205, 312]. When subtractions were performed between the treatments (Figure 5.9c), clear differences could not be observed. However, as PCA was employed, it was observed that the loadings of PC1 and PC2 showed values greater than 0.05 (Figure 5.10k), which indicated that even though the difference is small, it was meaningful. In particular, the region at 1725 cm^{-1} was of interest since the loading of PC2 was much greater than zero at that region. The clearest difference was seen when the average spectra from the strontium groups were subtracted from the spectra of the strontium-free control (Ost) (Figure 5.11). Here, 0.1Sr had the closest lipid detection to Ost, as the subtraction between Ost and 0.1Sr produced values closest to zero. 1Sr and 0.1SrRan had similar lipid detection as they each produced similar values when each of them was subtracted from Ost. 0.1SrRan and

1Sr had slightly higher lipid detection than Ost and 0.1Sr. 3Sr has the highest lipid intensity of all since the subtraction of 3Sr spectra from Ost produced the most negative value. In summary, Ost and 0.1Sr had the least lipid, followed by 1Sr and 0.1SrRan at similar amounts. 3Sr was shown to have the highest lipid content.

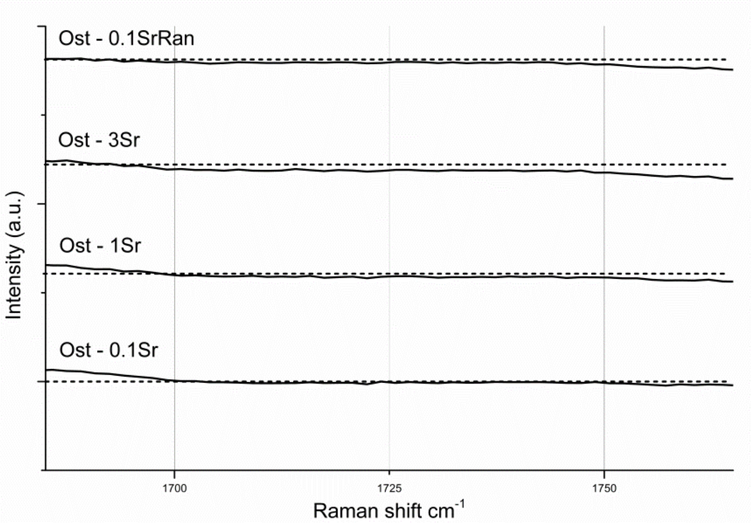

Figure 5.11 Differences between averaged Raman spectra of day-14 MC3T3 grown in strontium supplemented groups and strontium-free control group at the spectral region of lipid, especially at 1725 cm^{-1}. The resulting spectra of each subtractions were shifted along the *y*-axis for clarity; the dashed horizontal lines corresponded to the *y*=0 for each subtractions.

5.3.3.1.2. C=C (regions around 1500 – 1550 cm^{-1})

The Raman region above 1500 – 1550 cm^{-1} has previously been identified as C=C signature (v(C=C)) [313, 314]. While some studies on plant products view that signal in this region as contributed by carotenoids [314, 315], the signal seen in our mammalian cell culture system was probably due to the presence of lipid moieties. When subtractions between the treatments (Figure 5.9c and Figure 5.12) were performed, strontium-free control had a similar C=C level to 0.1Sr. The rest of the strontium treated groups had similar levels but higher C=C detection compared to that of Ost and 0.1Sr. At 1525 cm^{-1}, PC loadings showed values greater than zero, further suggesting that the differences in C=C region seen by the subtraction method were important differences as they contributed to the differences in the two most important principal components. In summary, from the region between 1500 to 1550 cm^{-1}, Ost and 0.1Sr had the same lipid detection, followed by 1Sr, 3Sr, and 0.1SrRan at similar levels.

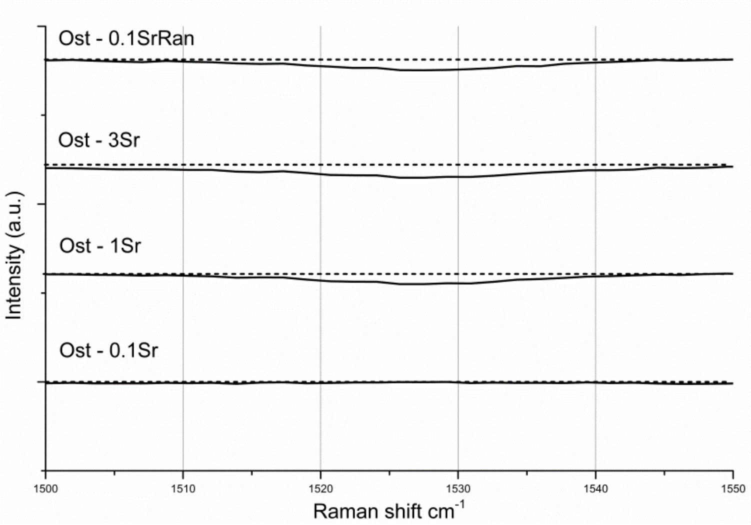

Figure 5.12 Differences between averaged Raman spectra of day-14 MC3T3 grown in strontium supplemented groups and strontium-free control group at the Raman region corresponding to C=C. The resulting spectra of each subtractions were shifted along the *y*-axis for clarity; the dashed horizontal lines corresponded to the *y*=0 for each subtractions.

5.3.3.2. Protein Signatures

5.3.3.2.1. Amide I Signature (regions around 1660 – 1690 cm^{-1})

The Raman region around 1660 – 1690 cm^{-1} has previously been identified as the amide I signature of collagen, or protein molecular vibration [3, 308, 309, 316, 317]. When subtractions were done between the spectra of the various treatments, it was observed that strontium supplementation decreased the detection of amide I in a concentration-independent fashion, i.e. amide I detection was the highest at strontium-free control group, followed by 0.1SrRan, 3Sr, 1Sr, and 0.1Sr. When PCA was employed, both PC1 and PC2 loadings showed values that were less than -0.05 (in Figure 5.10k), further suggesting that the differences in amide I seen by the subtraction method were meaningful as they were able to contribute to the differences in the two most important principal components.

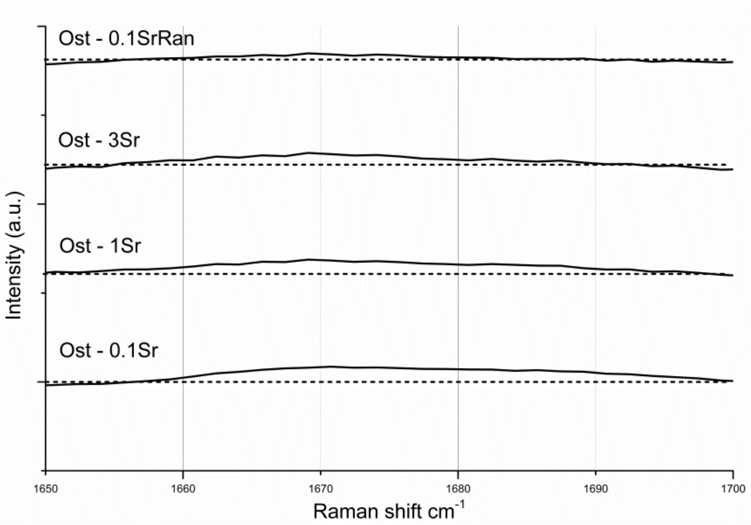

Figure 5.13 Differences between averaged Raman spectra of day-14 MC3T3 grown in strontium supplemented groups and strontium-free control group at the Raman region of amide I. The resulting spectra of each subtractions were shifted along the *y*-axis for clarity; the dashed horizontal lines corresponded to the *y*=0 for each subtractions.

5.3.4. Hydroxyproline Quantification

Hydroxyproline quantification was used to verify the relative amount of collagen (as amide I) detected by Raman spectroscopy. Hydroxyproline has been assumed to be proportionally related to the amount of collagen [296, 318]. Hydroxyproline quantification showed that there were no statistical significance found between the strontium treated groups and controls at day 14 (Figure 5.14). However, from the combined values of the three repeats, it showed that strontium supplementation upwards to 1 mM increased hydroxyproline amount, while supplementation at 3 mM adversely impacted the hydroxyproline amount. It was also observed that 0.1SrRan behaved more like that of 3Sr than that of 0.1Sr or 0.1SrRan.

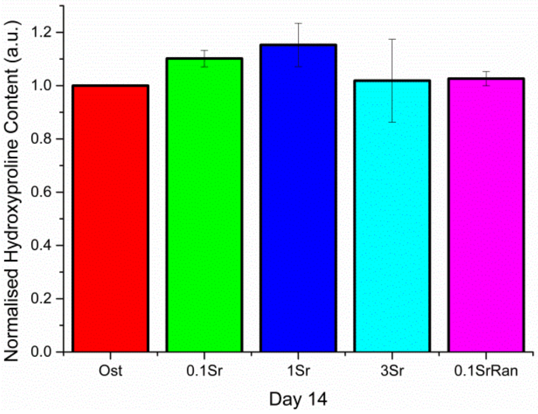

Figure 5.14 Hydroxyproline quantification of day 14 MC3T3 grown in various concentrations of strontium ions. All values were normalised to Ost value. No statistical difference was found between all groups (*n*=3).

5.4. Discussion

Strontium ranelate has long been used as a treatment for osteoporosis [144, 146-148, 155, 172, 187, 190, 192, 193, 319, 320]. But despite nearly thirty years of research, questions remain. For instance, even though the effect of strontium ions on the mineral component of bone has been explored [150, 151, 181, 182], strontium's effect or mode of action on the matrix component of bone is minimally studied. In our study, we attempt to look closely into the effect of strontium supplementation on the non-mineral part of bone mineralisation. As our work examined the effect of strontium supplementation, an *in vitro* osteoblast cell-line culture was chosen as the mineralisation model to simplify the otherwise complicated *in vivo* animal model.

Preliminary studies determined the appropriate media supplementation and strontium concentrations used. The strontium-free control media was effective in allowing normal mineralisation. Some groups were treated with 0.1 mM of strontium chloride or ranelate, which is a relevant concentration also found in the serum of osteoporotic patients treated with strontium ranelate [146]. Some groups were treated with higher strontium supplementation [154, 201, 321] in order to test the effect of higher strontium supplementation to bone matrix.

5.4.1. Low Strontium Supplementation Allowed Normal Mineralisation, while High Strontium Supplementation Altered Mineralisation

Mineralisation of the culture was confirmed as early as day 14 for the control group and those supplemented with 0.1 mM strontium chloride or ranelate. As the culture time was prolonged until the 42nd day, mineralisation in the groups supplemented with 1 and 3 mM strontium chloride was confirmed to be impaired. It also appeared as if these groups supplemented with 1 and 3 mM strontium chloride produced nodules and yet failed to further mineralise. This may suggest that the alteration of mineralisation occurred at the stage of mineral deposition and/or growth and not at during collagen production.

A variety of observations have previously reported on the effect of strontium on mineralisation. Barbara *et al*. showed that continuous supplementation of up to 1 mM of strontium ranelate to MC3T3 did not significantly affect the surface of mineralised nodules at day 14 [154]. Even though our mineralisation observation contradicted this study, others have reported results similar to ours. Wornham *et al*.

showed that strontium ranelate or strontium chloride supplementation inhibited mineralisation of cultured primary rat calvarial osteoblasts at day 14 [201]. Supplementation as low as 0.01 mM showed mineralisation reduction to 59%, while 0.1 and 1 mM supplementation corresponded to 98 and 100% inhibition, respectively.

Using a similar strontium supplementation to the current study, Verberckmoes *et al*. showed that primary rat osteoblast cultures supplemented with 20 and 100 µg/mL strontium ranelate (equivalent to 0.228 and 1.141 mM, respectively) produced a significant reduction in the total area of mineralised nodules compared to a strontium-free control [321]. Instead of a linear trend, this study highlighted the multiphasic effect of strontium supplementation as cultures supplemented with intermediate concentration of strontium (2 and 5 µg/mL or 0.023 and 0.057 mM, respectively) showed no statistical difference in the total area of unmineralised and mineralised nodule; a low concentration of strontium supplementation significantly reduced the combined area of unmineralised and mineralised nodule compared to control.

In light of the variety of observations on the effect of strontium in enhancing, altering, or diminishing *in vitro* mineralisation, it is crucial to note that the differences here may be the result of multiple factors. With regards to the *in vitro* model, the cell type and the passage number should be considered (Figure A.1). The culture conditions such as the type of media used, the concentration of mineral-inducing media supplements (e.g. ascorbic acid, ß-glycerophosphate, steroids and antibiotics), and the frequency of media changes could affect the mineralisation result. However, perhaps the most important factor is the serum supplementation as batch-per-batch differences between sera are indisputable.

5.4.2. High Strontium Supplementation may Alter Mineralisation by Inhibiting the Degradation Rate of Matrix Vesicle-like Entities

In this study, we also used TEM to study the morphology of the collagen fibrils. Periodic banding pattern of the collagen was observed at day 14 in all groups, indicating normal collagen fibrils. Collagen fibril mineralisation was seen in the Ost, 0.1Sr, and 0.1SrRan groups, where mineralisation was observed with the naked eye and through the use of a low-magnification light microscope. The collagen fibrils of the groups supplemented with 1 and 3 mM strontium did not show fibril mineralisation, which confirmed the failure of observed mineralisation by low-magnification methods. Interestingly, circular, electron-dense entities were observed around the collagen of the group supplemented by 3 mM strontium.

An earlier study by Reinholt *et al*. observed the cartilage growth-plate in strontium-induced rickets in a rat model [322]. Using a quantitative stereological approach, they found that the volume fraction of the calcifying zone of the growth-plate in the rachitic rats was lacking compared to the small calcifying zone of the control rats. In addition, Reinholt *et al*. found a comparatively high matrix vesicle volume fraction in the hypertrophic zones of the growth-plates of rachitic rats compared to control rats. The lack of a calcifying zone in rats exposed to high strontium diet seemed to be similar to our observation of failure in mineralisation of the collagen fibril level in groups supplemented by high strontium concentration. The higher volume fraction of matrix vesicle in the rachitic group than that of the control was also similar to our observation of a higher number of structures that resembled matrix vesicles around the collagen of the group treated with high strontium supplementation.

Observations by Shibata and Yamashita in 2001 are comparable to our findings. This study observed the presence of matrix vesicles around the collagen fibrils of mandibular bone and the hypertrophic zone of condylar cartilage of newborn mice whose mother was treated with strontium carbonate in a vitamin-D deficient and low-calcium diet during pregnancy [323]. This strontium group also showed inhibited mineralisation as it was barely stained with alizarin red, which was a stark contrast to the observation of the strontium-free, normal-diet control group, where collagen was fully mineralised.

The *in vivo* observations by Shibata and Yamashita and Reinholt *et al*. resemble ours: high strontium supplementation alters mineralisation with matrix vesicle-like entities seen in the vicinity of collagen where mineralisation was altered by high strontium supplementation. The observed matrix vesicle volume fraction of a given zone could be described as a function of vesicle formation, rate of vesicle degradation, and turnover of matrix [322]. Since a higher occurrence of matrix vesicles was observed in the hypertrophic zone of the cartilage where chondrocyte matures before subsequently dying at the next calcifying zone, it was argued that the matrix vesicle degradation event was the most likely event occurring in the hypertropic zone; hence, it was very possible that high strontium supplementation altered mineralisation through a change in the degradation of matrix vesicles [322].

The observation in our *in vitro* model seemed to confirm this: supplementation with the highest strontium concentration produced a high number of matrix vesicle-like entities scattered around the collagen matrix. In fact, to use an *in vitro* cell line model to explore and verify such a theory was advantageous because the *in vitro* system provided a more controlled platform with lower biological variability than *in vivo* models. As we observed that only the group supplemented with the highest strontium supplementation seemed to support this model, it is very probable that there exists a threshold amount of strontium supplementation lower than 3 mM but higher than 1 mM strontium (or threshold ratio of calcium to strontium concentrations) that would result in the lowering of the matrix vesicle-like entities degradation rate observed here, but with a lesser extent.

5.4.3. Strontium's Counter Ion or Species may Contribute to the Effects of Strontium Supplementation

Raman spectroscopy allows for the acquisition of a great array of information simultaneously. Owing to the complexity of the Raman signature of the cell and matrix, the effects of strontium supplementation to the cell and matrix are yet been explored fully with Raman spectroscopy with more biochemical approaches preferred (e.g. PCR, calorimetric assays). However, since Raman spectroscopy can provide a low cost and non-discriminative analysis of various cellular and matrix characteristics, it can be used to discern the overall effect and potential 'crosstalk' of strontium supplementation to the cells and matrix.

Jablonski *et al.* used Raman spectroscopy to investigate the influence of strontium chloride and ranelate on bone when administered orally to mice (*in vivo*) [324]. They observed the Raman band at 811 cm^{-1} in bones treated with strontium ranelate, which was suggested to be attributable to the vibrational modes of osteonectin. The absence of this band in the strontium-free control groups and strontium chloride groups was argued to be a sign of low levels of osteonectin. It was also argued that as the strontium ranelate had twice the number of strontium binding sites, the effect of strontium supplementation was observed more clearly than in strontium chloride treated groups [324, 325].

One obvious difference between our system and that of Jablonski *et al.* in [324] is the use of *in vitro* and *in vivo* systems, respectively. The use of an *in vivo* system would mean that the release of strontium might be different to our *in vitro* system (i.e. the involvement of digestive system and enzyme in *in vivo* system versus solubility based on solubility constant in a test tube system). In fact, taking our ICP results into account, we did not see any significant difference in the detected amount of strontium ions in the media supplemented with either 0.1 mM strontium chloride or 0.1 mM strontium ranelate. This could be compared to the two-fold difference in the amount of *in vivo* strontium released between strontium ranelate (having two strontium binding sites) and strontium chloride (having one strontium binding site) [324, 325].

Interestingly, even though the detected level of strontium ions was statistically not different as assessed by ICP, Raman spectroscopy reveals there are some subtle differences between the groups treated with 0.1 mM strontium chloride and those treated with 0.1 mM strontium ranelate. In fact, the crosshairs of the PC scores showed that the groups supplemented with 0.1 mM strontium ranelate were more similar to the groups supplemented with higher concentration of strontium chloride, especially to those supplemented with 3 mM strontium chloride. This Raman observation showed that even though ICP did not detect a statistically significant difference in the strontium ion concentration between strontium ranelate and strontium chloride, the cell response indicated otherwise. Another way to verify the difference between 0.1 mM strontium ranelate and strontium chloride supplementation is to compare cells treated with 0.05 mM strontium ranelate to those treated with 1 mM strontium chloride, where the final strontium ion concentrations of the two groups would be equal (i.e. 0.1 mM strontium ions).

Another reason for the differences between 0.1 mM strontium ranelate and strontium chloride groups may be the result of the difference in strontium's counter ion (i.e. chloride) or species (i.e. ranelate). A study by Yamaguchi *et al.* showed that 200 µM strontium ranelate promoted mineralisation in MC3T3 (day 17; visualised by alizarin red), while groups supplemented by either strontium chloride or a combination of strontium chloride and sodium ranelate did not show such mineralisation [291]. While the study by Yamaguchi *et al.* differed from a more recent study [201][7], strontium's counter ion or species may play a role in influencing cell response in Yamaguchi's *et al.* controlled experiments.

We have only minimally explored the effect of different strontium counter ions or species. To investigate the effect of various counter ions or species further, different salts of strontium can be studied such as strontium carbonate and strontium nitrate. The physical sizes of various counter ions and species may play a role in affecting bone mineralisation.

5.4.4. Strontium Supplementation Increases Lipid Detection by Raman Spectroscopy

Our selection of specific Raman regions for further investigation was made by observing areas where there were differences between the various groups (i.e. using the subtraction between two averaged spectra for two groups or 'subtraction method'). Moreover, the loadings of the PC1 and PC2 (plotted against Raman shift on the x-axis) also gave the indication of which differences were meaningful. When both loadings of PC1 and PC2 were either greater than 0.05 or lower than -0.05, the PCA algorithm detected meaningful differences between the treatments. When the subtraction method was combined with PCA, two Raman regions corresponding to lipid and protein were selected to have meaningful difference between the treatments.

When the subtraction of the average Raman spectra was observed, the differences in lipid detection were minimal at 1725 cm^{-1} and clearer at 1500-1550 cm^{-1}. However, the high PC loadings for both PC1 and PC2 at both Raman regions (greater than 0.05) provided convincing reasoning for the minimal difference to be meaningful. It is not possible to statistically measure the difference between the treatments with our Raman approach – more independent experiments are required. However, from our current dataset it can be concluded that the higher amount of strontium supplementation resulted in a higher lipid detection, satisfying one of our initial hypotheses. In 1994, Neufeld and Boskey published their investigation on strontium

---

[7] Wornham *et al.* showed that primary rat osteoblasts cells treated by either strontium ranelate or strontium chloride at 0.01, 0.1, and 1 mM had inhibited mineralisation to 59, 98, and 100%, respectively.

supplementation on mesenchymal cells differentiation in mineralising medium and *in vivo* rat model [326]. High strontium supplementation resulted in two conflicting events: (1) the increment of complexed acidic phospholipid known to promote *in vitro* and *in vivo* mineralisation; and (2) the decrease of mineralisation parameters. For example, cultures grown in media containing a 4:1 calcium-to-strontium ratio[8] resulted in a higher complexed acidic phospholipid content than that of calcium supplemented cells (i.e. strontium free cultures); they also showed that calcium (Ca^{45}) uptake into the mineralising cultures decreased significantly in the strontium-treated cultures starting at day 14. In the rat model, strontium supplementation elevated the complexed acidic phospholipid content together with altered mineralisation (i.e. reduced in ash weight and hydroxyapatite crystal size of bone of the strontium-treated rats). They explained that the conflicting observations in both *in vitro* and *in vivo* systems indicated that the tissues were prepared to form hydroxyapatite, however, mineral proliferation was impaired because of strontium incorporation into the initial hydroxyapatite crystal.

In Neufeld and Boskey’s study, the high strontium supplementation (Ca:Sr = 4:1) resulted in increased complexed acidic phospholipid, which may explain higher lipid detection in our cultures treated with strontium. The differences between the control and strontium treated culture in the Raman region above 1710 cm^{-1} showed minimal difference, while generally strontium-free control had the lowest lipid detection; at the region of 1500 - 1550 cm^{-1}, strontium-free control had a similar amount of lipid compared to that of the 0.1 mM strontium treated group, and those treated with 1 and 3 mM strontium showed a higher level of lipid. In our cell culture, strontium supplementation was given as 18:1, 1.8:1, and 0.6:1 Ca:Sr for (0.1, 1, and 3 mM strontium supplementation, respectively[9]); of these, those treated with 1 mM and 3 mM strontium fall into the category of rachitic concentrations, and the higher lipid detection is supported by Neufeld and Boskey. The similar lipid level between that observed in the 0.1 mM strontium ranelate group and those in the 1 and 3 mM strontium-treated group may be because of the ranelate counter species, as

---

[8] Serum of strontium-rachitic rats have Ca:Sr of 4:1 (2.4±0.04 mM : 0.62±0.03 mM) [322] Reinholt, F. P., A. Hjerpe, K. Jansson*, et al.*, "Stereological studies on the epiphyseal growth plate in strontium-Induced rickets - with special reference to the distribution of matrix vesicles," *Journal of Bone and Joint Surgery-American Volume,* 66A, 1274-1280, 1984, [326] Neufeld, E. B. and A. L. Boskey, "Strontium Alters the Complexed Acidic Phospholipid Content of Mineralizing Tissues," *Bone,* 15, 425-430, 1994.

[9] αMEM (A10490 - MEM alpha, nucleosides, no ascorbic acid) has calcium level of 1.802 mM (in the form of $CaCl_2$), according to GIBCO.

explained in the earlier paragraphs. Further, taking our Raman and TEM observations together, it is possible that the higher lipid detection in our Raman data is contributed by the high number of matrix vesicle-like entities seen around the collagen fibrils of the cultures supplemented by a high strontium concentration.

5.4.5. Strontium Supplementation may affect the Organisation of Collagen Fibrils

ECM organisation has been reported to be affected by forces exerted by cells, muscles, or other external forces (e.g. tensile) [327, 328]. It is also important in cases such as during *in vivo* inflammation and wound healing. In our *in vitro* model that is free of tensile forces, only the cells and physiochemical forces in the culture environment (such as ionic strength, pH, presence of larger protein molecules from serum supplementation, and temperature) would have effects on the organisation of ECM. With collagen being the highest constituent of ECM in our osteoblast culture, our TEM observation of collagen was also used to ascertain if strontium supplementation would affect the organisation of collagen fibrils.

Although we did not find statistical significance because of the variability between the biological repeats within independent experiments, it is observed that the higher concentrations of strontium supplementation (1 and 3 mM) shifted the organisation of collagen fibrils towards more randomly organised fibrils, satisfying one of our initial hypotheses. The hundreds of TEM micrograph of collagen fibrils analysed also seemed to suggest that the groups treated with 0.1 mM of either strontium chloride or strontium ranelate had the same/less random organisation of fibrils than those in the control. With the current experiment, it is not possible to isolate whether the strontium is directly affecting the organisation of the collagen fibrils by contributing to the physiochemical forces or is indirectly affecting the organisation of the fibril by causing some cellular involvement. It is also possible that the difference in collagen fibril organisation is altogether not affected by the strontium supplementation but by the presence or absence of mineral or abundance of matrix vesicle-like entities. More experiments are needed to attain statistically meaningful data.

A recent publication by Huang *et al*. showed an analysis of mineralised collagen fibril that originated from dissolved collagen suspension (in solution containing Cl^-, Na^+, Ca^{2+}, Sr^{2+}, and phosphate ions) that then formed mineralised collagen fibrils upon changing of the pH [329]. Their FTIR, XRD, SEM, and TEM analysis focused mainly on the mineral analysis and showed that strontium was incorporated into the mineralised collagen fibril and produced mineral crystal with increased *a*- and *c*-axis lattice parameters. In view of this study and along with the limitation of our TEM methods, the following experiment could be conducted to see the effect of strontium supplementation to collagen organisation: an analysis of collagen fibril formation from dissolved collagen in the presence of various concentrations of strontium without the presence of mineral-forming ions (calcium and phosphate). Such an experiment would reduce the complexity of the current *in vitro* system as this acellular model would eliminate the contribution of cells, mineral, and matrix vesicle-like entities.

5.4.6. Strontium Supplementation Affects the Collagen Amount

Because strontium supplementation may contribute to the organisation of collagen fibrils, the amount of collagen from the different treatments was of interest in our present study. The amount of collagen around the cells may contribute to the organisation of collagen fibril as the steric effect may act as a physiochemical parameter that directs collagen fibril organisation.

Collagen amounts were analysed using hydroxyproline quantification and Raman amide I signal. In the context of bone mineralisation and osteoblast culture, amide I is contributed by collagen type I, as collagen type I exists as the most abundant protein [330]. Our Raman experiments showed that amide I signal contributed to the differences between the treatments as observed by using the subtraction method and the PC1 and PC2 loadings that were both greater than 0.05, which indicated that the difference in the amide I signature between the treatments was meaningful. Our Raman result showed that the highest detection of amide I or collagen was found in the strontium-free control, followed by 0.1SrRan, 3Sr, 1Sr, and 0.1Sr.

Our Raman result did not show a clear trend of how the concentration of strontium affected the collagen detection. Instead, our biochemical analysis (hydroxyproline quantification) showed that collagen amount was affected by strontium supplementation. The lack of a statistically significant difference necessitated a conservative conclusion, while more experimental repeats are necessary to achieve statistically conclusive results. However, from our hydroxyproline quantification, a trend was seen in that strontium supplementation may increase collagen amount to

1 mM strontium supplementation before having an adverse effect on the quantity of collagen. It has been previously reported that 1 mM strontium ranelate supplementation to MC3T3 statistically increased collagen synthesis at day 10; however, day 14 cultures treated with 1 mM strontium ranelate showed a higher average value of collagen synthesis than that of strontium-free control, albeit statistically insignificant [154].

The current results, both from Raman and biochemical assay, seem to warrant further studies as the correlation between strontium concentration and collagen amount is not fully confirmed; hence neither proves nor disproves our initial hypothesis. Nevertheless, it can be safely deduced that strontium supplementation affects collagen amount. The current disagreement in the trends of collagen amount between that measured by the Raman versus the hydroxyproline quantification may arise from the technical difficulty that was apparent in the non-mineralising cell culture sample used for Raman measurement but not those used for the hydroxyproline quantification.

5.5. Conclusion and Future Work

This study explored the effect of strontium supplementation on MC3T3 cells *in vitro*, with special focus on strontium's effect on the osteoblast matrix. It was observed that mineralisation was impaired in cultures treated with high strontium supplementation. In these cultures, nodules were formed yet failed to mineralise. TEM observations showed normal collagen banding on all cultures, indicating the production of normal collagen fibrils. Cultures treated with the highest amount of strontium supplementation indicated an abundance of matrix vesicles-like structures around the collagen fibrils. Raman spectroscopy showed an increase in lipid detection on strontium supplemented groups, especially those supplemented with higher strontium concentration. This higher lipid detection in Raman spectroscopy may be due to the increased presence of matrix vesicles. Taken together, high strontium supplementation may decrease the rate of degradation of matrix vesicle, leading to altered mineralisation where nodules could form but fail to mineralise. In the future, an analysis of collagen fibrils formed from dissolved collagen in the presence of various concentrations of strontium but without the presence of mineral-forming ions (calcium and phosphate), and isolation and analysis of the content of matrix vesicles produced, would confirm and compliment the current study with regards to the effect of strontium supplementation to collagen quality and matrix vesicles.

Because no statistically significant result was found in the amount of strontium released between strontium chloride and strontium ranelate, the differences in detected between the groups treated with the same amount of these compounds may be attributable to the counter ion or species (i.e. chloride and ranelate). Further studies could include the observation of the effect of other counter ion or species such as strontium carbonate and strontium nitrate.

The relative amount of collagen was explored by Raman spectroscopy and biochemical analysis. With the disagreement in the trends observed by the two techniques, future work could include increasing the number of experimental repeats.

With the number of studies showing that strontium and calcium are very similar and can act through the same pathways, experiments that would include a calcium-supplemented groups would be necessary to decipher the specific strontium effect on bone mineralisation. Such control groups can also be used to make sure that an increase in the ionic strength of media does not introduce another variable in the study.

Finally, because of the limited number of experimental repeats achieved, the current study has yet conclusively revealed the full effect of strontium ion supplementation to *in vitro* osteoblast, especially to its matrix. Nevertheless, we have been able to show that strontium is effecting the lipid production in committed osteoblasts cells, an observation which was only previously reported in human MSC [205]. Potentially, this observation may reflect the presence of another strontium metabolic pathway that involves the activation of lipid-related genes in osteoblasts.

6. Conclusions and Future Work

6.1. Motivation of the Thesis

Over the past thirty years, research interest in understanding bone as a material has grown, especially with the increased occurrence of age-associated bone diseases. Studies have shown that desirable properties of bone result from highly complex components that form an intricate composite. In fact, bone's hierarchical structure ranging from macro-scale to nano-scale has made it a challenge to reproduce in the lab. Hence, many approaches to cure or alleviate bone-related diseases have been focused on regeneration or prevention rather than treatment or replacement. However, in all of these cases, understanding initial bone formation and processes that support normal bone growth is of paramount importance to successfully designing treatments for bone diseases.

The two studies presented in this thesis were aimed to contribute to: (1) the fundamental understanding of the processes that are involved in the early stages of bone mineralisation; and (2) the understanding of the effect of strontium ion supplementation on bone mineralisation, as an effort to understand how the ions commonly used as anti-osteoporotic treatment affect the bone mineralisation process.

6.2. Nanoscale Analysis of *In Vitro* Bone Mineral Alludes Sequential Crystal Maturation Processes

This work showed the use of TEM and STEM to image, analyse (EDX and EELS), and characterise the ECM mineral of primary mouse osteoblast, and proposed theories in the maturation process of early mineral component of bone mineralisation. It was observed that three stages of calcium phosphate structures were identified in mineralising osteoblast cultures: (1) <80 nm dense granules with low a Ca/P ratio and crystalline domains; (2) needle-like globules comprised with diameter >100 nm; and (3) mature mineral, both with statistically higher Ca/P ratios compared to that of the dense granules. Similar morphological observations of these entities were previously reported in zebrafish and mouse models; however, extensive chemical characterisation compounded with high spatial resolution was not provided as scanning electron microscope was used. The high resolution TEM used in this thesis also revealed the presence of crystalline domains in the dense granules and the needle-like globules; this observation was not previously detected by SAED. Taken together with the reported morphological observations by others, it was concluded that the dense granules were the earliest form of mineral, followed by needle-like globules and mature mineral.

High spatial resolution EELS mapping provided a spatially resolved distribution of carbonate moieties in the mineral. Quantification of these moieties showed a trend where the youngest mineral has more carbonate moieties that decrease as it matures. Carbonate was also found to be located in the middle of the calcium phosphate granules and globules, which suggested that the nucleation of the mineral started with a carbonate-containing precursor. This observation provided physical evidence of a recent study suggesting that calcium-carbonate deposits are the bioseed for calcium phosphate deposition processes in bone.

6.3. Effect of Strontium Ion Supplementation on *In Vitro* Osteoblast Matrix

The work in our second study featured a combination of biochemical approach, TEM, and Raman spectroscopy to investigate the effect of strontium supplementations on *in vitro* osteoblast mineralisation, especially to its matrix component. As the matrix component of bone gives the bone mineral precursor a scaffold to be deposited on and later grow, it is important to understand how strontium supplementation affects bone matrix.

At high strontium concentrations (1 and 3 mM), light microscopy showed the inability for cultures to mineralise. When TEM was used to observe the collagen fibril, cultures treated with high strontium ions showed a marked increase in the presence of matrix vesicles around the collagen fibrils. Increased lipid detection by Raman spectroscopy also supported the TEM observation of increased matrix vesicles. Similar observations were observed in *in vivo* mouse cartilage grown in high strontium surroundings. Together with previous studies, it was hypothesised that high strontium supplementation decreased the degradation rate of matrix vesicles, which altered nodule mineralisation.

The effect on strontium supplementation on the quantity of collagen and collagen fibril organisation was also investigated. Using hydroxyproline quantification, statistically insignificant differences were observed between treatments; a trend was found that a small amount of strontium supplementation increased collagen amount, while high concentrations (3 mM) of strontium supplementation decreased collagen amount. However, Raman spectroscopy failed to show any trends corresponding to the concentration of supplemented strontium. Further investigations are necessary to determine the precise relationship.

The effect of strontium on collagen fibril organisation was studied by analysing hundreds of TEM micrograph of collagen fibrils. Statistical significance was not able to be derived because of the relatively low number of biological repeats; visually, the trends from each repeat showed that the higher concentrations of strontium supplementation shifted the organisation of collagen fibrils towards more randomly organised fibrils, while 0.1 mM supplementation of strontium ions shifted the organisation of fibrils to similar or less random organisation compared to that of the controls. However, it remains challenging to isolate whether strontium was directly affecting the organisation of the collagen fibrils by contributing to the physiochemical forces or by causing some cellular involvement. It is also possible that the difference in collagen fibril organisation was altogether not affected by the strontium supplementation but by the presence or absence of mineral or abundance of matrix vesicles.

6.4. Future Work

Several areas for future studies have been identified below:

- For fundamental understanding on bone mineralisation:
    - to understand the sequence of events further by comparing various time points to allow statistical analysis of the occurrence of the granules and globules over time;
    - to understand the localisation of unbound ions and preserve mineral crystallinity by preparing TEM samples using plunge freezing, followed by cryo-ultramicrotome sectioning and observation by cryo TEM;

  - to confirm that calcium phosphate granules are localised within matrix vesicles by using membrane sensitive stains; and
  - to detect proteins with high spatial resolution with the use of very high energy and spatial resolution electron microscopy, or vibrational spectroscopy at sub-nm scale.

- For understanding the effect of strontium supplementation to bone mineralisation:
  - to ascertain that the increase in media ionic strength does not contribute as another changing parameter by adding control groups such as calcium-supplemented cultures;
  - to ensure that strontium's counter ion or species does not contribute as another variable by adding control groups supplemented with other strontium salts, such as strontium carbonate and strontium nitrate;
  - to further understand the effect of strontium on the vesicle's membrane and content by isolating and analysing the matrix vesicles produced by osteoblast grown in strontium supplemented condition; and
  - to further understand the physiochemical effect of strontium supplementation in the media by analysing collagen fibrils formed from dissolved collagen in the presence of various concentrations of strontium without the presence of mineral-forming ions (calcium and phosphate).

7. References

[1] "World Population Ageing 2013," United Nations, New York, USA, 2013.

[2] "Osteoporosis/Bone Health in Adults as a National Public Health Priority," American Academy of Orthopaedic Surgeons, Illinois, USA, 2009.

[3] Gentleman, E., R. J. Swain, N. D. Evans*, et al.*, "Comparative materials differences revealed in engineered bone as a function of cell-specific differentiation," *Nature Materials,* 8, 763-770, 2009.

[4] Querido, W., A. P. C. Campos, E. H. M. Ferreira*, et al.*, "Strontium ranelate changes the composition and crystal structure of the biological bone-like apatite produced in osteoblast cell cultures," *Cell and Tissue Research,* 357, 835-835, 2014.

[5] Paschalis, E. P., K. Verdelis, S. B. Doty*, et al.*, "Spectroscopic characterization of collagen cross-links in bone," *Journal of Bone and Mineral Research,* 16, 1821-1828, 2001.

[6] Hofstetter, B., S. Gamsjaeger, R. J. Phipps*, et al.*, "Effects of alendronate and risedronate on bone material properties in actively forming trabecular bone surfaces," *Journal of Bone and Mineral Research,* 27, 995-1003, 2012.

[7] Gamsjaeger, S., B. Buchinger, E. Zwettler*, et al.*, "Bone material properties in actively bone-forming trabeculae in postmenopausal women with osteoporosis after three years of treatment with once-yearly zoledronic acid," *Journal of Bone and Mineral Research,* 26, 12-18, 2011.

[8] Gunasegaran, J., *Textbook of Histology and a Practical Guide*, 1st ed. New Delhi, India: Elsevier, 2007.

[9] Weiner, S., W. Traub, and H. D. Wagner, "Lamellar bone: structure-function relations," *Journal of Structural Biology,* 126, 241-255, 1999.

[10] Doblare, M., J. M. Garcia, and M. J. Gomez, "Modelling bone tissue fracture and healing: a review," *Engineering Fracture Mechanics,* 71, 1809-1840, 2004.

[11] Marotti, G., "A new theory of bone lamellation," *Calcified Tissue International,* 53, S47-S56, 1993.

[12] Reznikov, N., R. Shahar, and S. Weiner, "Three-dimensional structure of human lamellar bone: The presence of two different materials and new insights into the hierarchical organization," *Bone,* 59, 93-104, 2014.

[13] Rho, J. Y., L. Kuhn-Spearing, and P. Zioupos, "Mechanical properties and the hierarchical structure of bone," *Medical Engineering & Physics,* 20, 92-102, 1998.

[14] Steele, D. G. and C. A. Bramblett, *The Anatomy and Biology of the Human Skeleton*. Texas, USA: Texas A&M University Press, 1988.

[15] Travlos, G. S., "Normal structure, function, and histology of the bone marrow," *Toxicologic Pathology,* 34, 548-565, 2006.

[16] Grabowski, T., *The Skeleton System: Bone Tissue*, 10th ed. New York, USA: John Wiley and Sons, Inc., 2003.

[17] Rho, J. Y., L. Kuhn-Spearing, and P. Zioupos, "Mechanical properties and the hierarchical structure of bone," *Med Eng Phys,* 20, 92-102, 1998.

[18] Tortora, G. J., *Principles of Human Anatomy*. New York, USA, 1983.

[19] Droll, K. P., H. Broekhuyse, and P. O'Brien, "Fracture of the femoral head," *Journal of the American Academy of Orthopaedic Surgeons,* 15, 716-727, 2007.

[20] Hancox, N. M., *Biological Structure and Function 1: Biology of Bone*. 1: Biology of Bone. London, United Kingdom: Cambridge University Press, 1972.

[21] Smith, J. W., "Collagen fibre patterns in mammalian bone," *Journal of anatomy,* 94, 329-344, 1960.

[22] Buckwalter, J. A., M. J. Glimcher, R. R. Cooper*, et al.*, "Bone Biology 1. Structure, Blood-Supply, Cells, Matrix, and Mineralization," *Journal of Bone and Joint Surgery-American Volume,* 77A, 1256-1275, 1995.

[23] Kaplan, R., *Physical Medicine and Rehabilitation Review: Pearls of Wisdom*. New York, USA: McGraw-Hill Education, 2005.

[24] Kalfas, I. H., "Principles of bone healing," *Neurosurgical Focus,* 10, E1, 2001.

[25] Currey, J. D., *Bones: Structure and Mechanics*. New Jersey, USA: Princeton University Press, 2013.

[26] Landis, W. J., "Mineral characterization in calcifying tissues: atomic, molecular and macromolecular perspectives," *Connective tissue research,* 34, 239-46, 1996.

[27] Burger, C., H. W. Zhou, H. Wang*, et al.*, "Lateral packing of mineral crystals in bone collagen fibrils," *Biophysical Journal,* 95, 1985-1992, 2008.

[28] Jantou-Morris, V., M. A. Horton, and D. W. McComb, "The nano-morphological relationships between apatite crystals and collagen fibrils in ivory dentine," *Biomaterials,* 31, 5275-86, 2010.

[29] Alexander, B., T. L. Daulton, G. M. Genin*, et al.*, "The nanometre-scale physiology of bone: Steric modelling and scanning transmission electron microscopy of collagen-mineral structure," *Journal of the Royal Society Interface,* 2012.

[30] Rossert, J. and B. d. Crombrugghe, "Type I Collagen: Structure, Synthesis, and Regulation," in *Principles of Bone Biology*. 1, 2nd ed. California, USA: Academic Press, 1996.

[31] Fratzl, P., *Collagen: Structure and Mechanics*. New York, USA: Springer, 2008.

[32] Petruska, J. A. and A. J. Hodge, "A subunit model for the tropocollagen macromolecule," *Proceedings of the National Academy of Sciences of the United States of America,* 51, 871-6, 1964.

[33] Vanderrest, M. and R. Garrone, "Collagen family of proteins," *Faseb Journal,* 5, 2814-2823, 1991.

[34] Bansa, M. and C. Ramakrishnan, "A triple-helical model for (gly-pro-hyp)n with cis peptide units," *Biopolymers,* 14, 2457-2466, 1975.

[35] Orgel, J. P., T. C. Irving, A. Miller*, et al.*, "Microfibrillar structure of type I collagen in situ," *Proceedings of the National Academy of Sciences of the United States of America,* 103, 9001-5, 2006.

[36] Ricard-Blum, S., "The collagen family," *Cold Spring Harb Perspect Biol,* 3, a004978, 2011.

[37] Bilezikian, J. P., L. G. Raisz, and T. J. Martin, *Principles of Bone Biology*. Oxford, UK: Elsevier Limited, 2008.

[38] Culav, E. M., C. H. Clark, and M. J. Merrilees, "Connective tissues: Matrix composition and its relevance to physical therapy," *Physical Therapy,* 79, 308-319, 1999.

[39] Glimcher, M. J., "Bone: Nature of the calcium phosphate crystals and cellular, structural, and physical chemical mechanisms in their formation," *Medical Mineraology and Geochemistry,* 64, 223-282, 2006.

[40] Robey, P. G., "Bone Matrix Proteoglycans and Glycoproteins," in *Principles of Bone Biology*. 1, California, USA: Academic Press, 1996.

[41] Kobe, B. and J. Deisenhofer, "Crystal-structure of porcine ribonuclease inhibitor, a protein with leucine-rich repeats," *Nature,* 366, 751-756, 1993.

[42] Grzesik, W. J. and P. G. Robey, "Bone-matrix RGD glycoproteins - immunolocalization and interaction with human primary osteoblastic bone-cell in-vitro," *Journal of Bone and Mineral Research,* 9, 487-496, 1994.

[43] Vermeer, C., "Gamma-carboxyglutamate-containing proteins and the vitamin k-dependent carboxylase," *Biochemical Journal,* 266, 625-636, 1990.

[44] Hoang, Q. Q., F. Sicheri, A. J. Howard*, et al.*, "Bone recognition mechanism of porcine osteocalcin from crystal structure," *Nature,* 425, 977-980, 2003.

[45] Hauschka, P. V., J. B. Lian, D. E. C. Cole*, et al.*, "Osteocalcin and matrix GLA protein - vitamin K-dependent proteins in bone," *Physiological Reviews,* 69, 990-1047, 1989.

[46] Denhardt, D. T. and X. J. Guo, "Osteopontin - a protein with diverse functions," *Faseb Journal,* 7, 1475-1482, 1993.

[47] Lian, J. B., M. D. McKee, A. M. Todd*, et al.*, "Induction of bone-related proteins, osteocalcin and osteopontin, and their matrix ultrastructural-localization with development of chondrocyte hyperthropy in vitro," *Journal of Cellular Biochemistry,* 52, 206-219, 1993.

[48] Boskey, A. L., M. Maresca, W. Ullrich*, et al.*, "Osteopontin-hydroxyapatite interations in vitro - inhibition of hydroxyapatite formation and growth in a gelatin-gel," *Bone and Mineral,* 22, 147-159, 1993.

[49] McKee, M. D., A. Nanci, W. J. Landis*, et al.*, "Developmental appearance and ultrastructural immunolocalization of a major 66-kDa phosphoprotein in embryonic and postnatal chicken bone," *Anatomical Record,* 228, 77-92, 1990.

[50] Sodek, J., J. K. Chen, S. Kasugai*, et al.*, *Elucidating the functions of bone sialoprotein and osteopontin in bone-formation*. 1002. Amsterdam, Netherlands: Elsevier Science, 1992.

[51] Hunter, G. K. and H. A. Goldberg, "Modulation of cyrstal-formation by bone phosphoproteins - role of glutamic acid-rich sequences in the nucleation of hydroxyapatite by bone sialoprotein," *Biochemical Journal,* 302, 175-179, 1994.

[52] Midura, R. J. and V. C. Hascall, "Bone sialoprotein - A mucin in disguise?," *Glycobiology,* 6, 677-681, 1996.

[53] Termine, J. D., H. K. Kleinman, S. W. Whitson*, et al.*, "Osteonectin, a bone-specific protein linking mineral to collagen," *Cell,* 26, 99-105, 1981.

[54] Jahnen-Dechent, W., A. Heiss, C. Schafer*, et al.*, "Fetuin-A regulation of calcified matrix metabolism," *Circulation Research,* 108, 1494-509, 2011.

[55] Schafer, C., A. Heiss, A. Schwarz*, et al.*, "The serum protein alpha(2)-Heremans-Schmid glycoprotein/fetuin-A is a systemically acting inhibitor of ectopic calcification," *Journal of Clinical Investigation,* 112, 357-366, 2003.

[56] Rochette, C. N., S. Rosenfeldt, A. Heiss*, et al.*, "A shielding topology stabilizes the early stage protein-mineral complexes of fetuin-A and calcium phosphate: a time-resolved small-angle X-ray study," *Chembiochem,* 10, 735-40, 2009.

[57] Legros, R., N. Balmain, and G. Bonel, "Age-related changes in mineral of rat and bovine cortical bone," *Calcified Tissue International,* 41, 137-44, 1987.

[58] H. H. Roseberry, A. B. H., and J.K. Morse, "X-Ray analysis of bone and teeth," *Journal of Biological Chemistry,* 60, 395-407, 1931.

[59] Dorozhkin, S. V., "Calcium orthophosphates: occurrence, properties, biomineralization, pathological calcification and biomimetic applications," *Biomatter,* 1, 121-64, 2011.

[60] de Leeuw, N. H., "Computer simulations of structures and properties of the biomaterial hydroxyapatite," *Journal of Materials Chemistry,* 20, 5376-5389, 2010.

[61] Kay, M. I., R. A. Young, and A. S. Posner, "Crystal structure of hydroxyapatite," *Nature,* 204, 1050-2, 1964.

[62] Posner AS, P. A., Diorio AF. , "Refinement of the hydroxyapatite structure," *Acta crystallography,* 11, 308–9, 1958.

[63] Pasteris, J. D., B. Wopenka, J. J. Freeman*, et al.*, "Lack of OH in nanocrystalline apatite as a function of degree of atomic order: implications for bone and biomaterials," *Biomaterials,* 25, 229-38, 2004.

[64] Pasteris, J. D., B. Wopenka, and E. Valsami-Jones, "Bone and tooth mineralization: Why apatite?," *Elements,* 4, 97-104, 2008.

[65] Fletcher DA, M. R., Parkin D., "The United Kingdom chemical database service," *Journal of Chemical Information and Computer Sciences* 36, 746–9, 1996.

[66] Posner, A. S. and F. Betts, "Synthetic amorphous calcium-phosphate and its relation to bone-mineral structure," *Accounts of Chemical Research,* 8, 273-281, 1975.

[67] Lowenstam, H. A. and S. Weiner, *On Biomineralization*. USA: Oxford University Press, 1989.

[68] Fratzl, P., M. Groschner, G. Vogl*, et al.*, "Mineral crystals in calcified tissues: a comparative study by SAXS," *Journal of bone and mineral research,* 7, 329-34, 1992.

[69] Harper, R. A. and A. S. Posner, "Measurement of non-crystalline calcium phosphate in bone mineral," *Proceedings of the Society for Experimental Biology and Medicine,* 122, 137-42, 1966.

[70] Termine, J. D. and A. S. Posner, "Amorphous/crystalline interrelationships in bone mineral," *Calcified Tissue Research,* 1, 8-23, 1967.

[71] Rey, C., C. Combes, C. Drouet*, et al.*, "Bone mineral: update on chemical composition and structure," *Osteoporosis International,* 20, 1013-21, 2009.

[72] Brown, W. E., J. P. Smith, J. R. Lehr*, et al.*, "Octacalcium phosphate and hydroxyapatite: Crystallographic and chemical relations between octacalcium phosphate and hydroxyapatite," *Nature,* 196, 1050-1055, 1962.

[73] Chickerur, N. S., M. S. Tung, and W. E. Brown, "A mechanism for incorporation of carbonate into apatite," *Calcified Tissue International,* 32, 55-62, 1980.

[74] F.C.M. Driessens, R. K. V., *Biominerals*, Illustrated ed. Florida, USA: CRC Press, 1990.

[75] Aubin, J. E. and J. T. Triffit, *Mesenchymal Stem Cells and Osteoblast Differentiation*. 1. California, USA: Academic Press, 1996.

[76] Wu, J. Y., D. T. Scadden, and H. M. Kronenberg, "Role of the osteoblast lineage in the bone marrow hematopoietic niches," *Journal of Bone and Mineral Research,* 24, 759-764, 2009.

[77] Aubin, J. E. and F. Liu, "The Osteoblast Lineage," in *Principles of Bone Biology*. 1, California, USA: Academic Press, 1996.

[78] Hermey, S. C. M. a. D. C., "The Structure and Development of Bone," in *Principles of Bone Biology*. 1, 2 ed. California, USA: Academic Press, 1996.

[79] Franz-Odendaal, T. A., B. K. Hall, and P. E. Witten, "Buried alive: How osteoblasts become osteocytes," *Developmental Dynamics,* 235, 176-190, 2006.

[80] Hadjidakis, D. J. and I. I. Androulakis, "Bone remodeling," *Women's Health and Disease: Gynecologic, Endocrine, and Reproductive Issues,* 1092, 385-396, 2006.

[81] Nijqeide, P. J., E. H. Burger, J. K. Nulend*, et al.*, "The Osteocyte," in *Principles of Bone Biology*. 1, California, USA: Academic Press, 1996.

[82] Boyce, B. F. and L. P. Xing, "Biology of RANK, RANKL, and osteoprotegerin," *Arthritis Research & Therapy,* 9, 2007.

[83] Lee, D. D. and M. J. Glimcher, "3-Dimentional spacial relationship between the collagen fibrils and the inorganic calcium-phosphate cyrstals of pickerel (americanus-americanus) and herring (clupea-harengus) bone," *Journal Molecular Biology,* 217, 487-501, 1991.

[84] Nudelman, F., K. Pieterse, A. George*, et al.*, "The role of collagen in bone apatite formation in the presence of hydroxyapatite nucleation inhibitors," *Nature Materials,* 9, 1004-1009, 2010.

[85] Landis, W. J., K. J. Hodgens, M. J. Song*, et al.*, "Mineralization of collagen may occur on fibril surfaces: Evidence from conventional and high-voltage electron microscopy and three-dimensional imaging," *Journal of Structural Biology,* 117, 24-35, 1996.

[86] Ehrlich, H., T. Hanke, P. Simon*, et al.*, "Carboxymethylation of the fibrillar collagen with respect to formation of hydroxyapatite," *Journal of Biomedical Materials Research Part B-Applied Biomaterials,* 92B, 542-551, 2010.

[87] Silver, F. H. and W. J. Landis, "Deposition of apatite in mineralizing vertebrate extracellular matrices: A model of possible nucleation sites on type I collagen," *Connective Tissue Research,* 52, 242-254, 2011.

[88] Olszta, M. J., X. G. Cheng, S. S. Jee*, et al.*, "Bone structure and formation: A new perspective," *Materials Science & Engineering R-Reports,* 58, 77-116, 2007.

[89] Doi, Y., T. Horiguchi, S. H. Kim*, et al.*, "Effects of noncollagenous proteins on the formation of apatite in calcium beta-glycerophosphate solutions," *Archives of Oral Biology,* 37, 15-21, 1992.

[90] Anderson, H. C., "Vesicles associated with calcification in the matrix of epiphyseal cartilage mouse.," *Journal of Cell Biology,* 41, 59-72, 1969.

[91] Golub, E. E., "Role of matrix vesicles in biomineralization," *Biochimica et Biophysica Acta,* 1790, 1592-1598, 2009.

[92] Bonucci, E., "Fine structure of early cartilage calcification," *Journal of Ultrastructural Research,* 20, 33-50, 1967.

[93] Xiao, Z., C. E. Camalier, K. Nagashima*, et al.*, "Analysis of the extracellular matrix vesicle proteome in mineralizing osteoblasts," *Journal of Cell Physiology,* 210, 325-35, 2007.

[94] Xiao, Z., J. Blonder, M. Zhou*, et al.*, "Proteomic analysis of extracellular matrix and vesicles," *Journal of Proteomics,* 72, 34-45, 2009.

[95] Arana-Chavez, V. E. and L. F. Massa, "Odontoblasts: The cells forming and maintaining dentine," *The International Journal of Biochemistry,* 36, 1367-1373, 2004.

[96] Hayashi, Y. and H. Nagasawa, "Matrix vesicles isolated from apical pulp of rat incisors: Crystal formation in low Ca×Pi ion-product medium containing β-glycerophosphate," *Calcified Tissue International,* 47, 365-372, 1990.

[97] Landis, W. J. and F. H. Silver, "The structure and function of normally mineralizing avian tendons," *Comparative Biochemistry and Physiology Part A: Molecular & Integrative Physiology,* 133, 1135-1157, 2002.

[98] Muhlrad, A., A. Setton, J. Sela*, et al.*, "Biochemical characterization of matrix vesicles from bone and cartilage," *Metabolic Bone Disease & Related Research,* 5, 93-9, 1983.

[99] Rabinovitch, A. L. and H. C. Anderson, "Biogenesis of matrix vesicles in cartilage growth plates," *Federation Proceedings,* 35, 112-116, 1976.

[100] Anderson, H. C., "Molecular-biology of matrix vesicles," *Clinical Orthopaedics and Related Research,* 266-280, 1995.

[101] Wuthier, R. E., "Lipid-composition of isolated epiphyseal cartilage cells, membranes and matrix vescicles," *Biochimica Et Biophysica Acta,* 409, 128-143, 1975.

[102] Cecil, R. N. A. and H. C. Anderson, "Freeze-fracture studies of matrix vesicle calcification in epiphyseal growth plate," *Metabolic Bone Disease Related Research,* 1, 89-95, 1978.

[103] Wuthier, R. E., "Electrolytes of isolated epiphyseal chondrocytes, matrix vesicles, and extracellular fluid," *Calcified Tissue Research,* 23, 125-133, 1977.

[104] Wuthier, R. E., "Mechanism of matrix vesicle-mediated mineralization of cartilage," *Isi Atlas of Science-Biochemistry,* 1, 231-241, 1988.

[105] Ali, S. Y., S. W. Sajdera, and H. C. Anderson, "Isolation and characterization of calcifying matrix vesicles from epiphyseal cartilage," *Proceedings of the National Academy of Sciences of the United States of America,* 67, 1513-1520, 1970.

[106] Kirsch, T., "Annexins - Their role in cartilage mineralization," *Frontiers in Bioscience,* 10, 576-581, 2005.

[107] Kirsch, T. and H. Claassen, "Matrix vesicles mediate mineralization of human thyroid cartilage," *Calcified Tissue International,* 66, 292-297, 2000.

[108] Hessle, L., K. A. Johnson, H. C. Anderson*, et al.*, "Tissue-nonspecific alkaline phosphatase and plasma cell membrane glycoprotein-1 are central antagonistic regulators of bone mineralization," *Proceedings of the National Academy of Sciences of the United States of America,* 99, 9445-9449, 2002.

[109] Henthorn, P. S. and M. P. Whyte, "Missense mutation of the tissue-nonspecific alkaline-phosphatase gene in hypophosphatasia," *Clinical Chemistry,* 38, 2501-2505, 1992.

[110] Xiao, Z., C. E. Camalier, K. Nagashima*, et al.*, "Analysis of the extracellular matrix vesicle proteome in mineralizing osteoblasts," *Journal of Cell Physiology,* 210, 325-335, 2007.

[111] Kirsch, T., "Annexins and tissue mineralization: matrix vesicles, ion channel activity of annexins and annexin V/collagen interactions," Springer US, 2003.

[112] Wu, L. N. Y., B. R. Genge, G. C. Lloyd*, et al.*, "Collagen-binding proteins in collagenase-released matrix vesicles from cartilage - interaction between matrix vesicle proteins and different types of collagen," *Journal of Biological Chemistry,* 266, 1195-1203, 1991.

[113] Cmoch, A., A. Strzelecka-Kiliszek, M. Palczewska*, et al.*, "Matrix vesicles isolated from mineralization-competent Saos-2 cells are selectively enriched with annexins and S100 proteins," *Biochemical and Biophysical Research Communications,* 412, 683-687, 2011.

[114] Kirsch, T. and M. Pfaffle, "Selective Binding of Anchorin-Cii (Annexin-V) to Type-Ii and X-Collagen and to Chondrocalcin (C-Propeptide of Type-Ii

Collagen) - Implications for Anchoring Function between Matrix Vesicles and Matrix Proteins," *Febs Letters,* 310, 143-147, 1992.

[115] Arispe, N., E. Rojas, B. R. Genge*, et al.*, "Similarity in calcium channel activity of annexin V and matrix vesicles in planar lipid bilayers," *Biophysical Journal,* 71, 1764-1775, 1996.

[116] Brachvogel, B., J. Dikschas, H. Moch*, et al.*, "Annexin A5 is not essential for skeletal development," *Molecular and Cellular Biology,* 23, 2907-2913, 2003.

[117] Belluoccio, D., I. Grskovic, A. Niehoff*, et al.*, "Deficiency of annexins A5 and A6 induces complex changes in the transcriptome of growth plate cartilage but does not inhibit the induction of mineralization," *Journal of Bone and Mineral Research,* 25, 141-153, 2010.

[118] Wu, L. N. Y., B. R. Genge, D. G. Dunkelberger*, et al.*, "Physicochemical characterization of the nucleational core of matrix vesicles," *Journal of Biological Chemistry,* 272, 4404-4411, 1997.

[119] Sauer, G. R. and R. E. Wuthier, "Fourier-transform infrared characterization of mineral phases formed during induction of mineralization by collagenase-released matrix vesicles in vitro," *Journal of Biological Chemistry,* 263, 13718-13724, 1988.

[120] Boonrungsiman, S., E. Gentleman, R. Carzaniga*, et al.*, "The role of intracellular calcium phosphate in osteoblast-mediated bone apatite formation," *Proceedings of the National Academy of Sciences of the United States of America,* 2012.

[121] Mahamid, J., A. Sharir, D. Gur*, et al.*, "Bone mineralization proceeds through intracellular calcium phosphate loaded vesicles: a cryo-electron microscopy study," *Journal of Structural Biology,* 174, 527-35, 2011.

[122] Rohde, M. and H. Mayer, "Exocytotic process as a novel model for mineralization by osteoblasts In vitro and In vivo determined by electron microscopic analysis," *Calcified Tissue International,* 80, 323-336, 2007.

[123] Carter, D. H., P. V. Hatton, and J. E. Aaron, "The ultrastructure of slam-frozen bone mineral," *Histochemical Journal,* 29, 783-793, 1997.

[124] Lehninger, A. L., "Mitochondria and calcium ion transport," *Biochemical Journal,* 119, 129-38, 1970.

[125] Hendricks, S. B. and W. L. Hill, "The nature of bone and phosphate rock," *Proceedings of the National Academy of Sciences of the United States of America,* 36, 731-7, 1950.

[126] Watson, R. A. R. a. M. L., "Crystal-collagen relationships in bone as bbserved in the electron microscope. III. Crystal and collagen morphology as a function of age," *Annals of the New York Academy of Sciences,* 60, 596-630, 1955.

[127] Burnell, J. M., E. J. Teubner, and A. G. Miller, "Normal maturational changes in bone matrix, mineral, and crystal size in the rat," *Calcified Tissue International,* 31, 13-9, 1980.

[128] Posner, A. S., R. A. Harper, S. A. Muller*, et al.*, "Age changes in the crystal chemistry of bone apatite," *Annals of New York Academy of Sciences,* 131, 737-42, 1965.

[129] Mahamid, J., A. Sharir, L. Addadi*, et al.*, "Amorphous calcium phosphate is a major component of the forming fin bones of zebrafish: Indications for an amorphous precursor phase," *Proceedings of the National Academy of Sciences of the United States of America,* 105, 12748-12753, 2008.

[130] Dey, A., P. H. H. Bomans, F. A. Mueller*, et al.*, "The role of prenucleation clusters in surface-induced calcium phosphate crystallization," *Nature Materials,* 9, 1010-1014, 2010.

[131] Coelfen, H., "Biomineralization - A crystal-clear view," *Nature Materials,* 9, 960-961, 2010.

[132] Mahamid, J., B. Aichmayer, E. Shimoni*, et al.*, "Mapping amorphous calcium phosphate transformation into crystalline mineral from the cell to the bone in zebrafish fin rays," *Proceedings of the National Academy of Sciences of the United States of America,* 107, 6316-21, 2010.

[133] Habraken, W. J., J. Tao, L. J. Brylka*, et al.*, "Ion-association complexes unite classical and non-classical theories for the biomimetic nucleation of calcium phosphate," *Nature Communication,* 4, 1507, 2013.

[134] Rey, C., H. M. Kim, L. Gerstenfeld*, et al.*, "Structural and chemical characteristics and maturation of the calcium-phosphate crystals formed during the calcification of the organic matrix synthesized by chicken osteoblasts in cell culture," *Journal of Bone Mineral Research,* 10, 1577-88, 1995.

[135] Rey, C., H. M. Kim, L. Gerstenfeld*, et al.*, "Characterization of the apatite crystals of bone and their maturation in osteoblast cell culture: Comparison with native bone crystals," *Connective tissue research,* 35, 343-349, 1996.

[136] Muller, W. E. G., H. C. Schroder, U. Schlossmacher*, et al.*, "Induction of carbonic anhydrase in SaOS-2 cells, exposed to bicarbonate and consequences for calcium phosphate crystal formation," *Biomaterials,* 34, 8671-8680, 2013.

[137] Hope, T. C., "Account of a mineral from Strontian and of a particular species of earth which it contains," *Transactions of the Royal Society of Edinburgh,* 4, 3-39, 1798.

[138] McCaslin, F. E. J., Janes, J.M., "The effect of strontium lactate in the treatment of osteoporosis," *Proceedings of Staff Meetings of the Mayo Clinic,* 34, 329-334, 1959.

[139] Sobel, A. E., J. Cohen, and B. Kramer, "The nature of the injury to the calcifying mechanism in rickets due to strontium," *Biochemical Journal,* 29, 2640-5, 1935.

[140] Skoryna, S. C. and D. S. Kahn, "The late effects of radioactive strontium on bone; histogenesis of bone tumors produced in rats by high Sr89 dosage," *Cancer,* 12, 306-22, 1959.

[141] Jones, G., T. Nguyen, P. N. Sambrook*, et al.*, "Symptomatic fracture incidence in elderly men and women: the Dubbo Osteoporosis Epidemiology Study (DOES)," *Osteoporosis International,* 4, 277-82, 1994.

[142] Klibanski, A., L. Adams-Campbell, T. Bassford*, et al.*, "Osteoporosis prevention, diagnosis, and therapy," *Jama-Journal of the American Medical Association,* 285, 785-795, 2001.

[143] Fuller Albright, P. H. S., Anna M. Richardson, "Postmenopausal osteoporosis: Its clinical features," *Journal of the American Medical Association,* 116, 2465-2474, 1941.

[144] Grynpas, M. D., E. Hamilton, R. Cheung*, et al.*, "Strontium increases vertebral bone volume in rats at a low dose that does not induce detectable mineralization defect," *Bone,* 18, 253-259, 1996.

[145] Marie, P. J. and M. Hott, "Short-term effects of fluoride and strontium on bone-formation and resorption in the mouse," *Metabolism-Clinical and Experimental,* 35, 547-551, 1986.

[146] Meunier, P. J., C. Roux, E. Seeman*, et al.*, "The effects of strontium ranelate on the risk of vertebral fracture in women with postmenopausal osteoporosis," *The New England Journal of Medicine,* 350, 459-68, 2004.

[147] Meunier, P. J., C. Roux, S. Ortolani*, et al.*, "Effects of long-term strontium ranelate treatment on vertebral fracture risk in postmenopausal women with osteoporosis," *Osteoporosis International,* 20, 1663-73, 2009.

[148] Reginster, J. Y., D. Felsenberg, S. Boonen*, et al.*, "Effects of long-term strontium ranelate treatment on the risk of nonvertebral and vertebral fractures in postmenopausal osteoporosis - Results of a five-year, randomized, placebo-controlled trial," *Arthritis Rheumatism,* 58, 1687-1695, 2008.

[149] Boivin, G. Y., E. Foos, I. Tupinon-Mathieu*, et al.*, "Strontium deposition in bone is dose dependent and does not alter the degree of mineralization of bone in osteoporotic patients treated with strontium ranelate.," *Journal of Bone and Mineral Research,* 15, S305-S305, 2000.

[150] Li, C., O. Paris, S. Siegel*, et al.*, "Strontium is incorporated into mineral crystals only in newly formed bone during strontium ranelate treatment," *Journal of Bone and Mineral Research,* 25, 968-975, 2010.

[151] Roschger, P., I. Manjubala, N. Zoeger*, et al.*, "Bone material quality in transiliac bone biopsies of postmenopausal osteoporotic women after 3 years of strontium ranelate treatment," *Journal of Bone Minerals Research,* 25, 891-900, 2010.

[152] Farlay, D., G. Boivin, G. Panczer*, et al.*, "Long-term strontium ranelate administration in monkeys preserves characteristics of bone mineral crystals and degree of mineralization of bone," *Journal of Bone Minerals Research,* 20, 1569-78, 2005.

[153] Stepan, J. J., "Strontium ranelate: in search for the mechanism of action," *Journal of Bone and Mineral Metabolism,* 31, 606-612, 2013.

[154] Barbara, A., P. Delannoy, B. G. Denis*, et al.*, "Normal matrix mineralization induced by strontium ranelate in MC3T3-E1 osteogenic cells," *Metabolism-Clinical and Experimental,* 53, 532-537, 2004.

[155] Canalis, E., M. Hott, P. Deloffre*, et al.*, "The divalent strontium salt S12911 enhances bone cell replication and bone formation in vitro," *Bone,* 18, 517-23, 1996.

[156] Bonnelye, E., A. Chabadel, F. Saltel*, et al.*, "Dual effect of strontium ranelate: stimulation of osteoblast differentiation and inhibition of osteoclast formation and resorption in vitro," *Bone,* 42, 129-38, 2008.

[157] Brennan, T. C., M. S. Rybchyn, W. Green*, et al.*, "Osteoblasts play key roles in the mechanisms of action of strontium ranelate," *British Journal and Pharmacology,* 157, 1291-300, 2009.

[158] Saidak, Z., E. Hay, C. Marty*, et al.*, "Strontium ranelate rebalances bone marrow adipogenesis and osteoblastogenesis in senescent osteopenic mice through NFATc/Maf and Wnt signaling," *Aging Cell,* 11, 467-474, 2012.

[159] Yang, F., D. Yang, J. Tu*, et al.*, "Strontium enhances osteogenic differentiation of mesenchymal stem cells and in vivo bone formation by activating Wnt/catenin signaling," *Stem Cells,* 29, 981-91, 2011.

[160] Peng, S., G. Zhou, K. D. Luk*, et al.*, "Strontium promotes osteogenic differentiation of mesenchymal stem cells through the Ras/MAPK signaling pathway," *Cellular Physiology and Biochemistry,* 23, 165-74, 2009.

[161] Fournier, C., A. Perrier, M. Thomas*, et al.*, "Reduction by strontium of the bone marrow adiposity in mice and repression of the adipogenic commitment of multipotent C3H10T1/2 cells," *Bone,* 50, 499-509, 2012.

[162] Bakker, A. D., B. Zandieh-Doulabi, and J. Klein-Nulend, "Strontium ranelate affects signaling from mechanically-stimulated osteocytes towards osteoclasts and osteoblasts," *Bone,* 53, 112-119, 2013.

[163] Takahashi, N., T. Sasaki, Y. Tsouderos*, et al.*, "S 12911-2 inhibits osteoclastic bone resorption in vitro," *Journal of Bone and Mineral Research,* 18, 1082-1087, 2003.

[164] Chattopadhyay, N., S. J. Quinn, O. Kifor*, et al.*, "The calcium-sensing receptor (CaR) is involved in strontium ranelate-induced osteoblast proliferation," *Biochemical Pharmacology,* 74, 438-47, 2007.

[165] Coulombe, J., H. Faure, B. Robin*, et al.*, "In vitro effects of strontium ranelate on the extracellular calcium-sensing receptor," *Biochemical and Biophysical Research Communications,* 323, 1184-1190, 2004.

[166] Caudrillier, A., A. S. Hurtel-Lemaire, A. Wattel*, et al.*, "Strontium ranelate decreases receptor activator of nuclear factor-kappa B ligand-induced osteoclastic differentiation in vitro: involvement of the calcium-sensing receptor," *Molecular Pharmacology,* 78, 569-576, 2010.

[167] Chattopadhyay, N., S. J. Quinn, O. Kifor*, et al.*, "The calcium-sensing receptor (CaR) is involved in strontium ranelate-induced osteoblast proliferation," *Biochemical Pharmacology,* 74, 438-447, 2007.

[168] Takaoka, S., T. Yamaguchi, S. Yano*, et al.*, "The calcium-sensing receptor (CaR) is involved in strontium ranelate-induced osteoblast differentiation and mineralization," *Hormone and Metabolic Research,* 42, 627-631, 2010.

[169] Hurtel-Lemaire, A. S., R. Mentaverri, A. Caudrillier*, et al.*, "The calcium-sensing receptor is involved in strontium ranelate-induced osteoclast apoptosis: New insights into the associated signaling pathways," *Journal of Biological Chemistry,* 284, 575-584, 2009.

[170] Fromigue, O., E. Hay, A. Barbara*, et al.*, "Calcium sensing receptor-dependent and receptor-independent activation of osteoblast replication and survival by strontium ranelate," *Journal of Cellular and Molecular Medicine,* 13, 2189-2199, 2009.

[171] Saidak, Z. and P. J. Marie, "Strontium signaling: Molecular mechanisms and therapeutic implications in osteoporosis," *Pharmacology & Therapeutics,* 136, 216-226, 2012.

[172] Reginster, J. Y., R. Deroisy, A. Neuprez*, et al.*, "Strontium ranelate: new data on fracture prevention and mechanisms of action," *Current Osteoporosis Reports,* 7, 96-102, 2009.

[173] Marie, P. J., P. Ammann, G. Boivin*, et al.*, "Mechanisms of action and therapeutic potential of strontium in bone," *Calcified Tissue International,* 69, 121-9, 2001.

[174] Boivin, G. and P. J. Meunier, "The mineralization of bone tissue: a forgotten dimension in osteoporosis research," *Osteoporosis International,* 14 Suppl 3, S19-24, 2003.

[175] Boivin, G., E. Schenker, I. Tupinon-Mathieu*, et al.*, "Uptake and distribution of strontium in human bone, evolution of the degree of mineralisation after strontium ranelate administration.," *Journal of Bone and Mineral Research,* 14, S284-S284, 1999.

[176] Boivin, G., P. Deloffre, B. Perratmabilon*, et al.*, "Strontium distribution in monkey iliac bone after S12911 administration - an X-ray-microanalysis," *Journal of Bone and Mineral Research,* 8, S270-S270, 1993.

[177] Boivin, G., P. Deloffre, B. Perrat*, et al.*, "Strontium distribution and interactions with bone mineral in monkey iliac bone after strontium salt (S

12911) administration," *Journal of Bone Minerals Research,* 11, 1302-11, 1996.

[178] Li, Z., W. W. Lu, L. Deng*, et al.*, "The morphology and lattice structure of bone crystal after strontium treatment in goats," *Journal of Bone and Mineral Metabolism,* 28, 25-34, 2010.

[179] Dahl, S. G., P. Allain, P. J. Marie*, et al.*, "Incorporation and distribution of strontium in bone," *Bone,* 28, 446-53, 2001.

[180] Bazin, D., A. Dessombz, C. Nguyen*, et al.*, "The status of strontium in biological apatites: an XANES/EXAFS investigation," *Journal Synchrotron Radiation,* 21, 136-42, 2014.

[181] Querido, W., A. P. Campos, E. H. Martins Ferreira*, et al.*, "Strontium ranelate changes the composition and crystal structure of the biological bone-like apatite produced in osteoblast cell cultures," *Cell and Tissue Research,* 2014.

[182] Rossi, A. L., S. Moldovan, W. Querido*, et al.*, "Effect of strontium ranelate on bone mineral: Analysis of nanoscale compositional changes," *Micron,* 56, 29-36, 2014.

[183] Frankaer, C. G., A. C. Raffalt, and K. Stahl, "Strontium localization in bone tissue studied by X-ray absorption spectroscopy," *Calcified Tissue International,* 94, 248-57, 2014.

[184] Yalin, S., Comelekoglu, U., Bagis, S., Yilmaz N., "Effects of strontium ranelate on cortical bone collagen integrity," *Saudi Medical Journal,* 33, 515-519, 2010.

[185] Cattani-Lorente, M., R. Rizzoli, and P. Ammann, "In vitro bone exposure to strontium improves bone material level properties," *Acta Biomaterialia,* 9, 7005-13, 2013.

[186] Marie, P. J., M. T. Garba, M. Hott*, et al.*, "Effect of low-doses of stable strontium on bone metabolism in rats," *Mineral and Electrolyte Metabolism,* 11, 5-13, 1985.

[187] Marie, P. J., M. Hott, D. Modrowski*, et al.*, "An uncoupling agent containing strontium prevents bone loss by depressing bone resorption and maintaining bone formation in estrogen-deficient rats," *Journal of Bone Minerals Research,* 8, 607-15, 1993.

[188] Matsumoto, A., "Effect of strontium chloride on bone resorption induced by prostaglandin E2 in cultured bone," *Archives of Toxicology,* 62, 240-1, 1988.

[189] Grynpas, M. D. and P. J. Marie, "Effects of low-doses of strontium on bone quality and quantity in rats," *Bone,* 11, 313-319, 1990.

[190] Buehler, J., P. Chappuis, J. L. Saffar*, et al.*, "Strontium ranelate inhibits bone resorption while maintaining bone formation in alveolar bone in monkeys (Macaca fascicularis)," *Bone,* 29, 176-179, 2001.

[191] Delannoy, P., D. Bazot, and P. J. Marie, "Long-term treatment with strontium ranelate increases vertebral bone mass without deleterious effect in mice," *Metabolism-Clinical and Experimental,* 51, 906-911, 2002.

[192] Reginster, J. Y., R. Deroisy, M. Dougados*, et al.*, "Prevention of early postmenopausal bone loss by strontium ranelate: The randomized, two-year, double-masked, dose-ranging, placebo-controlled PREVOS trial," *Osteoporosis International,* 13, 925-931, 2002.

[193] Meunier, P. J., D. O. Slosman, P. D. Delmas*, et al.*, "Strontium ranelate: Dose-dependent effects in established postmenopausal vertebral osteoporosis - a 2-year randomized placebo controlled trial," *Journal of Clinical Endocrinology & Metabolism,* 87, 2060-2066, 2002.

[194] Reginster, J. Y., O. Bruyere, A. Sawicki*, et al.*, "Long-term treatment of postmenopausal osteoporosis with strontium ranelate: results at 8 years," *Bone,* 45, 1059-64, 2009.

[195] Hott, M., P. Deloffre, Y. Tsouderos*, et al.*, "S12911-2 reduces bone loss induced by short-term immobilization in rats," *Bone,* 33, 115-123, 2003.

[196] Ammann, P., V. Shen, B. Robin*, et al.*, "Strontium ranelate improves bone resistance by increasing bone mass and improving architecture in intact female rats," *Journal of Bone and Mineral Research,* 19, 2012-2020, 2004.

[197] Ferraro, E. F., R. Carr, and K. Zimmerman, "A Comparison of the Effects of Strontium Chloride and Calcium-Chloride on Alveolar Bone," *Calcified Tissue International,* 35, 258-260, 1983.

[198] Peng, S. L., X. S. Liu, S. S. Huang*, et al.*, "The cross-talk between osteoclasts and osteoblasts in response to strontium treatment: Involvement of osteoprotegerin," *Bone,* 49, 1290-1298, 2011.

[199] Chavassieux, P., P. J. Meunier, J. P. Roux*, et al.*, "Bone histomorphometry of transiliac paired bone biopsies after 6 or 12 months of treatment with oral strontium ranelate in 387 osteoporotic women: Randomized comparison to alendronate," *Journal of Bone and Mineral Research,* 29, 618-628, 2014.

[200] Rizzoli, R., R. D. Chapurlat, J. M. Laroche*, et al.*, "Effects of strontium ranelate and alendronate on bone microstructure in women with osteoporosis. Results of a 2-year study," *Osteoporosis International,* 23, 305-15, 2012.

[201] Wornham, D. P., M. O. Hajjawi, I. R. Orriss*, et al.*, "Strontium potently inhibits mineralisation in bone-forming primary rat osteoblast cultures and reduces numbers of osteoclasts in mouse marrow cultures," *Osteoporosis International,* 25, 2477-2484, 2014.

[202] Omdahl, J. L. and H. F. DeLuca, "Strontium induced rickets: metabolic basis," *Science,* 174, 949-51, 1971.

[203] Schrooten, I., W. Cabrera, W. G. Goodman*, et al.*, "Strontium causes osteomalacia in chronic renal failure rats," *Kidney International,* 54, 448-56, 1998.

[204] D'Haese, P. C., I. Schrooten, W. G. Goodman*, et al.*, "Increased bone strontium levels in hemodialysis patients with osteomalacia," *Kidney International,* 57, 1107-1114, 2000.

[205] Autefage, H., E. Gentleman, E. Littmann*, et al.*, "Sparse feature selection methods identify unexpected global cellular response to strontium-containing materials," *Proceedings of the National Academy of Sciences of the United States of America,* 112, 4280-5, 2015.

[206] Christoffersen, J., M. R. Christoffersen, N. Kolthoff*, et al.*, "Effects of strontium ions on growth and dissolution of hydroxyapatite and on bone mineral detection," *Bone,* 20, 47-54, 1997.

[207] Verberckmoes, S. C., G. J. Behets, L. Oste*, et al.*, "Effects of strontium on the physicochemical characteristics of hydroxyapatite," *Calcified Tissue International,* 75, 405-15, 2004.

[208] Peck, W. A., S. J. Birge, Jr., and S. A. Fedak, "Bone cells: biochemical and biological studies after enzymatic isolation," *Science,* 146, 1476-7, 1964.

[209] Wong, G. L. and D. V. Cohn, "Target cells in bone for parathormone and calcitonin are different: enrichment for each cell type by sequential digestion of mouse calvaria and selective adhesion to polymeric surfaces," *Proceedings of the National Academy of Sciences of the United States of America,* 72, 3167-71, 1975.

[210] Helfrich, M. H. and S. Ralston, *Bone Research Protocols*. New Jersey, USA: Humana Press, 2003.

[211] Ecarot-Charrier, B., N. Shepard, G. Charette*, et al.*, "Mineralization in osteoblast cultures: a light and electron microscopic study," *Bone,* 9, 147-54, 1988.

[212] Bhargava, U., M. Barlev, C. G. Bellows*, et al.*, "Ultrastructural analysis of bone nodules formed in vitro by isolated fetal-rat calvaria cells," *Bone,* 9, 155-163, 1988.

[213] H.Y. Kodama, Y. A., H. Sudo, S. Kasai, S. Yamamoto, "Establishment of a clonal osteogenic cell kube fron newborn mouse calvaria," *Journal of Oral Biology,* 23, 899-901, 1981.

[214] Wang, D., K. Christensen, K. Chawla*, et al.*, "Isolation and characterization of MC3T3-E1 preosteoblast subclones with distinct in vitro and in vivo differentiation/mineralization potential," *Journal of Bone Mineral Research,* 14, 893-903, 1999.

[215] Quarles, L. D., D. A. Yohay, L. W. Lever*, et al.*, "Distinct proliferative and differentiated stages of murine MC3T3-E1 cells in culture - An in vitro model of osteoblast development," *Journal of Bone and Mineral Research,* 7, 683-692, 1992.

[216] Choi, J. Y., B. H. Lee, K. B. Song*, et al.*, "Expression patterns of bone-related proteins during osteoblastic differentiation in MC3T3-E1 cells," *Journal of Cellular Biochemistry,* 61, 609-618, 1996.

[217] Marsh, M. E., A. M. Munne, J. J. Vogel*, et al.*, "Mineralization of bone-like extracellular matrix in the absence of functional osteoblasts," *Journal of Bone and Mineral Research,* 10, 1635-1643, 1995.

[218] Franceschi, R. T., B. S. Iyer, and Y. Cui, "Effects of ascorbic acid on collagen matrix formation and osteoblast differentiation in murine MC3T3-E1 cells," *Journal of Bone Minerals Research,* 9, 843-54, 1994.

[219] Bellows, C. G., J. N. M. Heersche, and J. E. Aubin, "Inorganic phosphate added exogenously or released from β-glycerophosphate initiates mineralization of osteoid nodules in vitro," *Bone Mineralization,* 17, 15-29, 1992.

[220] Boonrungsiman, S., "Comparison of Ultrastructure and Mineralisation in Bone-Like Tissues Derived from Mouse Osteoblasts, Mesenchymal Stem Cells and Embryonic Stem Cells," PhD Thesis, Materials, Imperial College London, London, UK, 2011.

[221] Williams, D. B. and C. B. Carter, *Transmission Electron Microscopy: A Textbook for Materials Science*, 1st ed. New York, USA: Plenum Press, 1996.

[222] Oldfield, R. J., *Light Microscopy: An Illustrated Guide*: Wolfe, 1994.

[223] Warwick University. (2010, 17 October 2014). *Transmission Electron Microscopy (TEM)*. Available: http://www2.warwick.ac.uk/fac/sci/physics/current/postgraduate/regs/mpags/ex5/techniques/structural/tem/

[224] Williams, D. B., Carter, C. Barry, *Transmission electron microscopy : a textbook for materials science*, 2nd ed. New York, USA: Springer, 2008.

[225] Pennycook, S. J., M. Varela, C. J. D. Hetherington*, et al.*, "Materials advances through aberration-corrected electron microscopy," *Mrs Bulletin,* 31, 36-43, 2006.

[226] Neu, C. P. and G. M. Genin, *Handbook of imaging in biological mechanics*.

[227] Egerton, R. F., P. Li, and M. Malac, "Radiation damage in the TEM and SEM," *Micron,* 35, 399-409, 2004.

[228] Julian Seifter, D. S., Austin Ratner. (2005, 03 April 2012). *Concepts in Medical Physiology*.

[229] Australian Microscopy & Microanalysis Research Facility. (2014, 17 October 2014). *X-ray Intensity*. Available: http://www.ammrf.org.au/myscope/analysis/eds/xrayintensity/

[230] Egerton, R. F., *Electron energy-loss spectroscopy in the electron microscope*, 2nd ed. New York, USA: Plenum Press, 1996.

[231] M. Weyland, P. J. T., P.A. Midgley, *Advances in high resolution elemental analysis using image-spectroscopy*. 5. New York, USA: Wiley-VCH Verlag GmbH, 2000.

[232] Leibniz Institute. (2006, 22 January 2016). *Spectroscopy inside TEM (EELS/EDXS)*. Available: https://www.ifw-dresden.de/?id=344

[233] Lerotic, M., C. Jacobsen, T. Schafer*, et al.*, "Cluster analysis of soft X-ray spectromicroscopy data," *Ultramicroscopy,* 100, 35-57, 2004.

[234] Osanna, A. and C. Jacobsen, "Principal component analysis for soft X-ray spectromicroscopy," *X-Ray Microscopy, Proceedings,* 507, 350-357, 2000.

[235] Koprinarov, I. N., A. P. Hitchcock, C. T. McCrory*, et al.*, "Quantitative mapping of structured polymeric systems using singular value decomposition analysis of soft X-ray images," *Journal of Physical Chemistry B,* 106, 5358-5364, 2002.

[236] Tomus, D. and H. P. Ng, "In situ lift-out dedicated techniques using FIB-SEM system for TEM specimen preparation," *Micron,* 44, 115-119, 2013.

[237] Posner, A., F. Betts, and N. Blumenthal, "Properties of nucleating systems," *Metabolic Bone Disease and Related Research,* 1, 179-183, 1978.

[238] Landis, W. J. and M. J. Glimcher, "Electron diffraction and electron probe microanalysis of the mineral phase of bone tissue prepared by anhydrous techniques," *Journal of Ultrastructure Research,* 63, 188-223, 1978.

[239] Porter, A. E., N. Patel, J. N. Skepper*, et al.*, "Effect of sintered silicate-substituted hydroxyapatite on remodelling processes at the bone-implant interface," *Biomaterials,* 25, 3303-3314, 2004.

[240] John R. Ferraro, K. N., Chris W. Brown, *Introductory Raman Spectroscopy*, 2nd ed. California, USA: Academic Press, 2002.

[241] Stewart, S., D. A. Shea, C. P. Tarnowski*, et al.*, "Trends in early mineralization of murine calvarial osteoblastic cultures: a Raman microscopic study," *Journal of Raman Spectroscopy,* 33, 536-543, 2002.

[242] Querido, W., A. P. Campos, E. H. Martins Ferreira*, et al.*, "Erratum to: Strontium ranelate changes the composition and crystal structure of the biological bone-like apatite produced in osteoblast cell cultures," *Cell and Tissue Research,* 2014.

[243] Glimcher, M. J., "Recent studies of the mineral phase in bone and its possible linkage to the organic matrix by protein-bound phosphate bonds," *Philosophical Transaction of the Royal Society of London. Series B, Biological Sciences,* 304, 479-508, 1984.

[244] Termine, J. D., E. D. Eanes, D. J. Greenfield*, et al.*, "Hydrazine-deproteinated bone mineral. Physical and chemical properties," *Calcified Tissue Research,* 12, 73-90, 1973.

[245] Mahamid, J., L. Addadi, and S. Weiner, "Crystallization pathways in bone," *Cells, Tissues, Organs,* 194, 92-7, 2011.

[246] Malaval, L., F. Liu, P. Roche*, et al.*, "Kinetics of osteoprogenitor proliferation and osteoblast differentiation in vitro," *Journal of Cellular Biochemistry,* 74, 616-27, 1999.

[247] Garvie, L. A. J., "Can electron energy-loss spectroscopy (EELS) be used to quantify hydrogen in minerals from the O K edge?," *American Mineralogist,* 95, 92-97, 2010.

[248] Klosowski, M., "Electron microscopy characterisation of in vivo collagen and mineral ultrastructures, their development and pathologies," PhD Thesis, Materials, Imperial College London, London, 2014.

[249] Gibson, I. R. and W. Bonfield, "Novel synthesis and characterization of an AB-type carbonate-substituted hydroxyapatite," *Journal of Biomedical Materials Research,* 59, 697-708, 2002.

[250] Hyperspy: Hyperspectral data analysis toolbox. 2015

[251] Arenal, R., F. de la Peña, O. Stéphan*, et al.*, "Extending the analysis of EELS spectrum-imaging data, from elemental to bond mapping in complex nanostructures," *Ultramicroscopy,* 109, 32-38, 2008.

[252] Brandes, J. A., S. Wirick, and C. Jacobsen, "Carbon K-edge spectra of carbonate minerals," *Journal of Synchrotron Radiation,* 17, 676-82, 2010.

[253] Longo, P. (The use of MLLS fitting approach to resolve overlapping edges in the EELS spectrum at the atomic level.

[254] JC Elliott, R. W., SEP Dowker. (2002, 22 January 2016). Apatite Structures. *Advances in X-Ray Analysis 45*. Available: http://www.icdd.com/resources/axa/vol45/v45_28.pdf

[255] Kuhn, L. T., Y. T. Xu, C. Rey*, et al.*, "Structure, composition, and maturation of newly deposited calcium-phosphate crystals in chicken osteoblast cell cultures," *Journal of Bone and Mineral Research,* 15, 1301-1309, 2000.

[256] Porter, A. E., L. W. Hobbs, V. B. Rosen*, et al.*, "The ultrastructure of the plasma-sprayed hydroxyapatite-bone interface predisposing to bone bonding," *Biomaterials,* 23, 725-33, 2002.

[257] Aronova, M. A., A. A. Sousa, and R. D. Leapman, "EELS characterization of radiolytic products in frozen samples," *Micron,* 42, 252-256, 2011.

[258] Wang, C. G., J. W. Liao, B. D. Gou*, et al.*, "Crystallization at multiple sites inside particles of amorphous calcium phosphate," *Crystal Growth & Design,* 9, 2620-2626, 2009.

[259] Christoffersen, J., M. R. Christoffersen, W. Kibalczyc*, et al.*, "A contribution to the understanding of the formation of calcium phosphates," *Journal of Crystal Growth,* 94, 767-777, 1989.

[260] Koutsopoulos, S., "Synthesis and characterization of hydroxyapatite crystals: A review study on the analytical methods," *Journal of Biomedical Materials Research,* 62, 600-612, 2002.

[261] Rey, C., V. Renugopalakrishnan, B. Collins*, et al.*, "Fourier transform infrared spectroscopic study of the carbonate ions in bone mineral during aging," *Calcified Tissue International,* 49, 251-8, 1991.

[262] C. Rey, A. H., A. Tofighi, M.J. Glimcher, "Maturation of poorly crystalline apatites: Chemical and sturctural aspects in vivo and in vitro," *Cells and Materials,* 5, 345-356, 1995.

[263] Garvie, L. A. J., A. J. Craven, and R. Brydson, "Use of electron-energy-loss near-edge fine-structure in the study of minerals," *American Mineralogist,* 79, 411-425, 1994.

[264] Metzler, R. A., M. Abrecht, R. M. Olabisi*, et al.*, "Architecture of columnar nacre, and implications for its formation mechanism," *Physical Review Letters,* 98, 2007.

[265] Cazalbou, S., C. Combes, D. Eichert*, et al.*, "Poorly crystalline apatites: evolution and maturation in vitro and in vivo," *Journal of Bone and Mineral Metabolism,* 22, 310-317, 2004.

[266] Urquhart, S. G. and H. Ade, "Trends in the carbonyl core (C 1s, O 1s) -> pi*c=o transition in the near-edge X-ray absorption fine structure spectra of organic molecules," *Journal of Physical Chemistry B,* 106, 8531-8538, 2002.

[267] Neuman, W., M. Neuman, A. Diamond*, et al.*, "Blood: Bone disequilibrium. VI. Studies of the solubility characteristics of brushite: Apatite mixtures and their stabilization by noncollagenous proteins of bone," *Calcified Tissue International,* 34, 149-157, 1982.

[268] Hunter, G. K., P. V. Hauschka, A. R. Poole*, et al.*, "Nucleation and inhibition of hydroxyapatite formation by mineralized tissue proteins," *Biochemical Journal,* 317 (Pt 1), 59-64, 1996.

[269] Hu, J. T., P. D. Yang, and C. M. Lieber, "Nitrogen-driven sp(3) to sp(2) transformation in carbon nitride materials," *Physical Review B,* 57, R3185-R3188, 1998.

[270] Lehmann, J., Salomon, D., Brandes, J., Fleckenstein, H., Jacobsen, C., Theme, J., "Synchrotron-based near-edge X-ray spectroscopy of natural organic matter in soils and sediments," *Biophysico-Chemical Processes Involving Natural Nonliving Organic Matter in Environmental Systems,* 729-781, 2009.

[271] Vairavamurthy, A. and S. Wang, "Organic nitrogen in geomacromolecules: Insights on speciation and transformation with K-edge XANES spectroscopy," *Environmental Science & Technology,* 36, 3050-3056, 2002.

[272] Leinweber, P., J. Kruse, F. L. Walley*, et al.*, "Nitrogen K-edge XANES - An overview of reference compounds used to identify 'unknown' organic nitrogen in environmental samples," *Journal of Synchrotron Radiation,* 14, 500-511, 2007.

[273] Matsui, T., M. Yudasaka, R. Kikuchi*, et al.*, "2 kinds of nitrogen-atoms in nitrogen-substituted, highly crystalline graphite prepared by chemical-vapor-deposition," *Applied Physics Letters,* 65, 2145-2147, 1994.

[274] Bhattacharyya, S., M. Lubbe, P. R. Bressler*, et al.*, "Structure of nitrogenated amorphous carbon films from NEXAFS," *Diamond and Related Materials,* 11, 8-15, 2002.

[275] Gordon, M. L., G. Cooper, C. Morin*, et al.*, "Inner-shell excitation spectroscopy of the peptide bond: Comparison of the C 1s, N 1s, and O 1s spectra of glycine, glycyl-glycine, and glycyl-glycyl-glycine," *Journal of Physical Chemistry A,* 107, 6144-6159, 2003.

[276] Boskey, A. L., M. Maresca, W. Ullrich*, et al.*, "Osteopontin-hydroxyapatite interactions in-vitro - inhibition of hydroxyapatite formation and growth in a gelatin-gel," *Bone Miner,* 22, 147-159, 1993.

[277] Binderman, I., D. Duksin, A. Harell*, et al.*, "Formation of bone tissue in culture from isolated bone cells," *Journal of Cell Biology,* 61, 427-39, 1974.

[278] Bachra, B. N., "Precipitation of calcium carbonates and phosphates from metastable solutions," *Annals of the New York Academy of Sciences,* 109, 251-5, 1963.

[279] Bachra, B. N., O. R. Trautz, and S. L. Simon, "Precipitation of calcium carbonates and phosphates. I. Spontaneous precipitation of calcium carbonates and phosphates under physiological conditions," *Archives of Biochemistry and Biophysics,* 103, 124-38, 1963.

[280] Eanes, E. D., I. H. Gillessen, and A. S. Posner, "Intermediate states in the precipitation of hydroxyapatite," *Nature,* 208, 365-7, 1965.

[281] Beniash, E., R. A. Metzler, R. S. Lam*, et al.*, "Transient amorphous calcium phosphate in forming enamel," *Journal of Structural Biology,* 166, 133-43, 2009.

[282] Lowenstam, H. A. and S. Weiner, "Transformation of amorphous calcium-phosphate to crystalline dahllite in the radular teeth of chitons," *Science,* 227, 51-53, 1985.

[283] Stricker, S. A. and S. Weiner, "Amorphous calcium-phosphate in the stylets Produced by a marine worm (Nemertea)," *Experientia,* 41, 1557-1559, 1985.

[284] McCaslin FEJ, J. J., "The effect of strontium lactate in the treatment of osteoporosis," *Proceedings of Staff Meetings of the Mayo Clinic,* 34, 329-334, 1959.

[285] Skoryna, S. C., "Effects of oral supplementation with stable strontium," *Canadian Medical Association Journal,* 125, 703-12, 1981.

[286] Li, X., C. P. Xu, Y. L. Hou*, et al.*, "A novel resorbable strontium-containing alpha-calcium sulfate hemihydrate bone substitute: a preparation and preliminary study," *Biomedical Material,* 9, 045010, 2014.

[287] Zhao, Y., D. Guo, S. Hou*, et al.*, "Porous allograft bone scaffolds: doping with strontium," *Plos One,* 8, e69339, 2013.

[288] Baier, M., P. Staudt, R. Klein*, et al.*, "Strontium enhances osseointegration of calcium phosphate cement: a histomorphometric pilot study in ovariectomized rats," *Journal of Orthopaedic Surgery and Research,* 8, 16, 2013.

[289] Ni, G. X., W. W. Lu, B. Xu*, et al.*, "Interfacial behaviour of strontium-containing hydroxyapatite cement with cancellous and cortical bone," *Biomaterials,* 27, 5127-33, 2006.

[290] Querido, W., A. P. C. Campos, E. H. M. Ferreira*, et al.*, "Strontium ranelate changes the composition and crystal structure of the biological bone-like apatite produced in osteoblast cell cultures," *Cell and Tissue Research,* 357, 793-801, 2014.

[291] Yamaguchi, M. and M. N. Weitzmann, "The intact strontium ranelate complex stimulates osteoblastogenesis and suppresses osteoclastogenesis by antagonizing NF-kappa B activation," *Molecular and Cellular Biochemistry,* 359, 399-407, 2012.

[292] Sudo, H., H. A. Kodama, Y. Amagai*, et al.*, "In vitro differentiation and calcification in a new clonal osteogenic cell-line derived from newborn mouse calvaria," *Journal of Cell Biology,* 96, 191-198, 1983.

[293] Puchtler, H., S. N. Meloan, and M. S. Terry, "On the history and mechanism of alizarin and alizarin red S stains for calcium," *Journal of Histochemistry & Cytochemistry,* 17, 110-24, 1969.

[294] Meloan, S. N. P., Holde, "Chemical mechanisms of staining methods: Von Kossa's technique: What Von Kossa really wrote and a modified reaction for selective demonstration of inorganic phosphates," *Journal of Histotechnology,* 11-13, 1985.

[295] St-Pierre, J. P., L. Gan, J. Wang*, et al.*, "The incorporation of a zone of calcified cartilage improves the interfacial shear strength between in vitro-formed cartilage and the underlying substrate," *Acta Biomaterialia,* 8, 1603-1615, 2012.

[296] Reddy, G. K. and C. S. Enwemeka, "A simplified method for the analysis of hydroxyproline in biological tissues," *Clinical Biochemistry,* 29, 225-229, 1996.

[297] Pablo Mobili, A. L., Graciela De Antoni, andrea Gomez-Zavaglia, Cuauhtemoc Araujo-Andrade, H. Avila-Donoso, "Multivariate analysis of Raman spectra

applied to microbiology: Discrimination of microorganisms at the species level," *Revista Mexicana de Fisica,* 56, 378-385, 2010.

[298] Bonnier, F. and H. J. Byrne, "Understanding the molecular information contained in principal component analysis of vibrational spectra of biological systems," *Analyst,* 137, 322-32, 2012.

[299] Ian R. Lewis, H. E., *Handbook of Raman Spectroscopy: From the Research Laboratory to the Process Line*. New York, USA: Marcel Dekker, Inc., 2001.

[300] Chung, C. H., E. E. Golub, E. Forbes*, et al.*, "Mechanism of action of beta-glycerophsphate on bone cell mineralization," *Calcified Tissue International,* 51, 305-311, 1992.

[301] Bellows, C. G., J. N. Heersche, and J. E. Aubin, "Inorganic phosphate added exogenously or released from beta-glycerophosphate initiates mineralization of osteoid nodules in vitro," *Bone and Mineral,* 17, 15-29, 1992.

[302] Boskey, A. L., P. Guidon, S. B. Doty*, et al.*, "The mechanism of beta-glycerophosphate action in mineralizing chick limb-bud mesenchymal cell cultures," *Journal of Bone Mineral Research,* 11, 1694-702, 1996.

[303] Khouja, H. I., A. Bevington, G. J. Kemp*, et al.*, "Calcium and orthophosphate deposits in-vitro do not imply osteoblast-mediated mineralization - mineralization by beta-glycerophosphate in the absence of osteoblasts," *Bone,* 11, 385-391, 1990.

[304] Dean, D. D., Z. Schwartz, L. Bonewald*, et al.*, "Matrix vesicles produced by osteoblast-like cells in culture become significantly enriched in proteoglycan-degrading metalloproteinases after addition of beta-glycerophosphate and ascorbic-acid," *Calcified Tissue International,* 54, 399-408, 1994.

[305] Fratzl-Zelman, N., P. Fratzl, H. Horandner*, et al.*, "Matrix mineralization in MC3T3-E1 cell cultures initiated by beta-glycerophosphate pulse," *Bone,* 23, 511-20, 1998.

[306] Chang, Y. L., C. M. Stanford, and J. C. Keller, "Calcium and phosphate supplementation promotes bone cell mineralization: Implications for hydroxyapatite (HA)-enhanced bone formation," *Journal of Biomedical Materials Research,* 52, 270-278, 2000.

[307] Fujino, O., "The coprecipitation of strontium with hydroxyapatite," *Bulletin of the Chemical Society of Japan,* 48, 1455-1458, 1975.

[308] Guilbert, M., G. Said, T. Happillon*, et al.*, "Probing non-enzymatic glycation of type I collagen: a novel approach using Raman and infrared biophotonic methods," *Biochimica Et Biophysica Acta,* 1830, 3525-31, 2013.

[309] Dehring, K. A., A. R. Smukler, B. J. Roessler*, et al.*, "Correlating changes in collagen secondary structure with aging and defective type II collagen by Raman spectroscopy," *Applied Spectroscopy,* 60, 366-72, 2006.

[310] Juillard, A., G. Falgayrac, B. Cortet*, et al.*, "Molecular interactions between zoledronic acid and bone: An in vitro Raman microspectroscopic study," *Bone,* 47, 895-904, 2010.

[311] Bergholt, M. S., W. Zheng, and Z. W. Huang, "Characterizing variability in in vivo Raman spectroscopic properties of different anatomical sites of normal tissue in the oral cavity," *Journal of Raman Spectroscopy,* 43, 255-262, 2012.

[312] Stephen P. Morgan, F. R. R., Stephen J. Matcher, *Optical Techniques in Regenerative Medicine*, Illustrated ed. Florida, USA: CRC Press, 2013.

[313] Garreau, S., G. Louarn, J. P. Buisson*, et al.*, "In situ spectroelectrochemical Raman studies of poly(3,4-ethylenedioxythiophene) (PEDT)," *Macromolecules,* 32, 6807-6812, 1999.

[314] Withnall, R., B. Z. Chowdhry, J. Silver*, et al.*, "Raman spectra of carotenoids in natural products," *Spectrochimica Acta Part a-Molecular and Biomolecular Spectroscopy,* 59, 2207-2212, 2003.

[315] Qin, J. W., K. L. Chao, and M. S. Kim, "Nondestructive evaluation of internal maturity of tomatoes using spatially offset Raman spectroscopy," *Postharvest Biology and Technology,* 71, 21-31, 2012.

[316] Swain, R. J., G. Jell, and M. M. Stevens, "Non-invasive analysis of cell cycle dynamics in single living cells with Raman micro-spectroscopy," *Journal of Cellular Biochemistry,* 104, 1427-38, 2008.

[317] Mandair, G. S. and M. D. Morris, "Contributions of Raman spectroscopy to the understanding of bone strength," *Bonekey Reports,* 4, 620, 2015.

[318] St-Pierre, J.-P., "The Role of Inorganic Polyphosphates in the Formation of Bioengineered Cartilage Incorporating a Zone of Calcified Cartilage In Vitro," PhD Thesis, Materials Science and Engineering, University of Toronto, Toronto, Canada, 2011.

[319] Delannoy, P., D. Bazot, B. Robin*, et al.*, "Long-term treatment with strontium ranelate (S12911) increases vertebral bone mass without deleterious effect in mice.," *Journal of Bone and Mineral Research,* 16, S294-S294, 2001.

[320] Roux, C., J. Y. Reginster, J. Fechtenbaum*, et al.*, "Vertebral fracture risk reduction with strontium ranelate in women with postmenopausal osteoporosis is independent of baseline risk factors," *Journal of Bone Minerals Research,* 21, 536-42, 2006.

[321] Verberckmoes, S. C., M. E. De Broe, and P. C. D'Haese, "Dose-dependent effects of strontium on osteoblast function and mineralization," *Kidney International,* 64, 534-43, 2003.

[322] Reinholt, F. P., A. Hjerpe, K. Jansson*, et al.*, "Stereological studies on the epiphyseal growth plate in strontium-Induced rickets - with special reference to the distribution of matrix vesicles," *Journal of Bone and Joint Surgery-American Volume,* 66A, 1274-1280, 1984.

[323] Shibata, S. and Y. Yamashita, "An ultrastructural study of osteoclasts and chondroclasts in poorly calcified mandible induced by high doses of strontium diet to fetal mice," *Annals of Anatomy,* 183, 357-61, 2001.

[324] Jablonski, M. B., E. A. Stefaniak, L. Darchuk*, et al.*, "Microchemical investigation of bone derived from mice treated with strontium in different chemical forms using scanning electron microscopy and micro-Raman spectroscopy," *Microchemical Journal,* 108, 168-173, 2013.

[325] Turzanska, K., M. Jablonski, A. Posturzynska*, et al.*, "Bioavailability of strontium administered orally to growing mice as ranelate versus chloride. A pilot study," *Bone,* 44, S433-S434, 2009.

[326] Neufeld, E. B. and A. L. Boskey, "Strontium Alters the Complexed Acidic Phospholipid Content of Mineralizing Tissues," *Bone,* 15, 425-430, 1994.

[327] Cox, T. R. and J. T. Erler, "Remodeling and homeostasis of the extracellular matrix: implications for fibrotic diseases and cancer," *Disease Models & Mechanisms,* 4, 165-178, 2011.

[328] Chiquet, M., L. Gelman, R. Lutz*, et al.*, "From mechanotransduction to extracellular matrix gene expression in fibroblasts," *Biochimica Et Biophysica Acta-Molecular Cell Research,* 1793, 911-920, 2009.

[329] Huang, Z., F. Z. Cui, Q. L. Feng*, et al.*, "Incorporation of strontium into hydroxyapatite via biomineralization of collagen fibrils," *Ceramics International,* 41, 8773-8778, 2015.

[330] Elaine DiMasi, L. B. G., *Biomineralization Sourcebook: Characterization of Biominerals and Biomimetic Minerals*: CRC Press, 2014.

8. Appendices

Table A 1 Summary of studies showing desirable effect of strontium supplementation

Year & Ref	**System & Length of Study**	**Strontium Type and Dose**	**Control**	**Assays**	**Results**
1983 [197]	*in vivo* – rats 6 weeks Normal calcium diet	$SrCl_2$ 0.5mL of 1N	$CaCl_2$ -treated rats	Width of bone formation by microscopy	Ca and Sr stimulate bone formation; Sr group has faster bone growth, but shorter in duration
1985 [186]	*in vivo* – rats 9 weeks Normal calcium and vitamin D diet	$SrCl_2$ 1.9, 2.7, 3.4, 4.0g/L	Strontium-free control	Biochemical (serum, urine, bone ash) and bone histology	Sr supplement did not produce deleterious effects on body growth; Slight transitory decrease in serum calcium was observed; 0.40% supplement reduce mineralisation due to excessive osteoid thickness associated to decreased calcification rate and prolonged mineralisation lag time; At lower Sr supplement (0.27%), Sr stimulated bone formation (increased amount of osteoid; 10% increase in trabecular calcified bone mass); Number of osteoclasts unchanged after treatment
1986 [145]	*in vivo* – mice 4 weeks A follow up paper from 1985; Normal calcium and vitamin D diet;	$SrCl_2$ 2.7g/L Detected Sr in serum: 0.085 ± 0.010 mM	Strontium-free control; NaF (4mg/L); Combination of 4mg/L NaF and 2.7g/L $SrCl_2$	Serum analysis, bone histomorphometry	Bone formation and bone density is not observed to be significant at this time point; Bone resorbing cells are transiently reduced with Sr treatment
1988 [188]	*in vitro* – bone culture 10 days Normal calcium cell medium	$SrCl_2$ 0.1, 1, 5mM	Strontium-free control	Calcium content, bone resorbing activity assay	$SrCl_2$ has an inhibitory effect on bone resorption

1990 [189]	*in vivo* – rats 4 and 8 weeks Normal calcium and vitamin D diet	$SrCl_2$ 1.9 and 4.0g/L	Strontium-free control	Bone mineral X-ray diffraction, bone histomorphometry, bone resorption, carbonate analysis, bone elemental analysis	4.0g/L decrease mineralisation by increased amount of osteoid; Mineral crystal is less crystaline in the higher Sr-supplementation; Decrease in carbonate content as Sr-supplement increases; Sr seems to be replacing Ca in the bone mineral
1993 [187]	*in vivo* - rats (some ovaruectimised) 60 days Normal calcium diet	S12911 (Sr-ranelate) 77, 154, and 308 mg/kg/day	Sham mice, and strontium-free control	Alkaline phosphatase levels, bone mineral content, bone histomorphometry	Sr-Ranelate treatment increases plasma alkaline phosphatase and osteocalcin by 14-32% and 43-71%, respectively; Increasing Sr-ranelate supplement increases calcium detection in urine.
1996 [144]	*in vivo* – rats 8 weeks Normal calcium diet	$SrCl_2$ 2.0g/L Detected Sr in serum: 0.13±0.01 mM	Strontium-free control	Serum analysis, bone histomorphometry, bone density fractionation	Sr supplementation significantly increased the osteoid surface, osteoblast surface, and bone forming surfaces; Sr supplementation did not increase appositional rate, suggesting that the bone matrix synthesis rate did not increase; Sr and Ca administration must be given separately to optimise Sr uptake and bone formation
1996 [155]	*in vitro* - mouse calvaria culture and calvarial cell culture 3 days Normal calcium media	S12911 (Sr-ranelate) in the order of 1mM, 0.1mM, 0,01mM	Strontium-free control; calcium and sodium control	Histomorphometric observation, collagen production	The positive effect of the Sr treatment is specific to Sr, since the Ca and Na treatments did not produce the effects; Treatment on organ culture: Sr supplementation in the order of 1mM stimulates replication of calvarial preosteoblasts (the other concentrations did not) up 24 and 48 hours (but not in 72 hours; i.e. transient effect); Treatment on cell culture: increased in fibroblasts, pre-osteoblasts, and osteoblasts, as well as increased collagen and non-collagen protein synthesis number at 24 hours

2001 [190]	*in vivo* – monkey 26 weeks Normal calcium diet	S12911 (Sr-ranelate) 100, 275, or 750 mg/kg Detected Sr in serum of the highest Sr-treatment: 0.220 ± 0.032 mM	Strontium-free control	Blood plasma biochemistry, bone histomorphometry; males and females comparison	Sr treatment decrease bone resorption indices (at the medium and highest concentrations); Sr treatment did not alter bone formation indices
2002 [191]	*in vivo* – mice 104 weeks Normal calcium diet	S12911 (Sr-ranelate) 0.78, 2.34 or 7.01 mmol Sr /kg/d Sr serum level increased from 0.015 to 0.181 mM (males) and 0.023 to 0.266 mM (females) at the highest Sr-treatment	Strontium-free control	Blood plasma biochemistry, bone histomorphometry; males and females comparison	The concentrations tested did not affect bone mineralisation deleteriously; Sr treatment increased bone formation in both genders; Sr decreased bone resorption indices significantly in females (not in males)
2002 [192]	*in vivo* – osteoporotic postmenopausal women with at least one spinal fracture 24 months Calcium and vitamin D supplements were given	Sr-Ranelate 0.125, 0.5, or 1g/d	Strontium-free control (placebo)	Blood plasma biochemistry, bone mineral density	Sr treatment did not result in negative impact on bone mineralisation; Sr treatment resulted in a dose-dependent increase in lumbar bone mass density; Reduction in fracture incidence for Sr treated groups; Highest Sr dose resulted in increased serum bone alkaline phosphatase and osteocalcin;
2002 [193]	*in vivo* – osteoporotic postmenopausal women with at least one spinal fracture 24 months Calcium and vitamin D supplements were given	Sr-Ranelate 0.5, 1, or 2g/d	Strontium-free control (placebo)	Blood plasma biochemistry, bone mineral density	Sr treatment did not result in negative impact on bone mineralisation; Sr treatment resulted in a dose-dependent increase in lumbar bone mass density of about 3%/year; Reduction in fracture incidence for Sr treated groups; Highest Sr dose resulted in increased serum bone alkaline phosphatase;

2003 [195]	*in vivo* – rats 2 weeks Normal calcium and vitamin D diet	S12911 - 2 (Sr-ranelate) 0.1, 0.4, and 1.6 mmol/kg/day Detected Sr in serum: 0.014, 0.066, 0.216 mM at the doses of 0.1, 0.4, 1.6 mmol/kg/day, respectively	Strontium-free control; non-immobilise control	Blood plasma biochemistry, bone histomorphometry; comparing immobilised and non-immobilised bones	Bone mass was improved by Sr treatment after immobilisation, but osteopenia was not fully corrected;
2004 [146]	*in vivo* – osteoporotic postmenopausal women with at least one spinal fracture 3 years Calcium and vitamin D supplements were given	Sr-Ranelate 2g/day Detected Sr in serum: 0.118mM	Strontium-free control (placebo)	Blood plasma biochemistry, bone histomorphometry	Sr treatment reduced the risk of multiple vertebral fractures and the risk of symptomatic fractures; Sr treatment increased serum concentration of bone-specific alkaline phosphatase and bone mineral density; Sr treatment decreased bone resorption
2004 [196]	*in vivo*- intact rats 2 years Calcium-containing diet	Sr-Ranelate 0, 225, 450, 900 mg/kg/day Detected Sr in Serum: 0.32mM at the highest concentration	Strontium-free control	Bone mineral mass, mechanical properties, bone histomorphometry, ALP activity	Sr treatment increase bone strength and bone mass (due to increased bone volume and trabecular number and thickness) of vertebral bone in a dose-dependent manner in both male and female rats; Sr treatment increased ALP activity
2004 [154]	*in vitro* - MC3T3-E1 4, 10, 14 days Ascorbic acid supplementation = 25µg/mL; phosphate supplement: 3 mM	S12911 - 2 (Sr-ranelate) 0.1, 0.5, 1mM	Strontium-free control with or without 1,25(OH)2D vitamin D (inhibit collagenous synthesis by a transcriptional mechanism in mouse osteoblastic cells)	ALP activity, collagen quantification, ion measurements, quantification on mineralisation	1mM Sr treatment increased ALP activity and collagen synthesis compared with controls; No significant difference between Sr treatment and control in terms of the mineralised nodule surface

2008 [148]	*in vivo* – osteoporotic postmenopausal women 5 years	Sr-Ranelate 2g/d	Strontium-free control	New fracture incidence, new vertebral fracture, bone mineral density (X-ray absorphometry)	Sr treatment reduce fracture risk
2009 [194]	*in vivo* – osteoporotic postmenopausal women 8 years	Sr-Ranelate 2g/d	Strontium-free control (placebo)	Fracture risk, bone mineral density	No statistical difference was seen in the occurrence of osteoporotic fracture in the last 3 years; Continual increase of bone mineral density was seen throughout the years
2009 [147]	*in vivo* – osteoporotic postmenopausal women 5 years	Sr-Ranelate 2g/d	Strontium-free control (placebo)	Fracture risk, bone mineral density, quality of life	Sr treatment resulted in reduction in the risk of vertebral fractures; Bone mineral density shown to be increased due to the presence of Sr treatment; Sr treatment produced a significant improvement to quality of life

Table A 2 Description of various peaks at the phosphorus $L_{2,3}$-edge, calcium $L_{2,3}$-edge, nitrogen K-edge, and oxygen K-edge as seen in Figure 4.10. The description is as found in [248].

	Approximate Energy Loss (eV)	Description
Phosphorus		
A	138	Transitions to p-like states
B	141	Transitions from 2p state to new state created from due to interactions with calcium 3d orbital function (Characteristic for calcium-containing minerals)
C	146	Transitions to d-like states
D	160	Multiple scattering and the maximum 2p state cross section
Calcium		
E	348	Transitions from spin-orbital split 2p states ($2p_{1/2}$, $2p_{3/2}$) to d-like states
F	351	Transitions from spin-orbital split 2p states ($2p_{1/2}$, $2p_{3/2}$) to d-like states
Nitrogen		
G	400-401	1s-π* transitions; nitrogen in an aromatic ring, especially pyridine that is essential part of collagen crosslinking
H	408	broad peak C is attributed more generally to 1s-σ* transitions in amino compounds
Oxygen		
I	537	Transitions to the vacant π* states of the Ca-O bonding environment
J	539	Transitions to the vacant σ* states of the Ca-O bonding environment
K	545	Transitions to 4s- and 4p-like states in calcium-oxygen bonds

Table A 3 Description of various peaks at the carbon K-edge as seen in Figure 4.11. The description is as found in [248].

	Approximate Energy Loss (eV)	**Description**
Carbon		
A	285	Transitions to vacant π*states in in the carbon-carbon bonding environment (Amorphous Carbon)
Red line	287	Transitions to the vacant π*state of carbonyl groups
Blue line	290.2	Transitions to the vacant π*-A states of CO_3 groups
B	297	Transitions to vacant σ* states in the carbon-carbon bonding environment

Table A 4 EDX values of the different mineral morphologies

Dense Granules	**Needle-Like Globules**	**Mature**
1.151754	1.759849	1.779984
1.036207	1.698514	1.660007
0.953858	1.503456	1.650031
1.301407	1.564648	1.761647
1.574682	1.407235	1.715262
0.917504	1.196343	1.73558
1.584252	1.557095	1.391851
1.073759	1.894579	1.412498
	1.604841	1.403309
	1.644475	1.39772
		1.432977
		1.361353
		1.349498
		1.348699
		1.33685
		1.346227

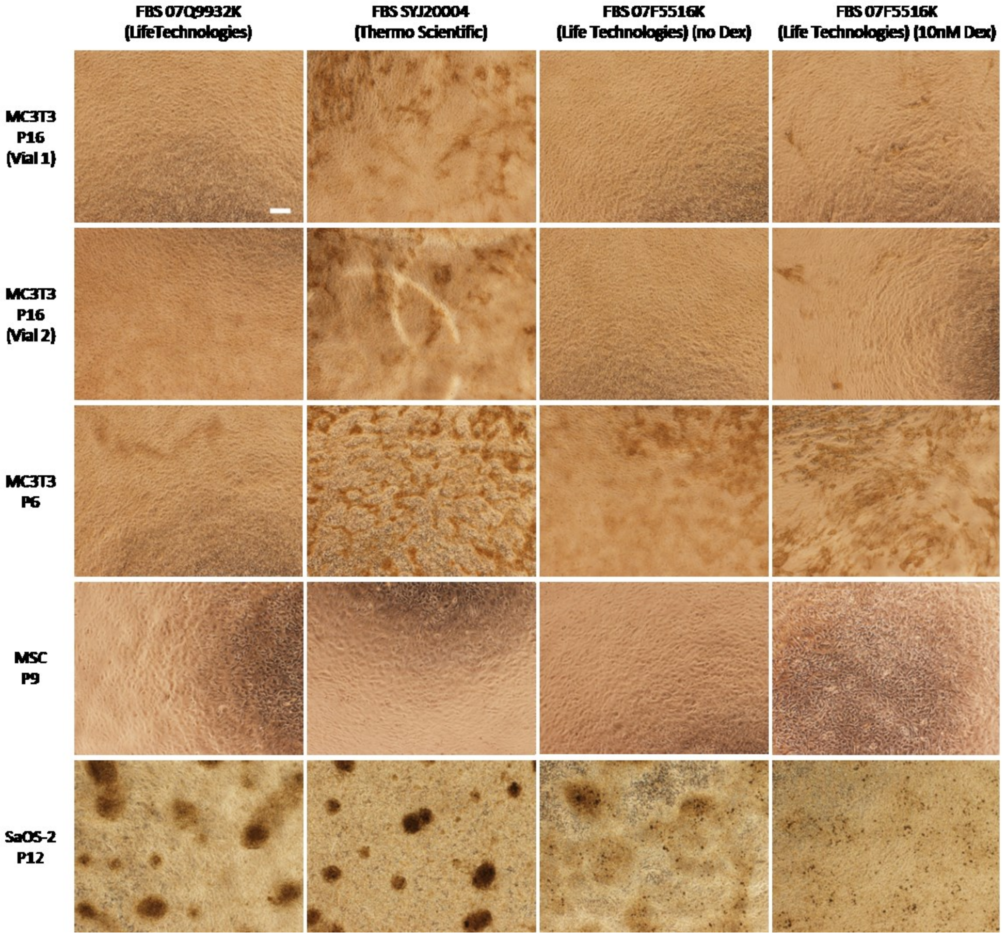

Figure A.1 Bright field light microscopy images showing various mineralising cells at various passage numbers (denoted by P#) at day 14, cultured in ascorbic-acid-free αMEM supplemented with 50 mg/mL ascorbic acid, 2 mM ß-glycerophosphate, and 10% (v/v) FBS from various sources and batches. The effect of dexamethasone (Dex; a form of steroid) was also tested. All cultures started with the same number of cells, in 24-well plates, and were cultured at the same time with the same amount of media. Scale bar denotes 200 µm.